AUG 3 1999

RECEIVED
AUG 11 1999
OSTI

DESIGN, MANUFACTURE AND TESTING OF A

Bend-Twist D-spar

Cheng-Huat Ong & Stephen W. Tsai
Department of Aeronautics & Astronautics
Stanford University
Stanford CA 94305-4035

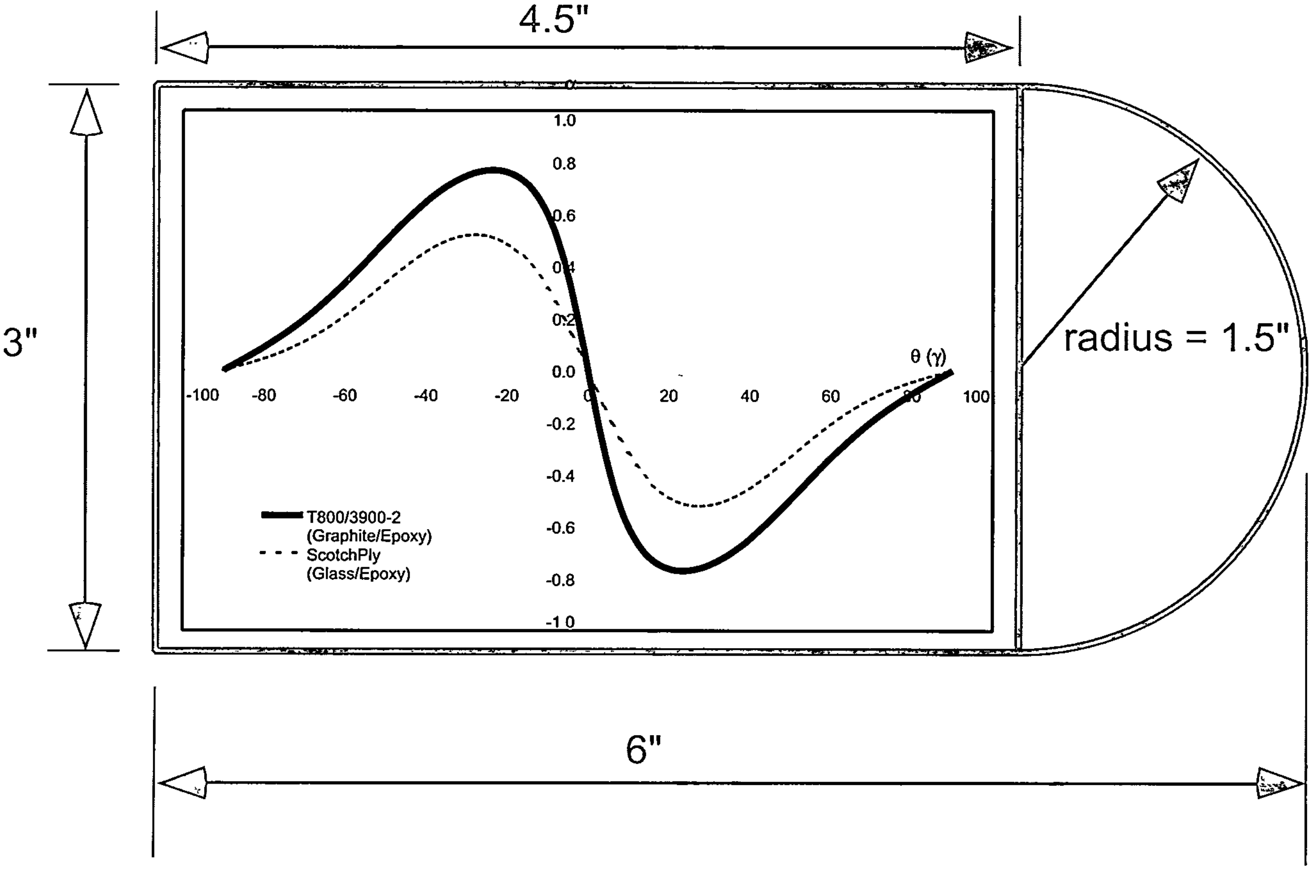

SAND99-1324
Unlimited Release
Printed June 1999

Prepared by
Sandia National Laboratories
Albuquerque, New Mexico 87185 and Livermore, California 94550

Sandia is a multiprogram laboratory operated by Sandia Corporation,
a Lockheed Martin Company, for the United States Department of Energy
under contract DE-AC04-94AL85000.

Approved for public release; further dissemination unlimited.

Sandia
National
Laboratories

Issued by Sandia National Laboratories, operated for the United States Department of Energy by Sandia Corporation.

Printed in the United States of America. This report has been reproduced directly from the best available copy.

Available to DOE and DOE contractors from
Office of Scientific and Technical Information
P.O. Box 62
Oak Ridge, TN 37831

Prices available from (703) 605-6000
Web site: http://www.ntis.gov/ordering.htm

Available to the public from
National Technical Information Service
U.S. Department of Commerce
5285 Port Royal Rd
Springfield, VA 22161

NTIS price codes
Printed copy: A03
Microfiche copy: A01

SAND 99-1324
Unlimited Distribution
Printed June 1999

Design, Manufacture and Testing of A Bend-Twist D-spar

Cheng-Huat Ong & Stephen W. Tsai
Department of Aeronautics & Astronautics
Stanford University
Stanford CA 94305-4035

Sandia Contract: BB-6066

Abstract

Studies have indicated that an adaptive wind turbine blade design can significantly enhance the performance of the wind turbine blade on energy capture and load mitigation. In order to realize the potential benefits of aeroelastic tailoring, a bend-twist D-spar, which is the backbone of a blade, was designed and fabricated to achieve the objectives of having maximum bend-twist coupling and fulfilling desirable structural properties (EI & GJ). Two bend-twist D-spars, a hybrid of glass and carbon fibers and an all-carbon D-spar, were fabricated using a bladder process. One of the D-spars, the hybrid D-spar, was subjected to a cantilever static test and modal testing.

Various parameters such as materials, laminate schedule, thickness and internal rib were examined in designing a bend-twist D-spar. The fabrication tooling, the lay-up process and the joint design for two symmetric clamshells are described in this report. Finally, comparisons between the experimental test results and numerical results are presented. The comparisons indicate that the numerical analysis (static and modal analysis) agrees well with test results.

Acknowledgements

This project was supported by Sandia National Laboratories under Contract No. BB-6066. The Technical Monitor is Dr. Paul S. Veers. The authors would like to thank Dr. D. W. Lobitz and Dr. P. S. Veers for their participation in many beneficial discussions. The authors would like to thank Dr. Thomas G. Carne and his staff, from Sandia National Laboratories, for sharing his experience on modal testing and test data. The authors would also like to thank the staffs and researchers from Materials Research Laboratories/ Industrial Technology Research Institute (Taiwan) for their support and assistance in the fabrication and static testing of D-spars. The authors would like to thank Ms. Julie Wang for her contribution and effort on D-spar fabrication and testing.

Contents

Chapter 1

Introduction

Researchers are exploring the potential benefits of the anisotropic characteristics of composite materials. A composite design that exhibits various degrees of anisotropy has tremendous advantages not seen in an orthotropic composite structure. The benefits are seen either in fixed wing, helicopter blade or wind turbine blade design.

One of the applications of aeroelastic tailoring is the use of a bend-twist coupled composite wing to prevent divergence of the forward swept wing.[1] Weisshaar[1] also highlighted other potential benefits for a fixed wing design, such as load relief, vibration control and increase of lift coefficients, resulting from the application of bend-twist coupling.

Smith & Chopra[2] proposed that composite designs exhibiting various couplings appear to have great potential for use in helicopter blades and tilt-rotor blades to reduce vibration, enhance aeroelastic stability, and improve aerodynamic efficiency. They formulated an analytical model for composite box-beam in the shape of a rectangle or square for rotor blade application. Their model can predict the behavior of a composite box-beam that exhibits bend-twist or extension-twist coupling. Their analytical predictions agree generally well with the results of the finite element model (FEM) and the experimental model.[3] The highlight of their findings is that torsion-related out-of-plane warping can substantially influence torsion and coupled torsion deformations in a symmetric lay-up box-beam.

The application of elastic (or aeroelastic) tailoring can also be found in wind turbine applications. Karaolis[4, 5] demonstrates the concept of anisotropy lay-ups in blade skin to achieve different types of twist coupling for wind turbine applications. Kooijman[6] investigated the optimum bend-twist flexibility distribution of a rotor blade to improve rotor blade design. Lobitz and Veers[7] studied generic coupling effects on the annual energy production of a stall-regulated wind turbine. They concluded that, with a small twist, a stall-controlled, fixed-pitch system could be operated with a larger rotor to achieve net energy enhancements.

Our interests here are related to the physical application of elastic tailoring of composite materials to enhance load mitigation as studied by Lobitz and Laino[8]. Although there are potential benefits to elastic tailoring, there are key issues that need to be resolved before the actual realization of a bend-twist coupled wind turbine blade. Two of the key issues are dynamic stability and the ability to manufacture a bend-twist couple blade. Lobitz and Veers[9] address two of the most common stability constraints, namely, flutter and divergence. A coupling coefficient, α, is used to facilitate the generic examination of the flutter and divergence boundary of a combined experiment blade (CEB). The study indicates that the flutter and divergence airspeeds are a function of the strength of the coupling; the strength of the coupling increases as the magnitude of the coupling coefficient, α, increases.

Mathematically, the range of α is between -1 and 1 as indicated by Lobitz and Veers.[9] The implicit question that needs to be addressed is the feasible range of α if composite materials are used. In the present study, an airfoil-type structure, a D-spar, is used as a test case to establish the achievable α range and the critical key parameters that exhibit a higher degree of coupling. The D-spars were designed to meet specific dimensions, desirable structural properties, and the maximum bend-induced twist per unit pound. The ability to manufacture bend-twist coupled D-spars is also demonstrated. Finally, one of the D-spars was subjected to a cantilever static test and the test results are compared to numerical results.

Chapter 2

3D-Beam Software Modifications & Verification

The 3D-Beam[10] program is for analyzing composite beam and frame structures with arbitrary cross-sections by the finite element method. The backbone of this program is a spreadsheet based software, Microsoft Excel. Therefore, the 3D-Beam is usable on any personal computer that runs the spreadsheet program.

This program is further modified to include the following features:

a. Option for "Plane Stress" input,

b. Option for "Thin Wall" input, and

c. Torsion-related Out-of-Plane warping for closed cell.

A series of cantilevered static tests (bending and torsion) has been conducted to verify the 3D-Beam predictions. The types of beams tested consisted of aluminum boxes, orthotropic and anisotropic sandwich beams, and composite box beams.

2.1 3D-Beam Modifications

2.1.1 Option for "Plane Stress" input

One of the basic assumptions used in the formulation of 3D-Beam equations is that the transverse strain (e_2, see Figure 2.1 for the notation) is zero. This is a natural consequence of the one-dimensional nature of beam theory itself. Smith & Chopra[2] stressed that when the walls of the box-beam are made of laminated composite material plies, transverse in-plane normal stress and strain can be quite important. They further examined three different methods for accounting for skin in-plane elastic behavior. The three methods are

- Method 1

Based only on an initial kinematics assumption about the deformations of the beam leads to,

$$e_2 = 0$$

- Method 2

In this method, the following assumption is made;

$$\sigma_2 = 0$$

e_2 is then calculated from the constitutive relation by substitution.

- Method 3

In this method, the conditions on the in-plane stresses and strains are imposed so that there are no in-plane forces and moments. Smith & Chopra[2] prefer to use this method in their beam formulation.

The 3D-Beam program has been modified to let a user have a choice for either Method 1 or 2. We define Method 1 as Plane Strain and Method 2 as Plane Stress. Our preference is Method 2, because our experimental results indicated that e_2 is not equal to zero and has the same order of magnitude as e_1.

2.1.2 Option for "Thin Wall" input

The 3D-Beam software was originally formulated on the assumption that the shear stress through the skin thickness is not negligible. This assumption is applicable if the skin of a beam is thick. In the modification, we create an input option for a user to choose either a "Thick Wall" or "Thin Wall" formulation.

In the "Thin Wall" formulation, the approach is similar to that given in *Section 14.99, ANSYS Theory Reference*. In that section, it is suggested that to avoid shear locking, a flush factor be used to reduce the magnitude of transverse out-of-plane shear modulus. This flush factor depends on the element area in the 1-2 plane and average total thickness. Our approach is to divide the ply out-of-plane shear modulus by a large factor if "Thin Wall" is selected.

2.1.3 Torsion-related Out-of-Plane Warping for a Closed Cell

To include the effect of torsion-related out-of-plane warping, a warping function, λ ($=\beta * x_1 * x_2$), is used. The axial displacement (x_1 direction) due to warping is,

$$U_1 = \lambda * \frac{\partial \phi_1}{\partial x_1}, \tag{2.1}$$

where ϕ_1 is the twist angle in the x_1 direction. This term is then added to the corresponding displacement kinematic equation.

2.2 3D-Beam Verification

A series of cantilevered static tests on various types of beams were conducted to verify the prediction of 3D-Beam software before and after the modifications. The experimental set up is described in Ong.[11] The beams tested included both the isotropic and composite beams.

2.2.1 Aluminum Box Beam

The external dimensions of the aluminum box beam are 3/4" (width), 3/4" (depth) and 32" (long). The skin thickness is 1/16". The aluminum box beam was subjected to both bending and torsion tests. The normalized test and numerical results are shown in Figure 2.2 and 2.3. Before the modifications, the predicted results underestimated the experimental values. The modifications based on Plane Stress assumption improve the prediction. It should be noted that the effect of torsion-related out-of-plane warping is not seen in Figure 2.3 as there is no warping for a square aluminum box with constant skin thickness.

2.2.2 Composite Box Beam

The external dimensions of the composite box beam are 3" (width), 1" (depth) and 29" (length). The lay-up of the composite skin is $[\pm 20^\circ_3]_T$. The ply material of the laminate skin is LTM-45, and the properties of the ply are given in Table 2.1.

The composite box beam was subjected to both the bending and torsion tests. The measured parameters were the vertical deflection, the twisting angle and strains at two longitudinal locations (x=10" and 15" from the built-in end).

Comparisons between the experimental results and numerical results for the bending test are shown in Figures 2.4 - 2.6. The 3D-Beam's prediction improves after the modifications. It is also noted that the transverse strain (e_2) is not negligible and, in fact, has the same order of magnitude as longitudinal strain (e_1). The data shows that our formulation based on the assumption that the transverse stress (σ_2) equals zero is more effective than that of zero transverse strain (e_2).

The comparisons between the experimental results and numerical results for the torsion test are shown in Figures 2.7 and 2.8. The comparsion indicates the 3D-Beam predictions (modified with warping effect) are close to the experimental results. It is also noted that the shear strain (e_6) is nearly double if the warping effect is included.

Description	LTM-45 (Graphite/Epoxy)
E_x(msi)	18.3
E_y(msi)	1.3
E_s(msi)	0.9
ν_x	0.28

Table 2.1 Ply Properties of LTM-45. E_x is the elastic modulus of the ply in the x (longitudinal axis of the fiber) direction. E_y is the elastic modulus of the ply in the y (transverse) direction. And E_s refers to the shear modulus of the ply.

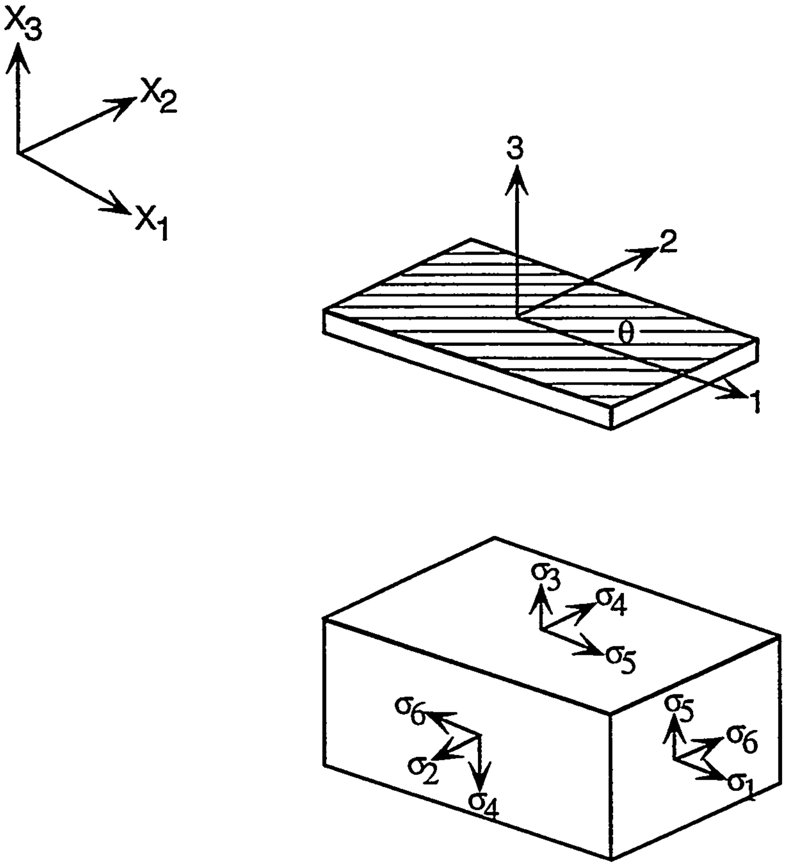

Figure 2.1 Definition of Coordinate System & Notations (X_1 is along the beam axis)

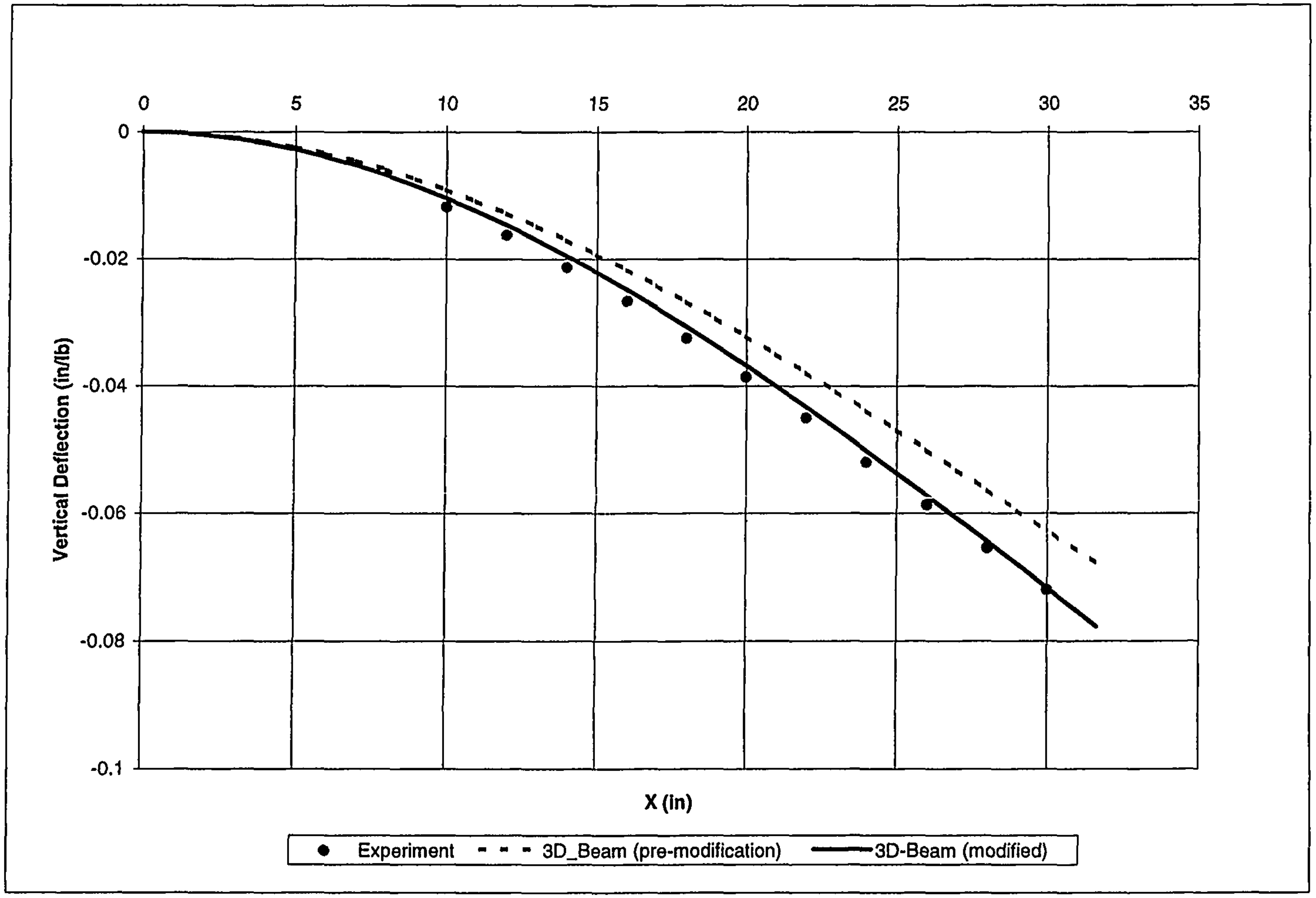

Figure 2.2 Vertical Deflection Under Unit Tip Bending Load of the Aluminum Box Beam (Dimension: 3/4" x 3/4" x32"; skin thickness = 1/16").

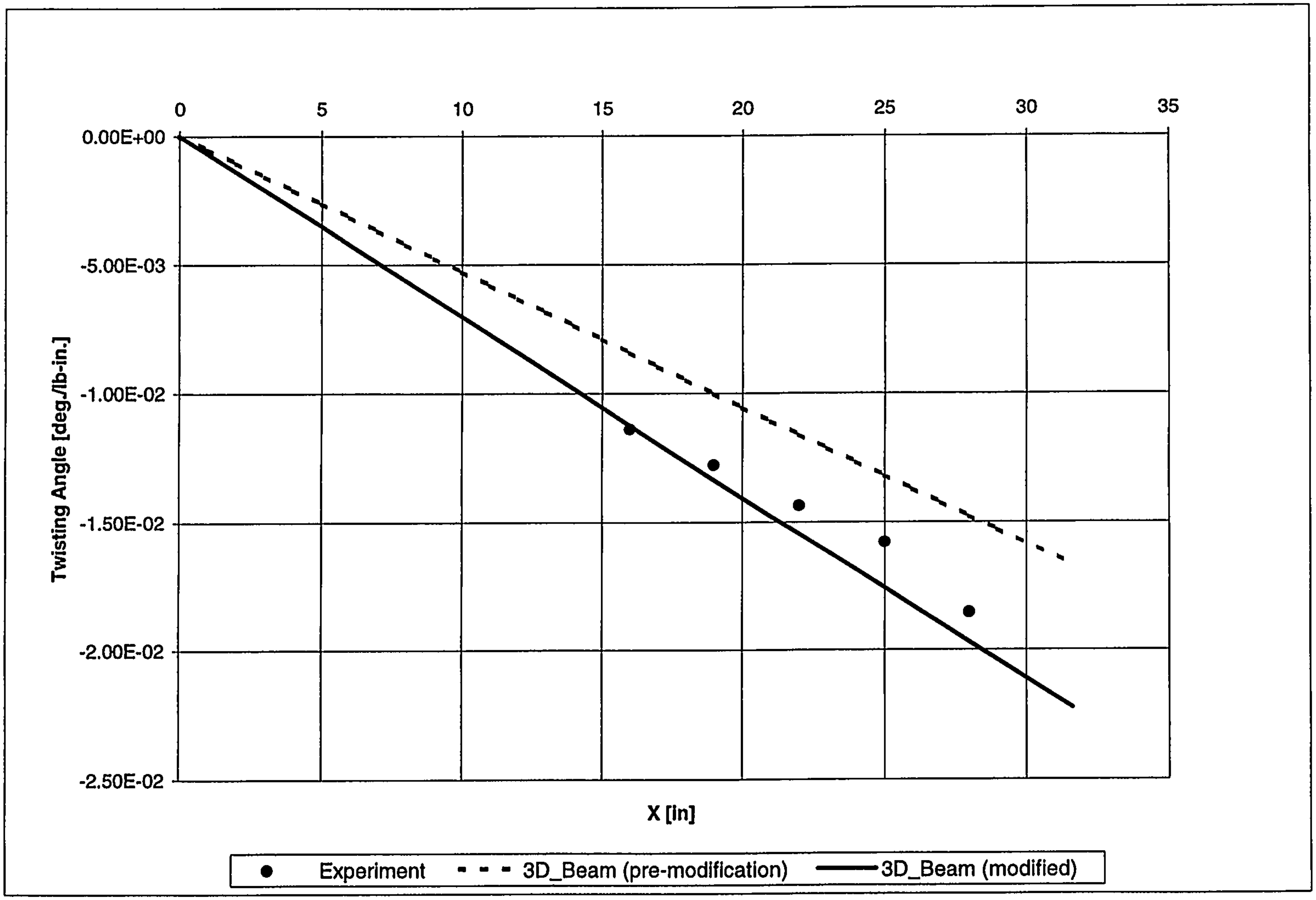

Figure 2.3 Twist Angle Distribution Under Unit Tip Torque Load (1 lb-in.) of the Aluminum Box Beam (Dimension: 3/4" x 3/4" x32"; skin thickness = 1/16").

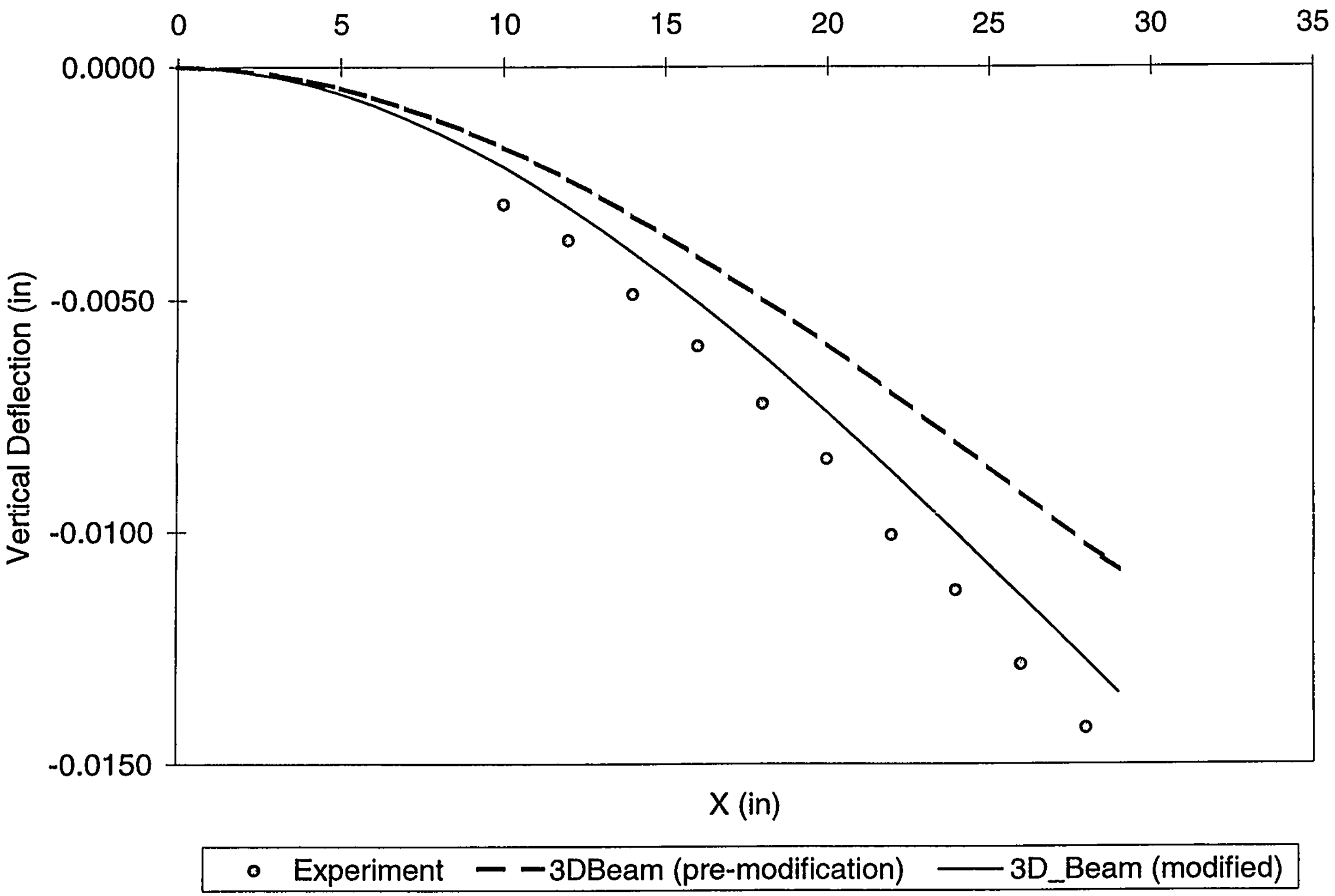

Figure 2.4 Vertical Deflection Under Unit Tip Bending Load of the Composite Box Beam (Dimension: 3" x 1" x 29"; skin laminate lay-up is [±20°$_3$]$_T$).

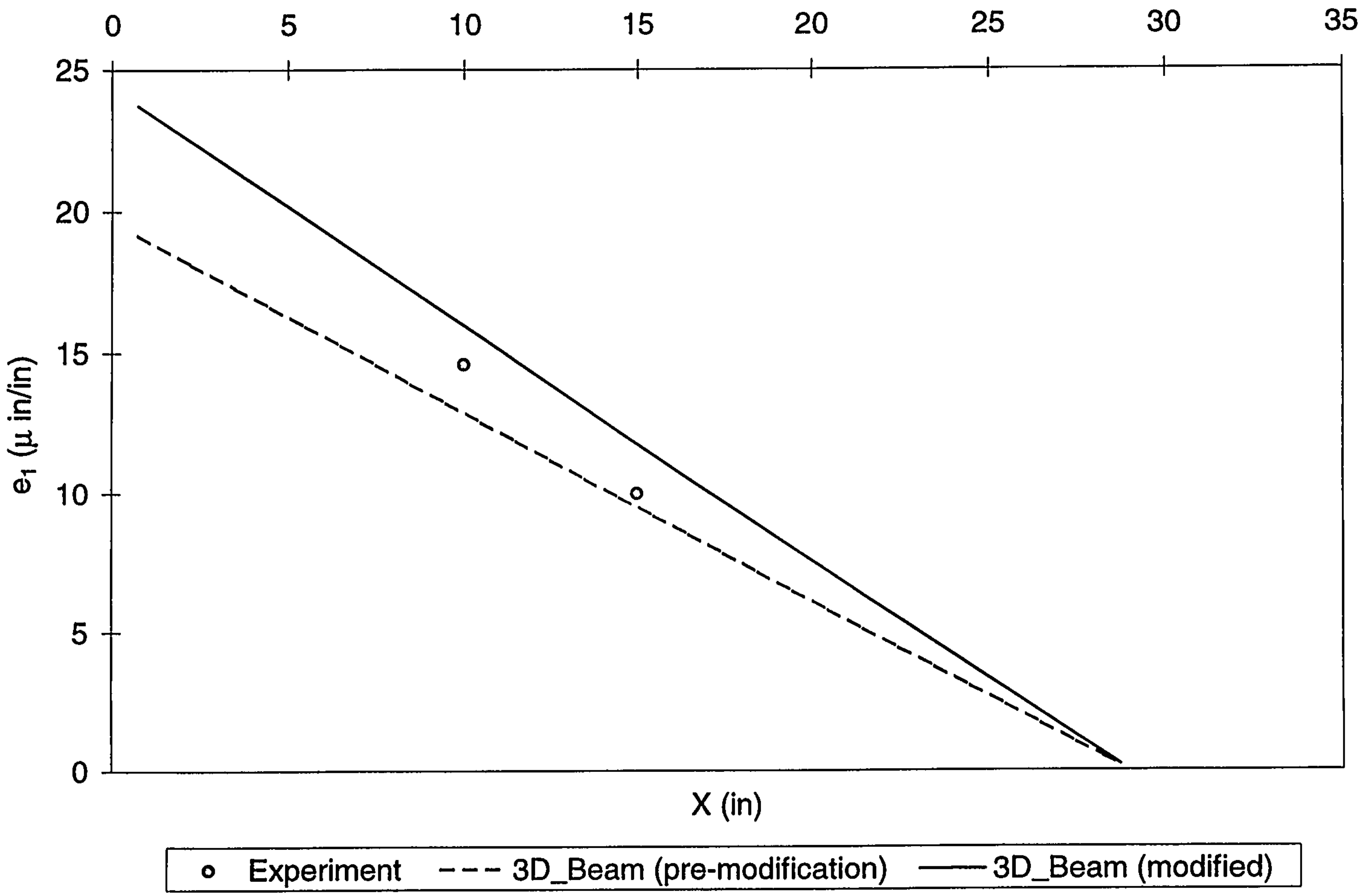

Figure 2.5 Top Skin Longitudinal Strain (e_l) Under Unit Tip Bending Load of the Composite Box Beam (Dimension: 3" x 1" x 29"; skin laminate lay-up is $[\pm20°_3]_T$).

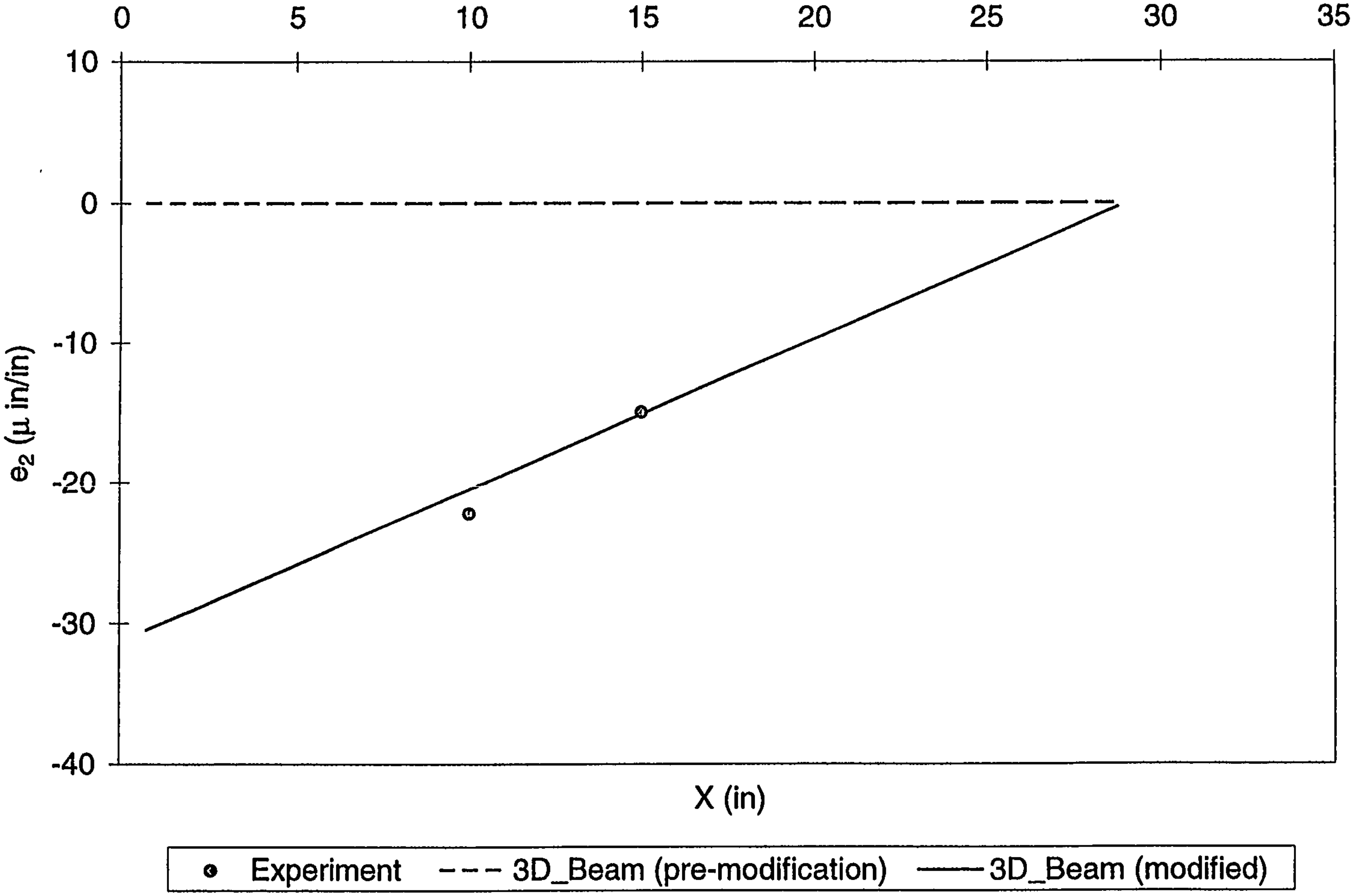

Figure 2.6 Top Skin Transverse Strain (e_2) Under Unit Tip Bending Load of the Composite Box Beam (Dimension: 3" x 1" x 29"; skin laminate lay-up is $[\pm 20°_3]_T$).

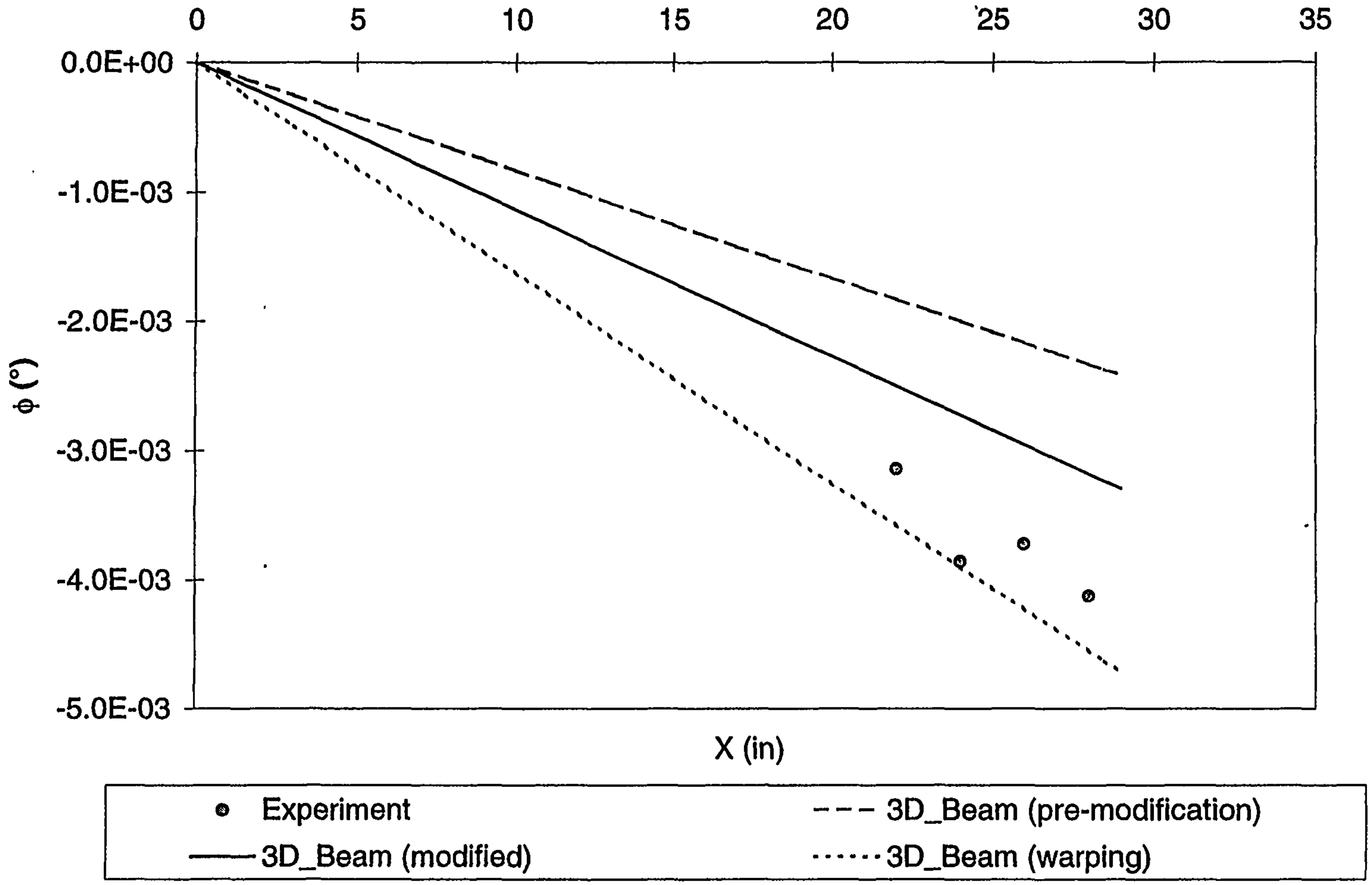

Figure 2.7 Twist Angle Distribution Under Unit Tip Torque Load (1 lb-in.) of the Composite Box Beam (Dimension: 3" x 1" x 29"; skin laminate lay-up is $[\pm 20°_3]_T$).

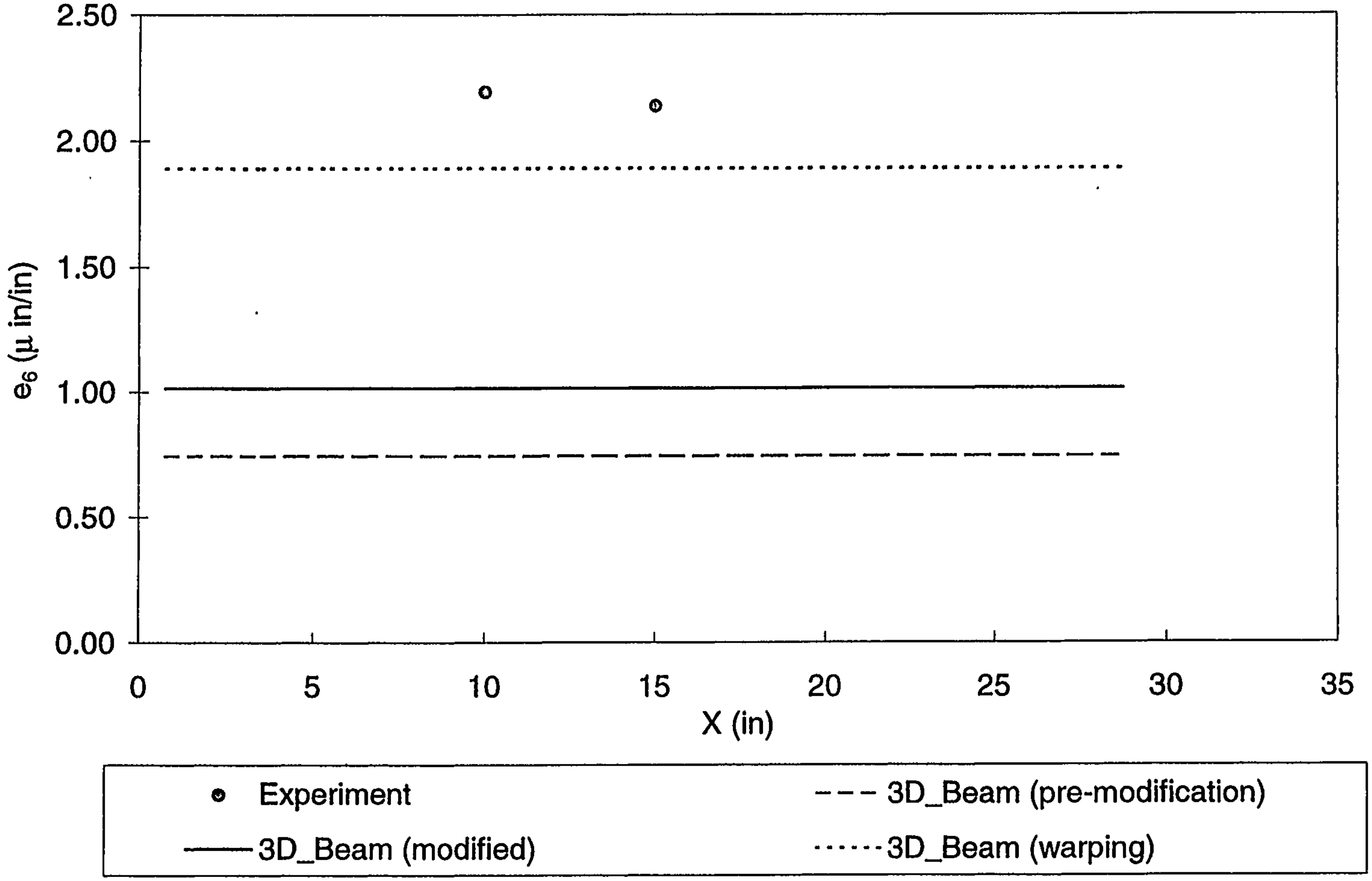

Figure 2.8 Top Skin Shear Strain (e_6) Under Unit Tip Torque Load (1 lb-in.) of the Composite Box Beam (Dimension: 3" x 1" x 29"; skin laminate lay-up is $[\pm 20°_3]_T$).

Chapter 3

Parametric Study

Before we start to design a D-spar that meets specific structural properties and has maximum bend-induced twist, we would like to understand how various design parameters influence the bend-twist coupling coefficient. We first derive a simple expression of the coupling coefficient for a flat-plate laminate. We then use 3D-Beam software to carry out the parametric study for the D-spar.

3.1 Theoretical Estimation of the Coupling Coefficient, α

Instead of immediately performing a numerical estimation of the α interaction parameter for the D-spar, we explored the possibility of estimating the maximum value of the α interaction parameter theoretically to gain some physical insight into bend-twist and extension-twist coupling.

We assume the problem we are looking at is a two-dimensional flat laminate and the in-plane normal stress in the '2' direction has the value of zero; i.e., $\sigma_2 = 0$.

The constituent relationship between stress and strain is

$$\begin{bmatrix} \sigma_1 \\ \sigma_2 \\ \sigma_6 \end{bmatrix} = \begin{bmatrix} Q_{11} & Q_{12} & Q_{16} \\ Q_{21} & Q_{22} & Q_{26} \\ Q_{61} & Q_{62} & Q_{66} \end{bmatrix} \begin{bmatrix} \varepsilon_1 \\ \varepsilon_2 \\ \varepsilon_6 \end{bmatrix} \tag{3.1}$$

If $\sigma_2 = 0$, we can reduce the Qs matrix as follows,

$$\begin{bmatrix} \sigma_1 \\ \sigma_6 \end{bmatrix} = \begin{bmatrix} \overline{Q}_{11} & \overline{Q}_{16} \\ \overline{Q}_{61} & \overline{Q}_{66} \end{bmatrix} \begin{bmatrix} \varepsilon_1 \\ \varepsilon_6 \end{bmatrix}$$

where

$$\overline{Q}_{11} = Q_{11} - \frac{Q_{12} * Q_{21}}{Q_{22}}$$

$$\overline{Q}_{16} = Q_{16} - \frac{Q_{12} * Q_{26}}{Q_{22}}$$

$$\overline{Q}_{61} = Q_{61} - \frac{Q_{62} * Q_{21}}{Q_{22}}$$

$$\overline{Q}_{66} = Q_{66} - \frac{Q_{62} * Q_{26}}{Q_{22}} \tag{3.2}$$

The relationship between the in-plane strains ($\varepsilon_1^0, \varepsilon_6^0$), ($\kappa_1, \kappa_6$) and N_1, N_6, M_1, M_6 is as follows

$$\begin{bmatrix} N_1 \\ N_6 \\ M_1 \\ M_6 \end{bmatrix} = \begin{bmatrix} \overline{A}_{11} & \overline{A}_{16} & \overline{B}_{11} & \overline{B}_{16} \\ \overline{A}_{61} & \overline{A}_{66} & \overline{B}_{61} & \overline{B}_{66} \\ \overline{B}_{11} & \overline{B}_{61} & \overline{D}_{11} & \overline{D}_{16} \\ \overline{B}_{16} & \overline{B}_{66} & \overline{D}_{61} & \overline{D}_{66} \end{bmatrix} \begin{bmatrix} \varepsilon_1^0 \\ \varepsilon_6^0 \\ \kappa_1 \\ \kappa_6 \end{bmatrix} \tag{3.3}$$

where

$$\overline{A}_{ij} = \int \overline{Q}_{ij}\, dz$$

$$\overline{B}_{ij} = \int \overline{Q}_{ij} * z\, dz$$

$$\overline{D}_{ij} = \int \overline{Q}_{ij} * z^2\, dz$$

$\varepsilon_1^0, \varepsilon_6^0$: in – plane normal and shear strains

κ_1, κ_6 : bending and twisting curvatures

N_1, N_6 : in-plane normal force and shear force per unit width

M_1, M_6 : bending moment and twisting moment per unit width

z : the vertical distance between the mid-plane and the ply layer

For a symmetric (symmetry with respect to the mid-plane) laminate, the relation reduces to

$$\begin{bmatrix} N_1 \\ N_6 \\ M_1 \\ M_6 \end{bmatrix} = \begin{bmatrix} \overline{A}_{11} & \overline{A}_{16} & 0 & 0 \\ \overline{A}_{61} & \overline{A}_{66} & 0 & 0 \\ 0 & 0 & \overline{D}_{11} & \overline{D}_{16} \\ 0 & 0 & \overline{D}_{61} & \overline{D}_{66} \end{bmatrix} \begin{bmatrix} \varepsilon_1^0 \\ \varepsilon_6^0 \\ \kappa_1 \\ \kappa_6 \end{bmatrix} \tag{3.4}$$

For a symmetric laminate, there are two types of coupling:

a. Extension – Shear coupling

b. Bend – Twist coupling.

For an anti-symmetric laminate, the relation reduces to

$$\begin{bmatrix} N_1 \\ N_6 \\ M_1 \\ M_6 \end{bmatrix} = \begin{bmatrix} \overline{A}_{11} & 0 & 0 & \overline{B}_{16} \\ 0 & \overline{A}_{66} & \overline{B}_{61} & 0 \\ 0 & \overline{B}_{61} & \overline{D}_{11} & 0 \\ \overline{B}_{16} & 0 & 0 & \overline{D}_{66} \end{bmatrix} \begin{bmatrix} \varepsilon_1^0 \\ \varepsilon_6^0 \\ \kappa_1 \\ \kappa_6 \end{bmatrix} \tag{3.5}$$

In this case, the coupling is different from the previous case. The couplings are

a. Extension – Twist coupling

b. Bend – Shear coupling.

If a laminate is not symmetric or anti-symmetric, there will be more than two modes of coupling. The stiffness and compliance matrix will be fully populated.

How do the $\overline{A}_{ij}, \overline{B}_{ij}, \overline{D}_{ij}$ values relate to the "EI", "GJ" and "g" of Lobitz's work? Let us reprint some of the equations in Lobitz's work[9] that are applicable to our derivation. The equations that Lobitz used for the extension-twist coupling are given in matrix form below:

$$\begin{bmatrix} EA & -g \\ -g & GJ \end{bmatrix} \begin{bmatrix} \dfrac{\partial u}{\partial x} \\ \dfrac{\partial \varphi}{\partial x} \end{bmatrix} = \begin{bmatrix} F \\ M_t \end{bmatrix}$$ (Eq. 1 in Lobitz and Veers[9])

$$\begin{bmatrix} EI & -g \\ -g & GJ \end{bmatrix} \begin{bmatrix} \dfrac{\partial \theta}{\partial x} \\ \dfrac{\partial \varphi}{\partial x} \end{bmatrix} = \begin{bmatrix} M_b \\ M_t \end{bmatrix} \cdot$$ (Eq. 6 in Lobitz and Veers[9])

The terms are defined in Lobitz.[9] For the strain terms, the terms $\frac{\partial u}{\partial x}$, $\frac{\partial \varphi}{\partial x}$ and $\frac{\partial \theta}{\partial x}$ equal to ε_1^0, κ_6 and κ_1 respectively. For the force terms, the F, M_t and M_b equal to b*N_1 b*M_6 and b*M_1 respectively. The parameter "b" is the width of the flat laminate.

The "EI", "GJ", "g" can be expressed by Aij, Bij and Dij as follows:

Bend-Twist Coupling (Symmetry)

$$\overline{D}_{11} = \frac{EI}{b}$$

$$\overline{D}_{66} = \frac{GJ}{b}$$

$$\overline{D}_{16} = -\frac{g}{b}$$

$$\alpha = \frac{g}{\sqrt{EI * GJ}} = -\frac{\overline{D}_{16}}{\sqrt{\overline{D}_{11} * \overline{D}_{66}}}$$

If a laminate has a lay-up of $[\theta]_S$ (single orientation), the α is further reduced to

$$\alpha = -\frac{\overline{Q}_{16}}{\sqrt{\overline{Q}_{11} * \overline{Q}_{66}}} = -\frac{Q_{16} * Q_{22} - Q_{12} * Q_{26}}{\sqrt{(Q_{11} * Q_{22} - Q_{12}^2) * (Q_{66} * Q_{22} - Q_{26}^2)}} \qquad (3.6)$$

Extension-Twist Coupling (Antisymmetry)

$$\overline{A}_{11} = \frac{EA}{b}$$

$$\overline{D}_{66} = \frac{GJ}{b}$$

$$\overline{B}_{16} = -\frac{g}{b}$$

$$\alpha = \frac{g}{\sqrt{EA * GJ}} = -\frac{\overline{B}_{16}}{\sqrt{\overline{A}_{11} * \overline{D}_{66}}}$$

If a laminate has a lay-up of $[\theta]_{AS}$ (single orientation), the α is further reduced to

$$\begin{aligned} \alpha &= -\sqrt{\frac{3}{4}} * \frac{\overline{Q}_{16}}{\sqrt{\overline{Q}_{11} * \overline{Q}_{66}}} \\ &= -\sqrt{\frac{3}{4}} * \frac{Q_{16} * Q_{22} - Q_{12} * Q_{26}}{\sqrt{(Q_{11} * Q_{22} - Q_{12}^2) * (Q_{66} * Q_{22} - Q_{26}^2)}} \end{aligned} \tag{3.7}$$

The α interaction parameters are related to the normal coupling coefficient (ν_{16}) and the shear coupling coefficient (ν_{61}). The two coefficients are defined as follows[12]:

$$\nu_{16} = \frac{Q_{12} * Q_{26} - Q_{22} * Q_{16}}{Q_{11} * Q_{22} - Q_{12}^2}$$

$$\nu_{61} = \frac{Q_{12} * Q_{26} - Q_{22} * Q_{16}}{Q_{22} * Q_{66} - Q_{26}^2} \tag{3.8}$$

Therefore, the α interaction parameters are reduced to the simplest form:

Bend-Twist Coupling

$$\alpha^2 = \nu_{16} * \nu_{61} \tag{3.9}$$

Extension-Twist Coupling

$$\alpha^2 = \frac{3}{4} * \nu_{16} * \nu_{61} \tag{3.10}$$

It is interesting to note that after all the algebraic manipulations, we have obtained a simple form for the α interaction parameter for a flat-plate laminate. This leads to some physical insights: first, the interaction parameter, α, is highly dependent on the ply material, since both the ν_{16} and ν_{61} coefficients are material-dependent; second, the geometry parameters do not appear in the simplified equation. This implies that the geometrical parameters may not affect the determination of the range of the α. However, for the second observation, we are dealing with a simple type of laminate; that is a flat surface, symmetric or anti-symmetric laminate.

Two typical ply materials, a) T800/3900-2 (Graphite/Epoxy) and b) Scotchply (Glass/Epoxy) are being studied. The ply properties of these materials are given in Table 3.1. The α interaction parameters for a flat plate laminate made out of these two types of materials are shown in Figure 3.1.

It is clearly seen that the range of α interaction parameters depends very much on the type of material chosen. Graphite/Epoxy has a maximum value close to 0.8, and Glass/Epoxy has a maximum value close to 0.5. The maximum values of α for these materials occur at different ply orientations. In general, we can state that the higher values of α occur in ply orientation, θ, between 15° and 30°. In subsequent sections, we look into other parameters that affect the α interaction parameters numerically.

3.2 Numerical Estimation of the Coupling Coefficient, α

3.2.1 D-spar Geometry

In the numerical study, we study a D-spar composite structure, which is part of the airfoil shape. The basic dimension of the D-spar is 72" (long), 6" (wide) and 3" (height) as shown in Figure 3.2. The radius of the semi-circle is 1.5”. Effectively, the width of the horizontal surface is 4.5".

The lay-up sequence at the top and bottom surface affects the lay-up sequence at the left vertical and right semi-circular walls. If the top and bottom laminates are symmetric lay-ups, then the lay-up at the two walls will be anti-symmetric. On the other hand, if the top and bottom laminates are anti-symmetric lay-ups, then the lay-up at the two walls will be symmetric.

We also need to standardize the lay-up notation. The notation $[\theta_n]_s$ refers to 'n' layers of θ ply, and the subscript 's' denotes that the lay-up is symmetric in reference to the mid-plane between top and bottom surfaces. The notation $[\theta_n]_{AS}$ refers to 'n' layers of θ ply, and the subscript 'AS' denotes that the lay-up is anti-symmetric in reference to the mid-plane between top and bottom surfaces.

3.2.2 Parametric Study

In this parametric study we investigate various parameters that affect the range of α interaction parameters (mainly for Bend-Twist coupling). The parameters that we have considered are:

a. geometry,

b. ply materials (Graphite/Epoxy and Glass/Epoxy),

c. laminate thickness,

d. volumetric fraction of the anisotropy,

e. internal spar or rib,

f. hybrid materials,

g. mixtures of extension-twist and bend-twist lay up,

h. torsion-related out-of-plane warping, and

i. others such as

   (i) configurations that exhibit the same "α" but have different "EI" and "GJ"

   (ii) configurations that exhibit different "α" but have the same "EI" and "GJ"

3.2.2.1 Geometry Effect

We looked into two different cross-sectional dimensions of the D-spar: a) 6" x 3" and b) 6" x 4". The results are shown in Figures 3.3a-c. The α interaction parameter does change as we change the height of the D-spar. However, the variation is negligible.

A relevant case for wind turbine blades is to compare the D-spar with an airfoil shape. We compute the α interaction parameter for a 3-inch thick NACA0012 airfoil (25" chord) and compare the results against the 6" x 3" D-spar. We observe that there are negligible effects from the geometry factor in the case of the thin-wall assumption as seen in Figure 3.3b.

We assume that the transverse shear through the thickness is negligible in the thin-wall case. On the other hand, the transverse shear effect is included in the thick-wall formulation. This leads to increasing the torsion rigidity of the D-spar and results in a smaller α as seen in Figure 3.3d. Since the wall thickness (0.2" to 0.3") of the D-spar is small as compared with the height (3" to 4") of the D-spar, the thin-wall formulation is more appropriate .

3.2.2.2 Material Effect

From the theoretical estimation of the α interaction parameter, we find that the α is highly dependent on the types of material used. For the D-spar, we also expect to see a significant effect of the material as we look at both the Graphite/Epoxy and Glass/Epoxy. The numerical results are shown in Figures 3.4a-c. The maximum α achievable for the graphite and glass materials is 0.62 and 0.42 respectively. The results indicate that the ratio of the maximum α for the two materials is about 3/2 (Graphite/Glass).

3.2.2.3 Thickness Effect

We have two approaches to studying the effects of the laminate thickness. The first approach is to fix the ply distribution, but to increase or decrease the total laminate thickness. For example, if we have a $[\theta_n/\phi_m]_S$ laminate, the distribution ratio is n/m(or m/n). If we assume each ply has the same thickness (t), then the total thickness is (m+n)*t. We proceed with changing the total thickness by varying the "m", "n" layers of plies but keeping the distribution ratio (n/m or m/n) constant. With this arrangement, we see that the α interaction parameter remains constant as shown in Figure 3.5a.

The second approach is to keep the total laminate thickness constant and vary the distribution ratio. We looked into various configurations. We observed that the α interaction parameter varies with the distribution ratio as in Figure 3.5b.

3.2.2.4 Anisotropy Volumetric Effect

Figure 3.5 indicates that the volumetric distribution of the ply within the laminate has a dominant effect on the α interaction parameter. To further study this effect we looked into a laminate that has ply orientation, $[20_n/[45/-45]_m]_S$, where m=2, 3, 4. We then varied the parameter 'n' to simulate change in the total thickness as well as the distribution ratio (the volume fraction V_a of anisotropic fibers is then n/(2*m+n)). The results are shown in Figure 3.6. The upper portion of the figure shows that for the same number of 20° plies but different values of V_a, we have different values of α. However, if we adjust the number of layers of 20° plies (n) in such a way that the three configurations have the same value of V_a, we will get a single value of α as seen in the lower portion of Figure 3.6.

Therefore, for a laminate with a fixed set of ply orientations, the α interaction parameter for that laminate is determined by the volume fraction of the anisotropic plies regardless of distribution ratio.

3.2.2.5 Internal Spar Effects

An internal spar is inserted at the end-edge of the semi-circle as shown in Figure 3.7. The insertion of an internal spar increases the "EI" and "GJ", and will result in a reduction of the α interaction parameter. We look into both the effects of the thickness and ply orientation of the internal spar. If we increase the thickness of the internal spar while having the same ply orientation, the α interaction parameter reduces, as shown in Figure 3.8.

The next case considered the constant thickness of the internal spar while varying the ply orientation of the internal spar. The result is shown in Figure 3.9a. The result indicates that the ply orientation of the D-spar has small effect on the α interaction parameter. The variation of the α interaction parameter with and without an internal spar is about 10%.

In fact, the internal spar has changed significantly the stiffness properties of the D-spar in the lead-lag direction. Figure 3.9b shows the D_{ij} of the D-spar with and without an internal spar (same thickness but different orientation). We can see that the D_{22} (lead-lag) changes substantially.

3.2.2.6 Hybrid Materials Effect

To study this effect, we looked at three baseline configurations and compared their results against the same configurations with hybrid material (for all the cases we substituted graphite/epoxy for glass/epoxy). The three configurations we studied are $[\theta(T800)_5/\theta(Scotchply)_5]_S$, $[\theta(T800)_5/0(Scotchply)_5]_S$, $[\theta(T800)_5/90(Scotchply)_5]_S$ and the results are shown in Figures 3.10a-c.

In the first case, we have 50% graphite fibers and 50% glass fibers all at the same ply orientation. The α interaction parameter of this hybrid case should be lower than the all-graphite case and higher than the all-glass case (see Figure 3.10a). Therefore, the reduction or increase of α depends on the baseline configurations. The lower bound of the α interaction parameter is limited by the low-performance fibers (glass) and the upper bound is limited by the high-performance fibers (graphite).

In the second case (see Figure 3.10b), the change is at the 0° material. We replaced 0° graphite fibers with 0° glass fibers or vice versa. The substantial change in α comes mainly from a large change in "EI" because the ratio of the E_x (graphite/fiber) is about 4 to 1. We can deduce that if the volume fraction of non-anisotropic fibers is of lower stiffness than the anisotropic ones, then we can achieve a higher α value.

In the third case (see Figure 3.10c), the change is at the 90° material. We replaced 90° graphite fibers with 90° glass fibers or vice versa. The change in α is marginal because there is marginal change in the E_y (transverse ply stiffness) and the E_s (shear modulus) for both materials.

In fact, the dominant effect of using hybrid materials is the significant change in flapping stiffness as shown in Figure 3.11. Note that the change of D_{12} between the solid and hollow cross sections cannot be seen in Figure 3.11 because the change is small

3.2.2.7 The Effect of Mixtures of Antisymmetry and Symmetry Lay-Up

Until now we have been looking at a D-spar with symmetric lay-up, and the behavior of the D-spar is quite clear (bend-twist or tension-shear mode). If we replace some of the symmetric lay-up with an anti-symmetric lay-up, the behavior of the D-spar will be very complicated. The following matrices show the change in stiffness matrix from the symmetric ply lay-up to the mixture of symmetric and antisymmetric ply lay-up.

$$\begin{bmatrix} \overline{A}_{11} & \overline{A}_{16} & 0 & 0 \\ \overline{A}_{61} & \overline{A}_{66} & 0 & 0 \\ 0 & 0 & \overline{D}_{11} & \overline{D}_{16} \\ 0 & 0 & \overline{D}_{61} & \overline{D}_{66} \end{bmatrix} \rightarrow \begin{bmatrix} A_{11} & A_{16} & 0 & B_{16} \\ A_{61} & A_{66} & B_{61} & 0 \\ 0 & B_{61} & D_{11} & D_{16} \\ B_{16} & 0 & D_{61} & D_{66} \end{bmatrix}$$

Symmetry → *mixture* [*symmetry* & *antisymmetry*]

Instead of just bend-twist coupling for the symmetric lay-up, we have complex coupling among bend, twist and shear modes. In fact, the compliance matrix of this mixture is fully populated, therefore it is difficult to control the desired mode of coupling. In addition to that, the α interaction parameter reduces as we increase the degree of mixture as shown in Figure 3.12. The insertion of core is just to clarify the notation, and it does not affect the calculation. The term "core" signifies that the D-spar is hollow.

3.2.2.8 Torsion-Related Out-of-Plane Warping

The effect of warping on the α interaction parameter is hard to evaluate. The reason is that it is difficult to include a warping function applicable to all cases in the 3D-Beam software. The warping function depends greatly on the geometry of the cross-sectional shape. We assume the shape of the D-spar is "similar" to the shape of a rectangular section, therefore, a simple bi-linear warping function was implemented in the 3D-Beam.

The torsion-related warping, as seen in Figures 3.13a-b, generally increases the α interaction parameter. The changes in the α values come from the reduction in "GJ" and increase in the "coupling" stiffness, while the "EI" remains unchanged. For other cross-section shapes, we expect the α will change if the torsion-related warping is included.

3.2.2.9 Others

The α interaction parameter is a relative value, because it is just a square-root ratio of the coupling term to the cross product of the "EI" and "GJ". It is possible to find two or more configurations of the ply lay-up having different cross-coupling stiffnesses, "EI" and "GJ", but having the same α values. Figure 3.6 has already implicitly indicated such combinations of "coupling" stiffness, "EI" and "GJ", that can give rise to the same α value. The control parameter for this case is the ratio of the volume of the anisotropic lay-up to the volume of the orthotropic lay-up. The control parameter may not be obvious in some cases. For example, the following two lay-ups, a) $[\theta_5/0_5]_S$ and b) $[\theta_4/(0/90)_3]_S$, have similar α values but different stiffness terms as shown in Figure 3.14. Such configurations are, in fact, found by trial-and-error.

The other observation is that "EI" and "GJ" are symmetric terms, since the terms do not change as the sign of the lay-up angle (θ) changes. However, the bend-twist coupling term will change sign if the sign of the ply angle changes. Therefore, we can make use of such features to design the lay-up configurations that have the same "EI" and "GJ" but different α values as seen in Figure 3.15. In this case, the key parameter for such designs is the angle ply lay-up.

3.3 Summary

We identified two key parameters that significantly affect the magnitude of α in the theoretical evaluation. The two key parameters are the ply orientation angle and the materials of the laminate. A higher α value is achieved for the ply angle range between 15° and 30°. A higher α value can also be obtained by using a high-performance laminate such as Graphite/Epoxy.

We also looked into various parameters that affect the magnitude of α in the numerical evaluation. Among the parameters studied, the three key parameters are the ply orientation angle, the laminate material and the volume of anisotropy lay-up relative to the volume of orthotropic lay-up. A hybrid material lay-up will increase α if we are starting with a soft material. Other parameters such as the geometry, the inclusion of the internal rib, the mixture of the extension-twist and bend-twist lay-up, change the magnitude of the α, but the effect is not significant. Torsion-related warping can have a large effect on estimates of α. However, the effect depends on the shape of the cross section. In the selected D-spar, the effect on α from warping is marginal but tends to increase the α estimate.

We also realize through this study that the α interaction parameter is a relative value. There are many ways (configurations) to get the same α with different values of the stiffness terms.

Description	T800/3900-2 (Graphite/Epoxy)	Scotchply (Glass/Epoxy)
E_x(msi)	23.2	5.6
E_y(msi)	1.0	1.2
E_s(msi)	0.9	0.66
ν_x	0.28	0.3

Table 3.1 Ply Properties of T800/3900-2 and Scotchply. E_x is the elastic modulus of the ply in the x (longitudinal axis of the fiber) direction. E_y is the elastic modulus of the ply in the y (transverse) direction. And E_s refers to the shear modulus of the ply.

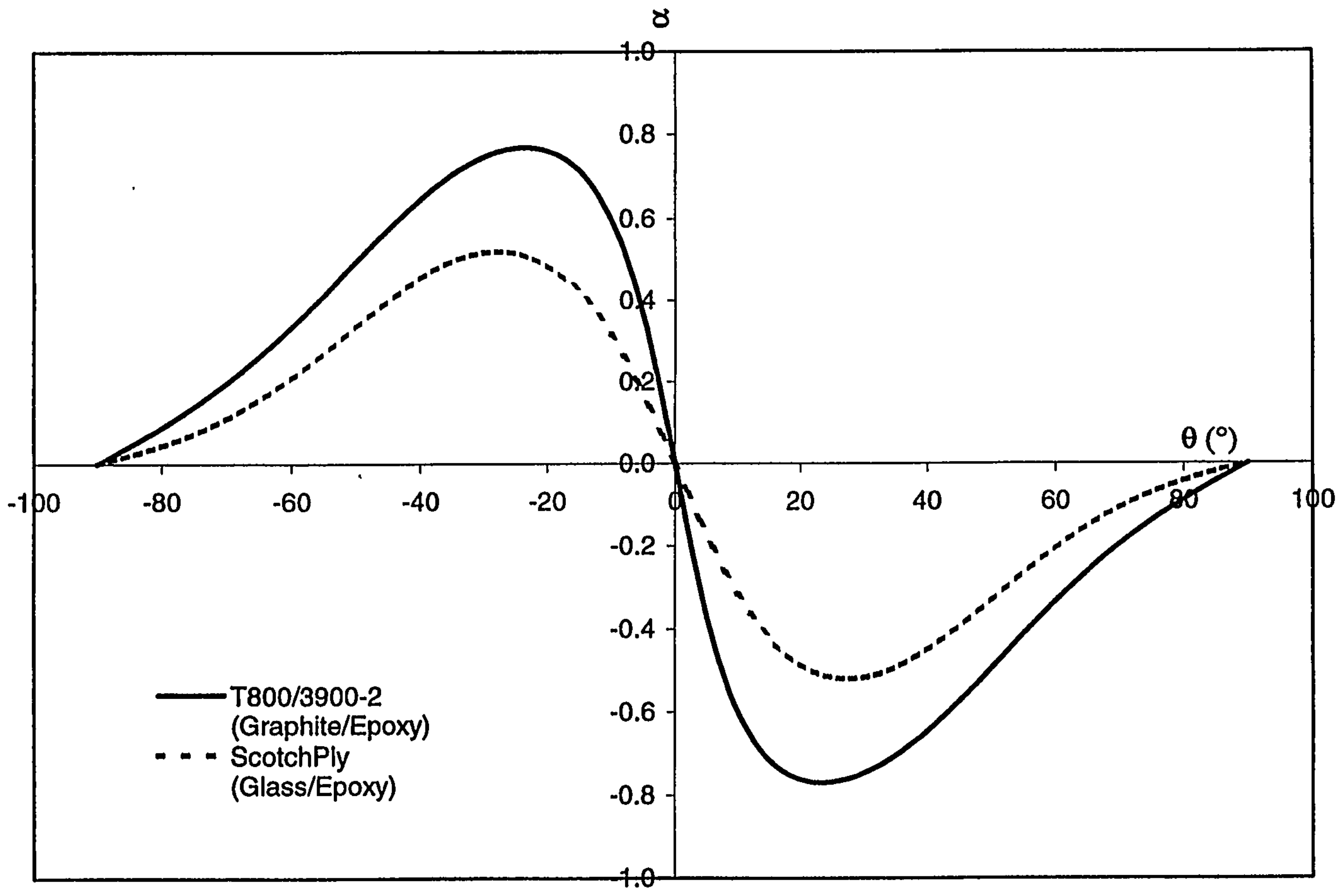

Figure 3.1 The Coupling Coefficient, α, of a Graphite/Epoxy and Glass/Epoxy Flat Laminate.

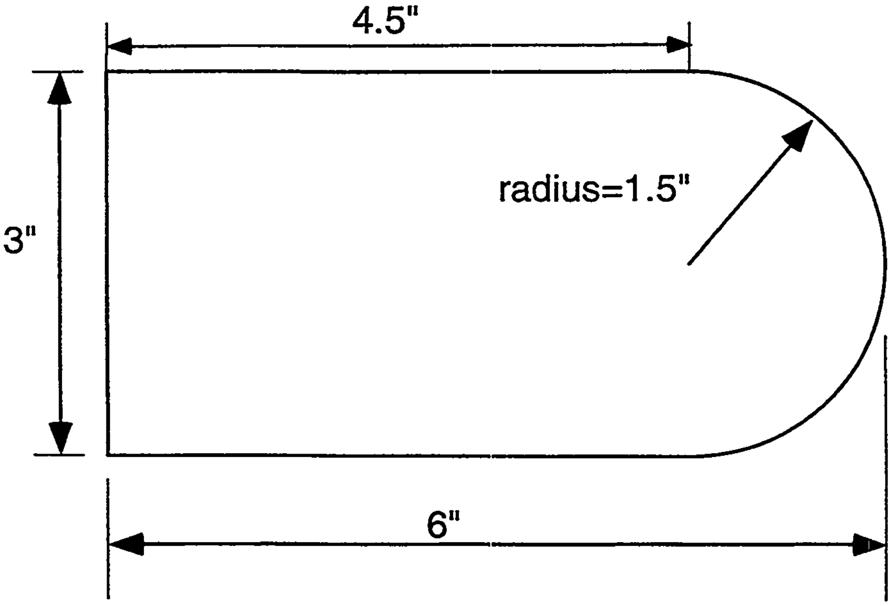

Figure 3.2 D-spar Cross-Section Shape

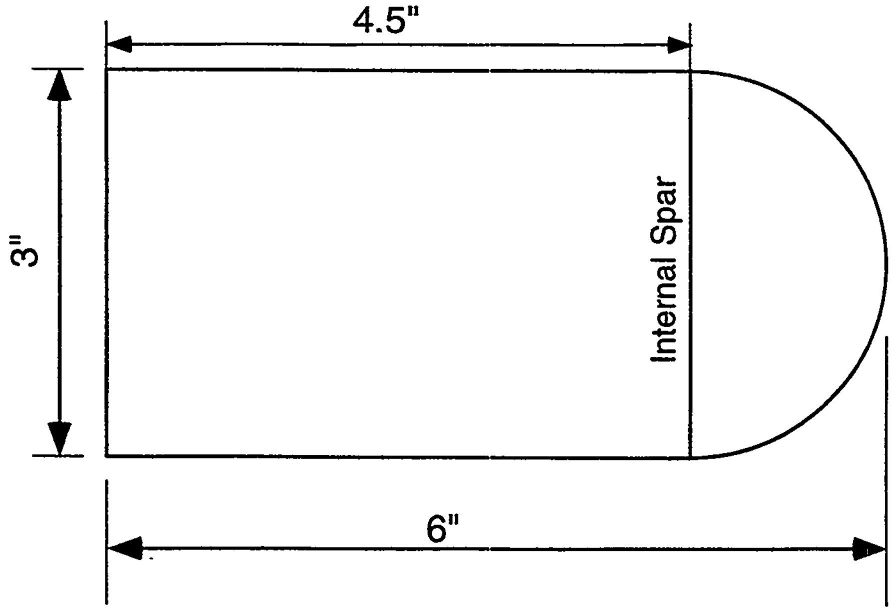

Figure 3.7 D-spar with Internal Spar

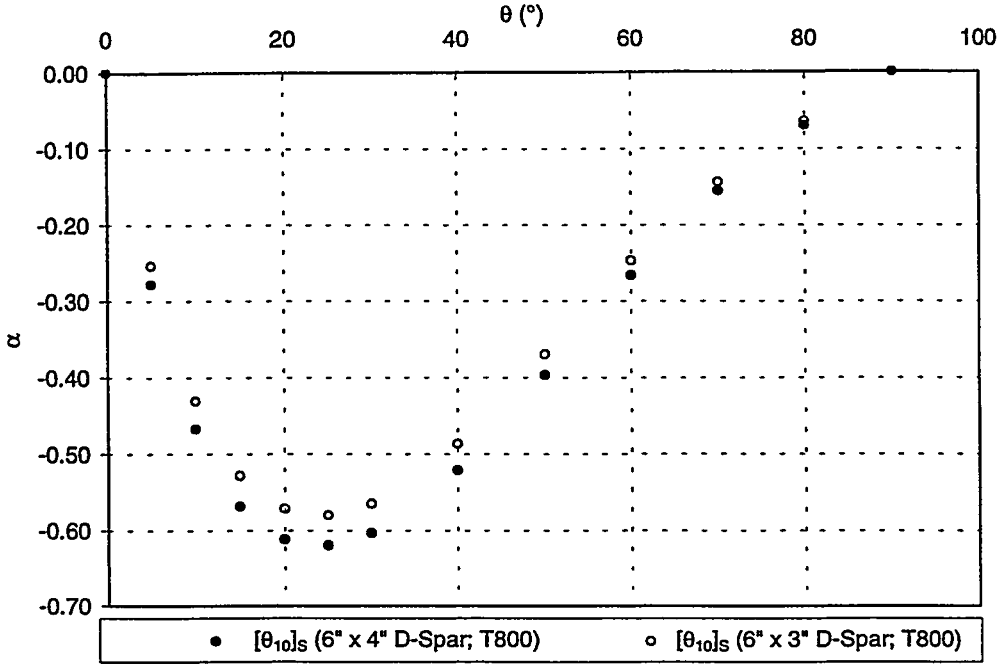

Figure 3.3a The Effect of Geometry on α Interaction Parameter for $[\theta_{10}]_S$ lay-up

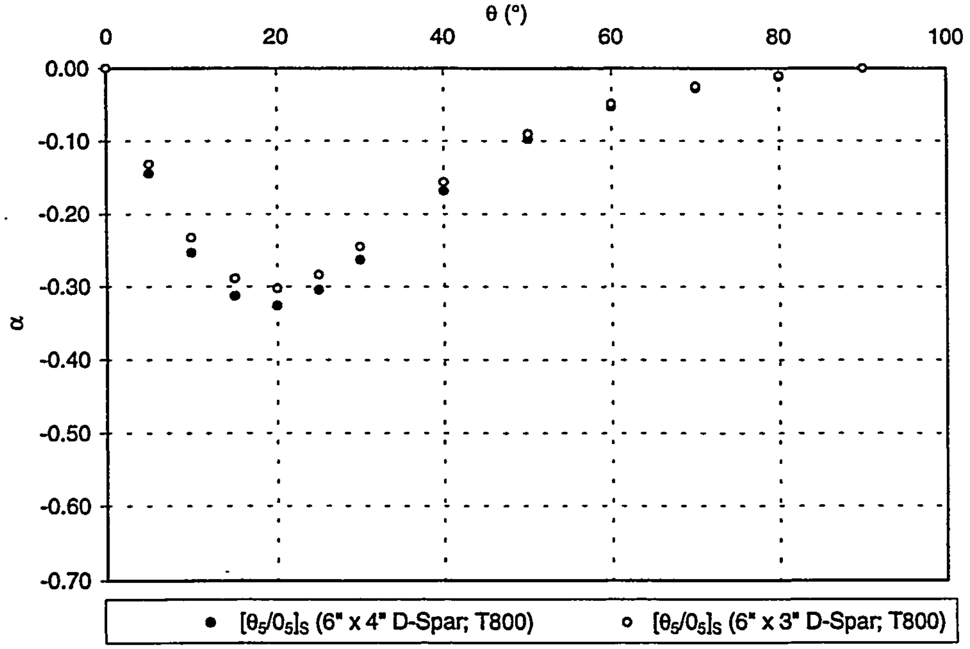

Figure 3.3b The Effect of Geometry on α Interaction Parameter for $[\theta_5/0_5]_S$ lay-up

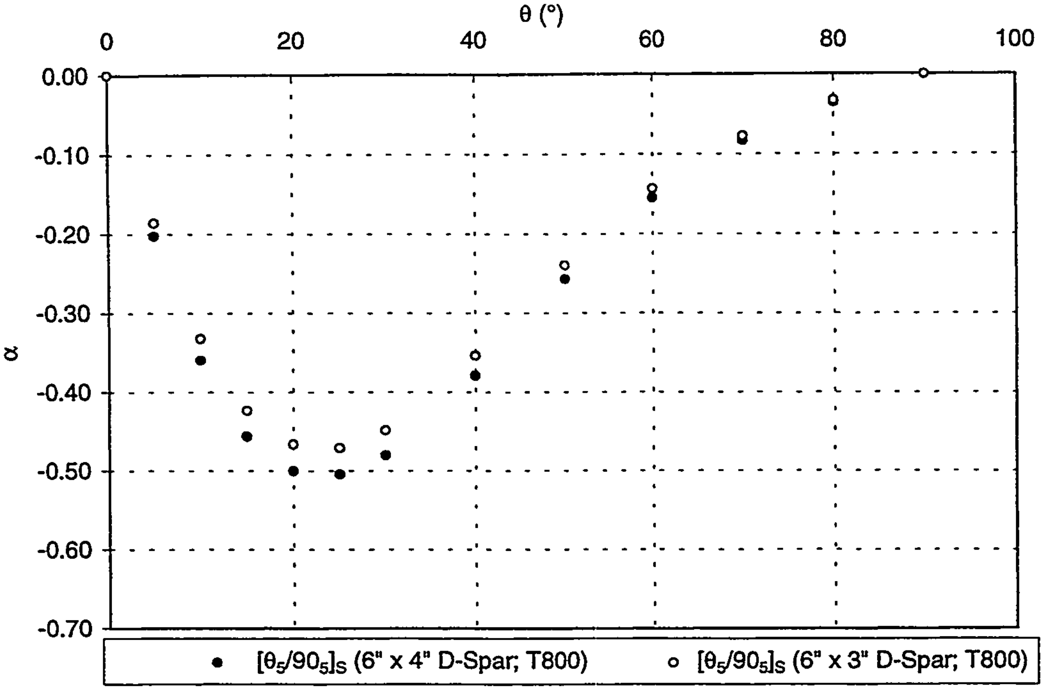

Figure 3.3c The Effect of Geometry on α Interaction Parameter for $[\theta_5/90_5]_S$ lay-up

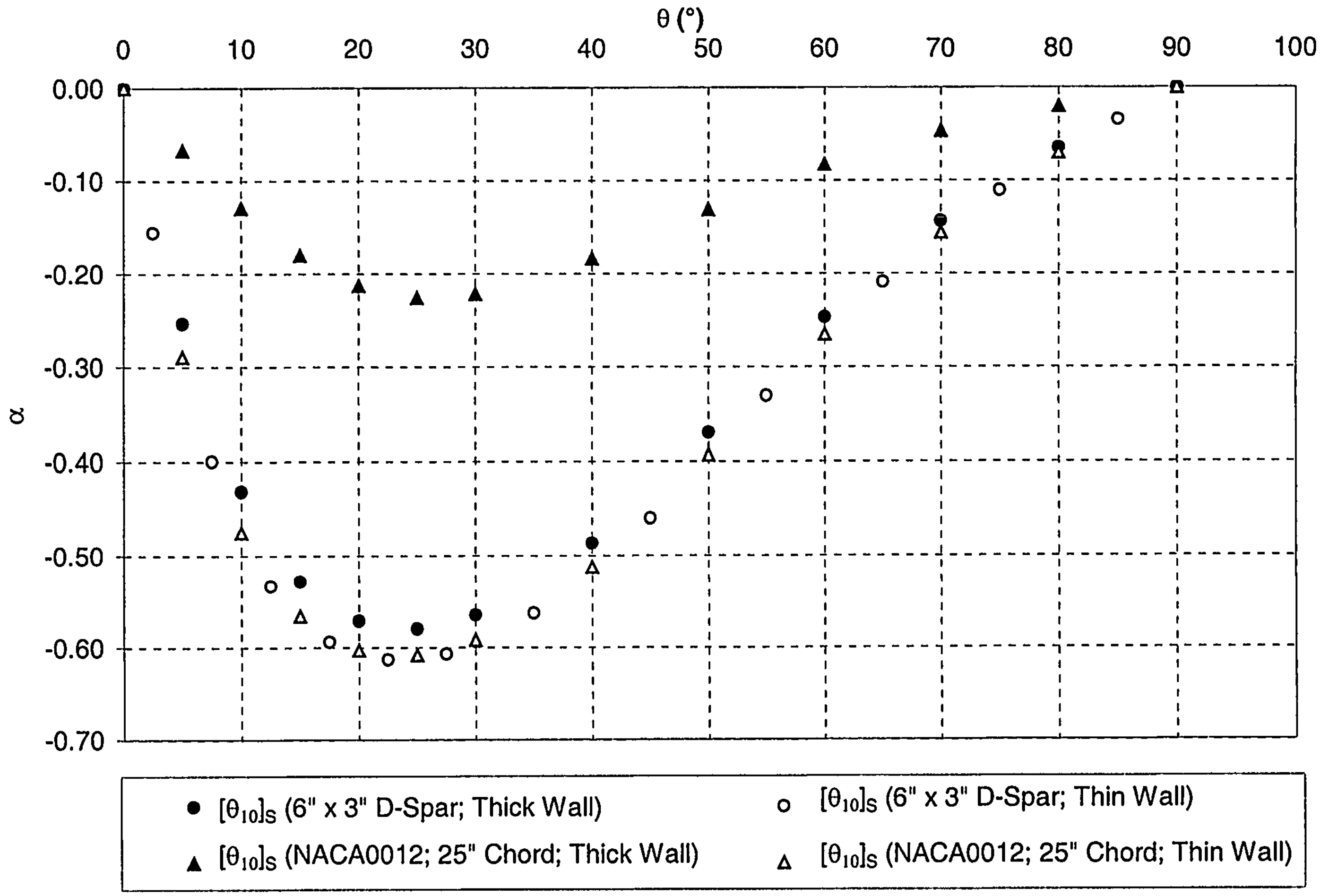

Figure 3.3d The Effects of Thick/Thin Wall Assumption on α Interaction Parameter

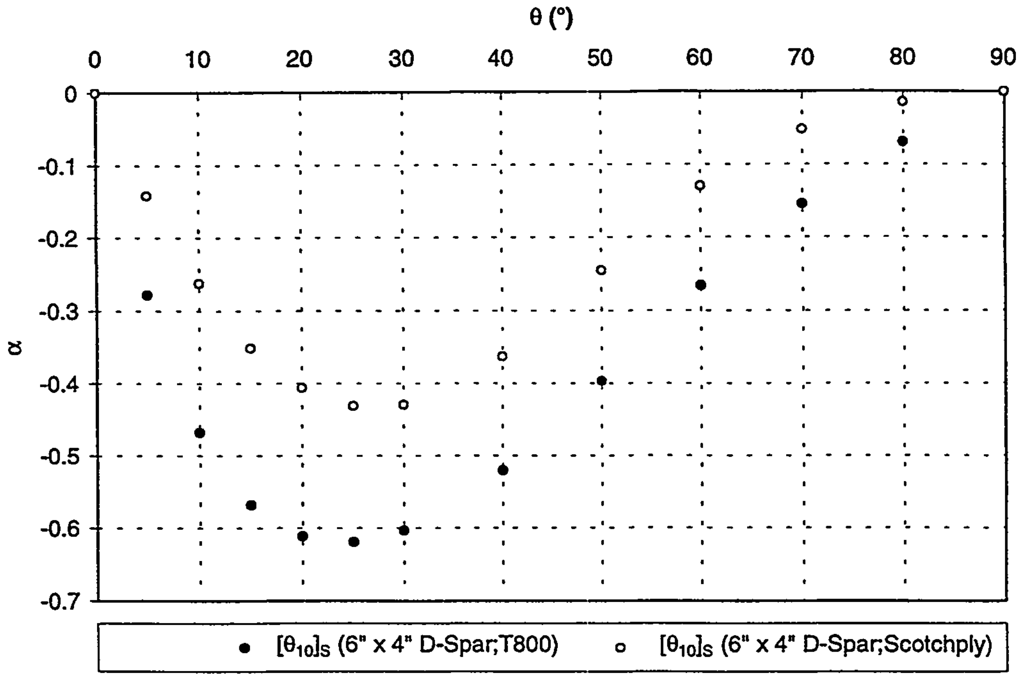

Figure 3.4a The Effects of Materials on α Interaction Parameter for $[\theta_{10}]_S$ lay-up

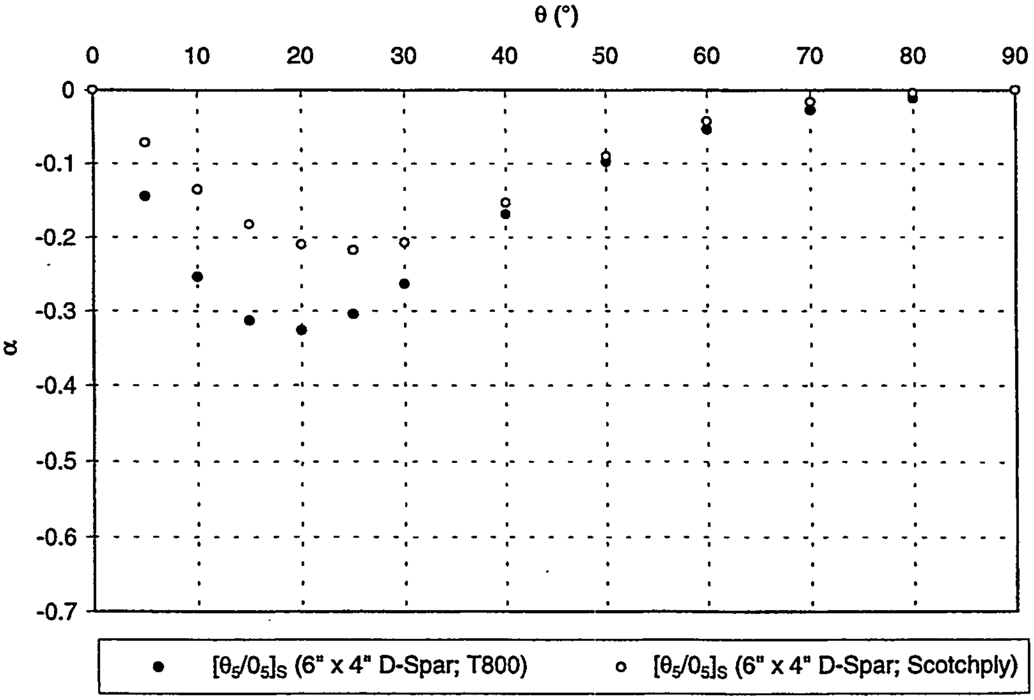

Figure 3.4b The Effects of Materials on α Interaction Parameter for $[\theta_5/0_5]_S$ lay-up

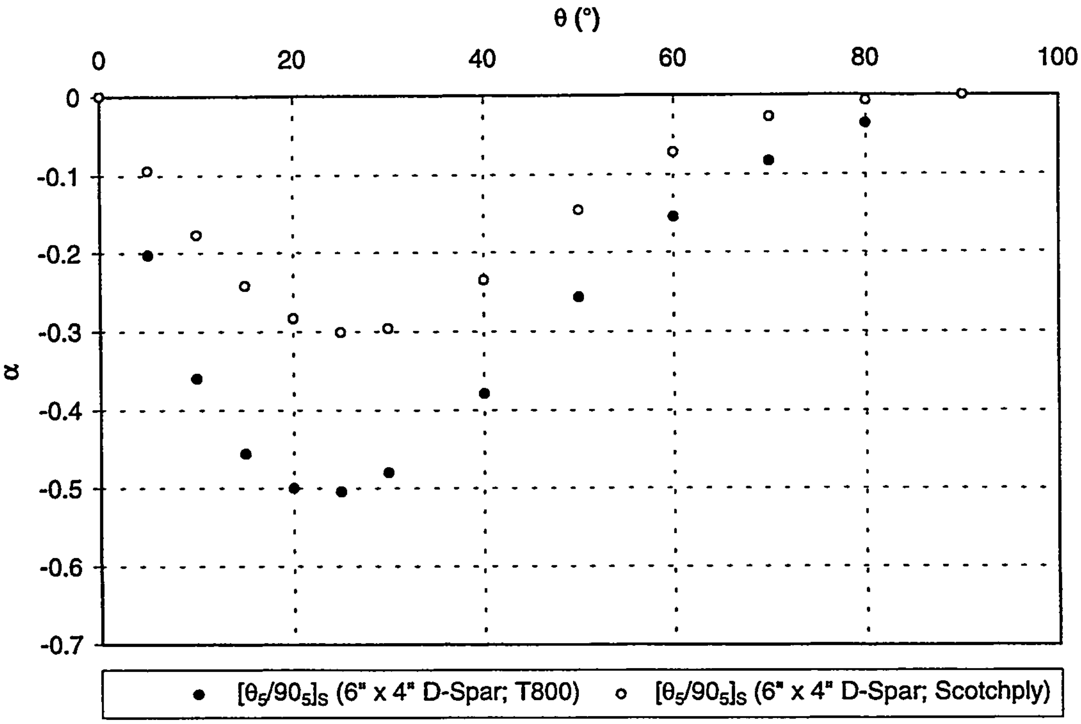

Figure 3.4c The Effects of Materials on α Interaction Parameter for $[\theta_5/90_5]_S$ lay-up

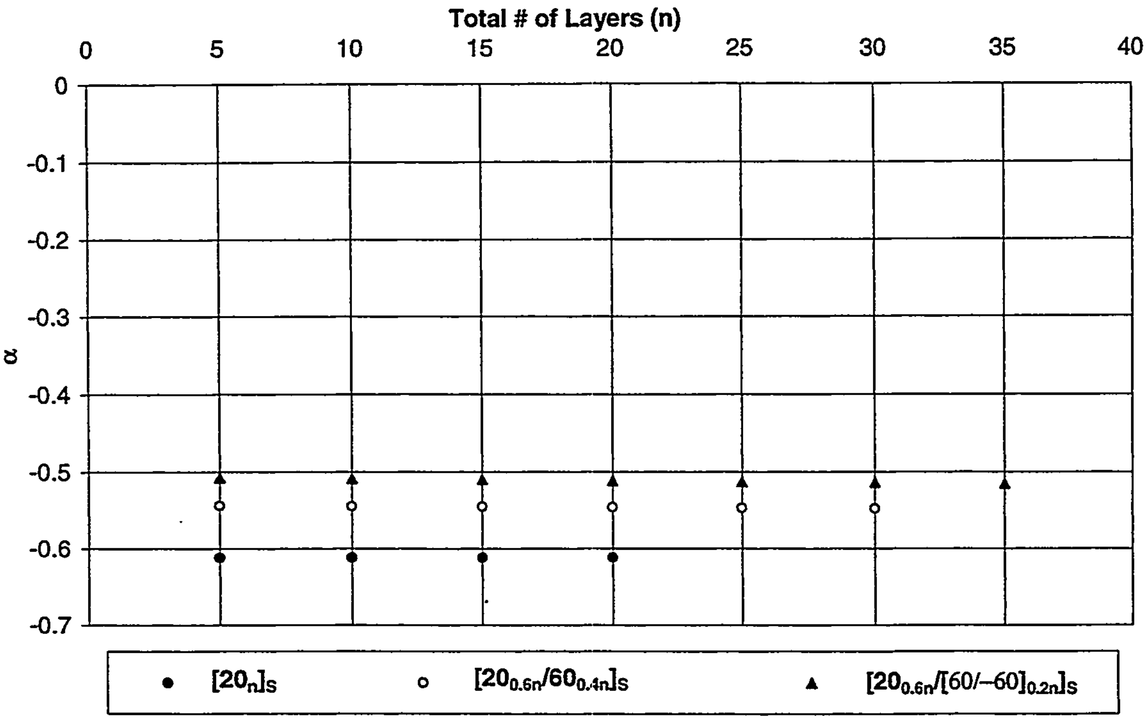

Figure 3.5a The Effects of Ply Thickness for a given distribution for 6" x 4" D-spar

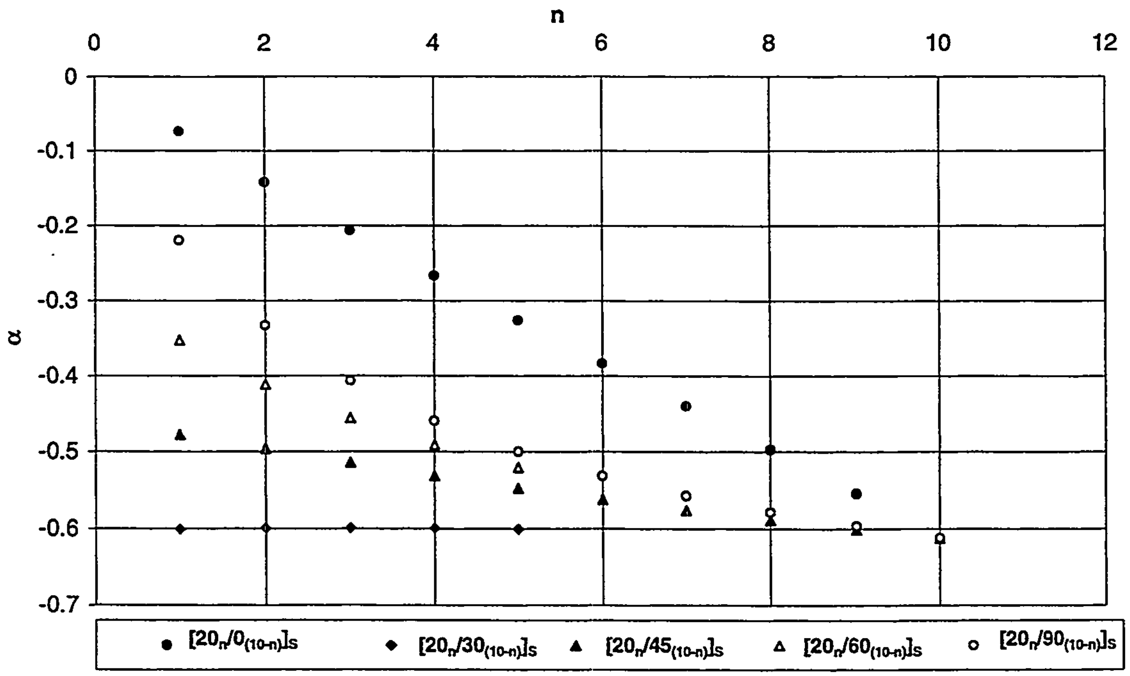

Figure 3.5b The Effects of Ply Thickness & Distribution for 6" x 4" D-spar

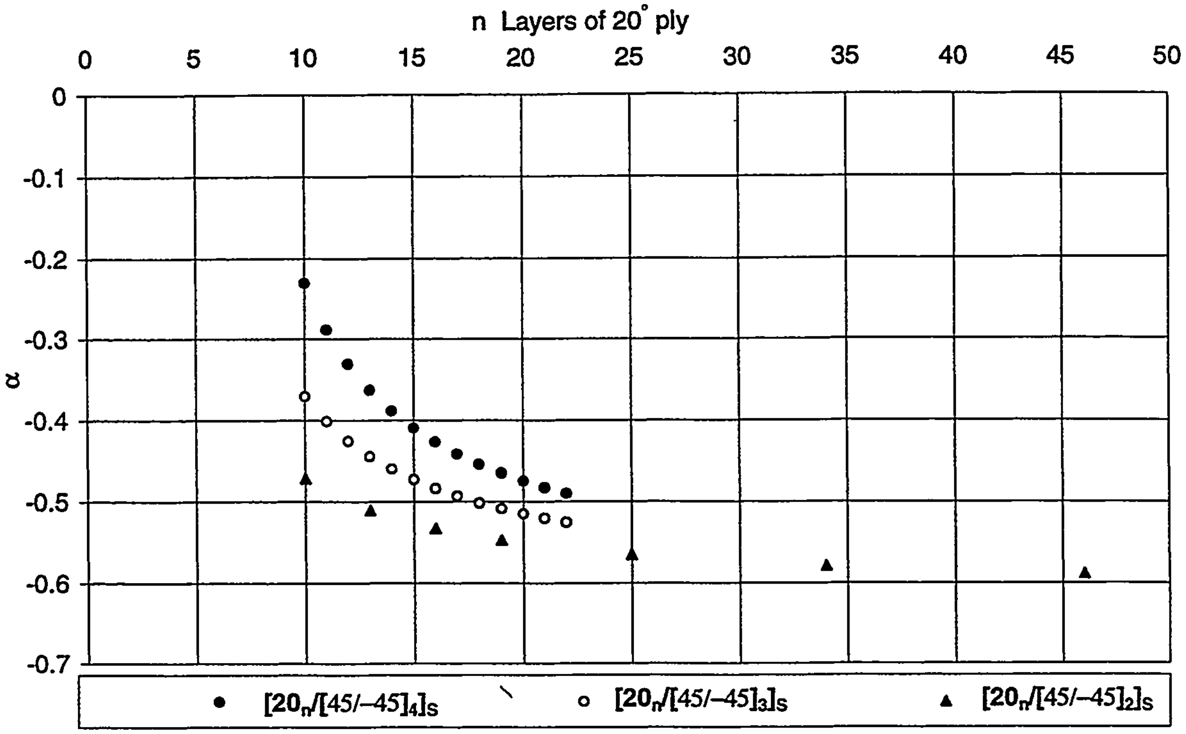

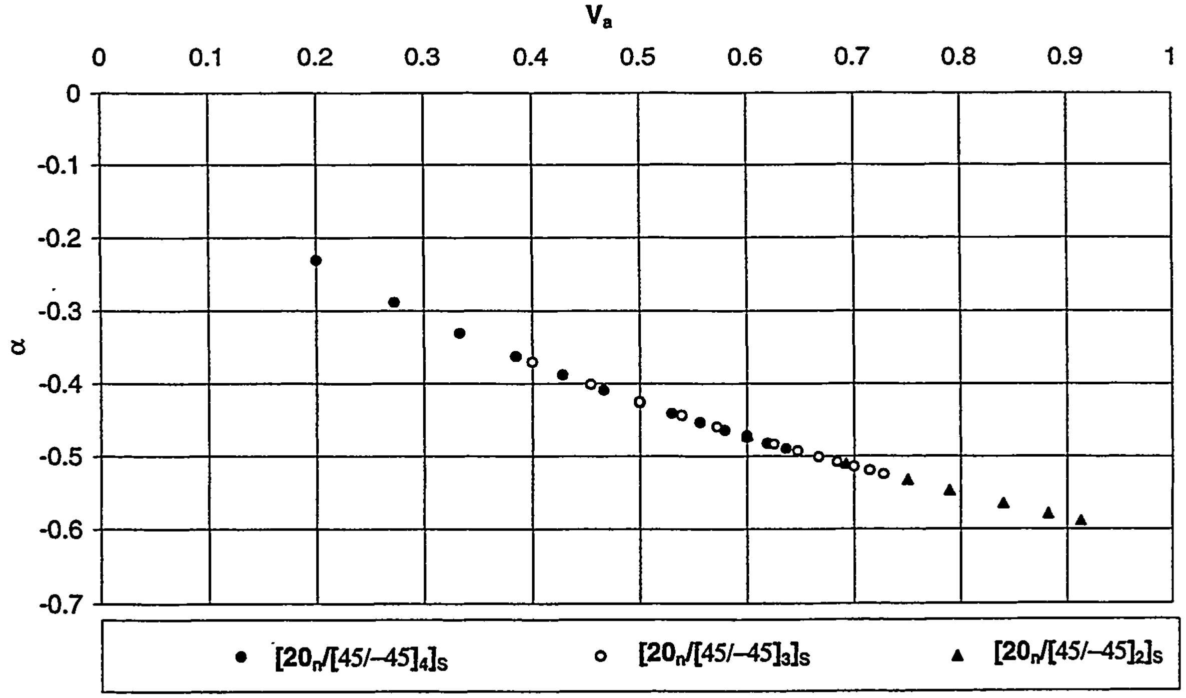

Figure 3.6 The Effect of Anisotropic Volumetric Ratio on α for 6" x 4" D-Spar

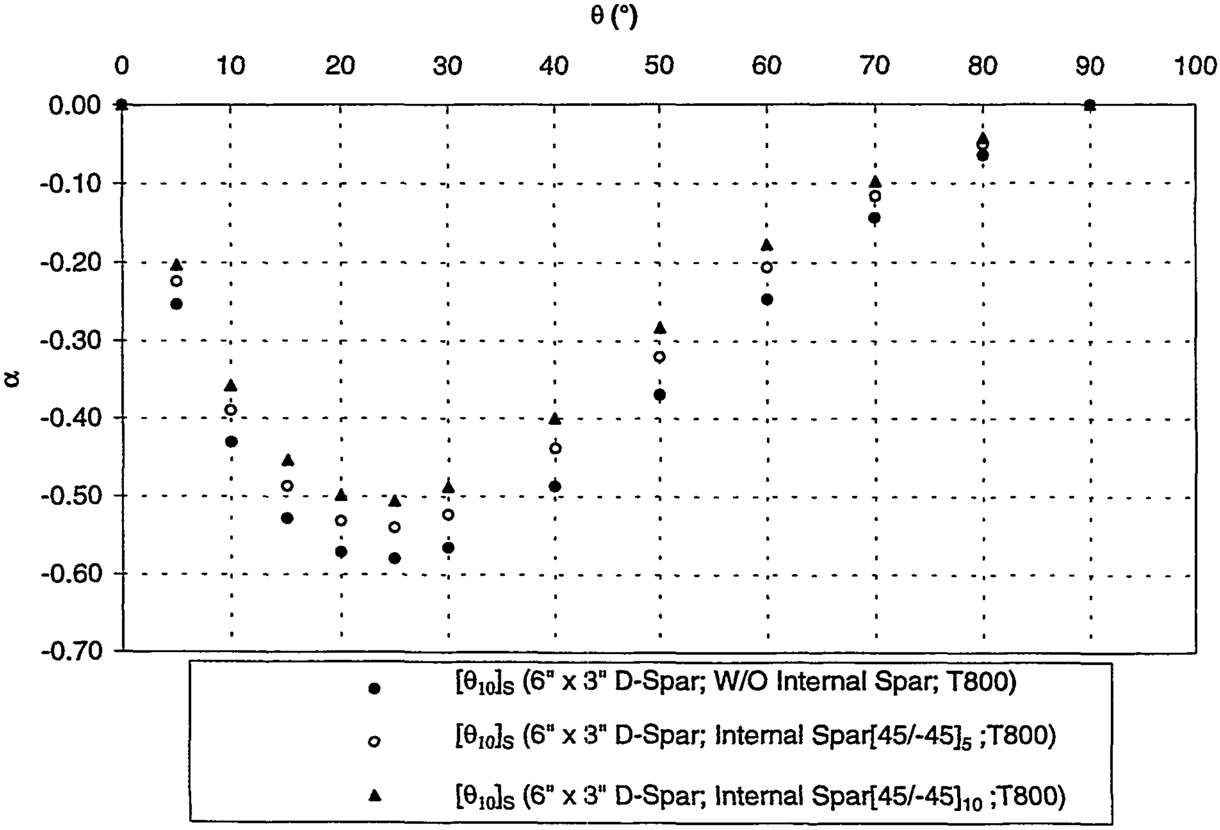

Figure 3.8 The Effect of Internal Spar Thickness (D-spar lay-up: $[\theta_{10}]_S$)

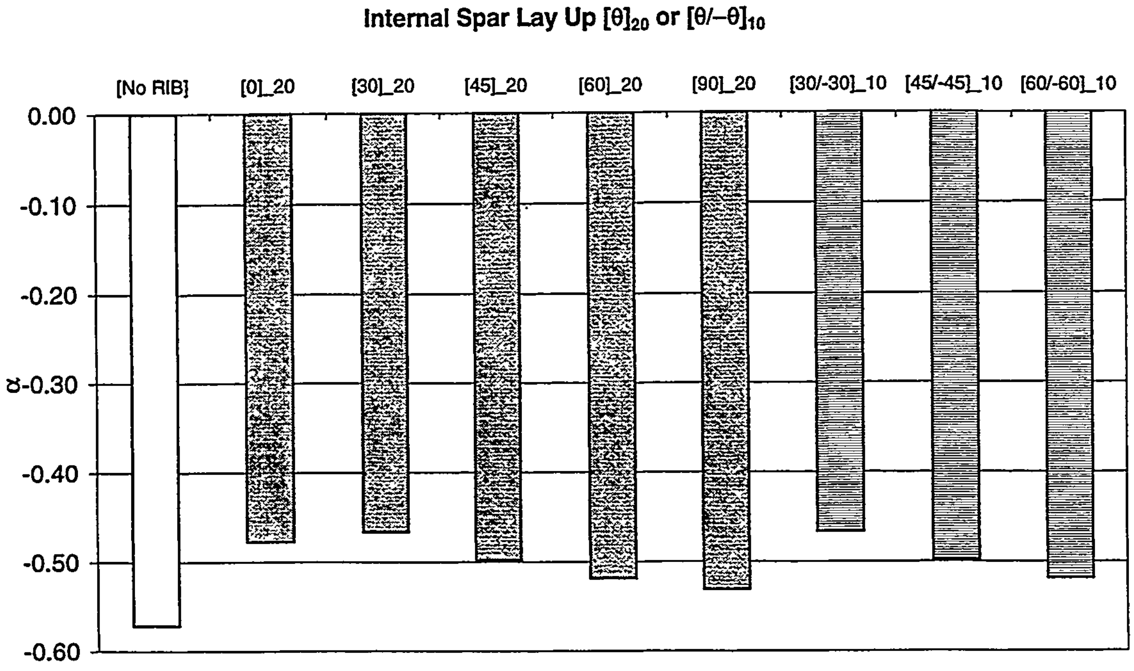

Figure 3.9a The Effect of Internal Spar Ply Orientation (D-spar lay-up: $[20_{10}]_S$)

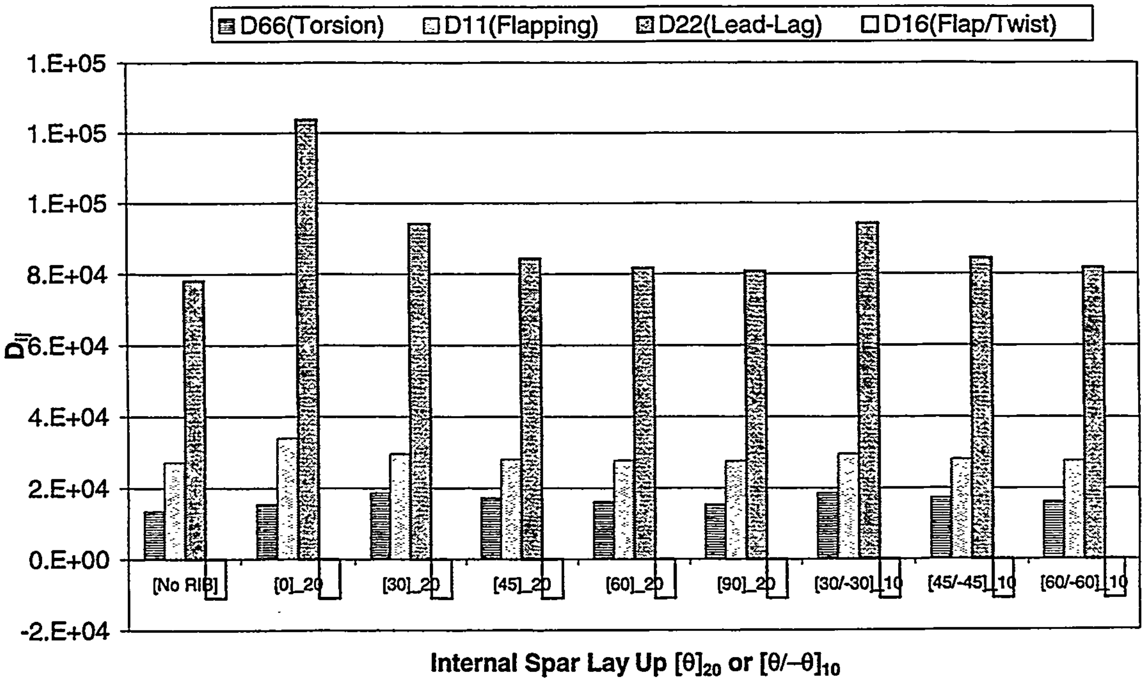

Figure 3.9b The Effect of Internal Spar Ply Orientation (D-spar lay-up: $[20_{10}]_S$)

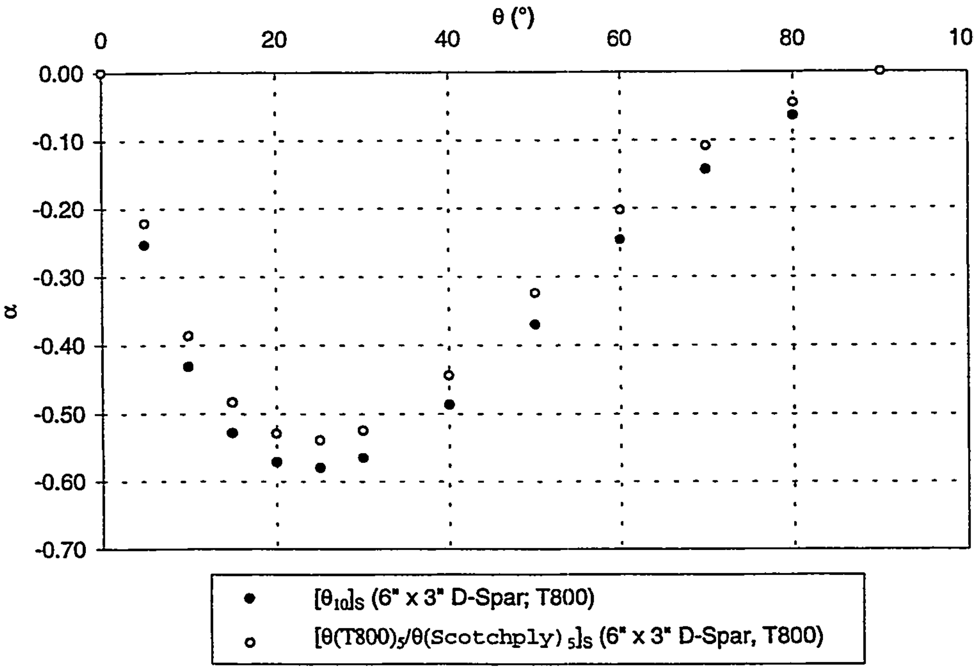

Figure 3.10a The Effect of Hybrid Materials on α Interaction Parameter for $[\theta_{10}]_S$ lay-up

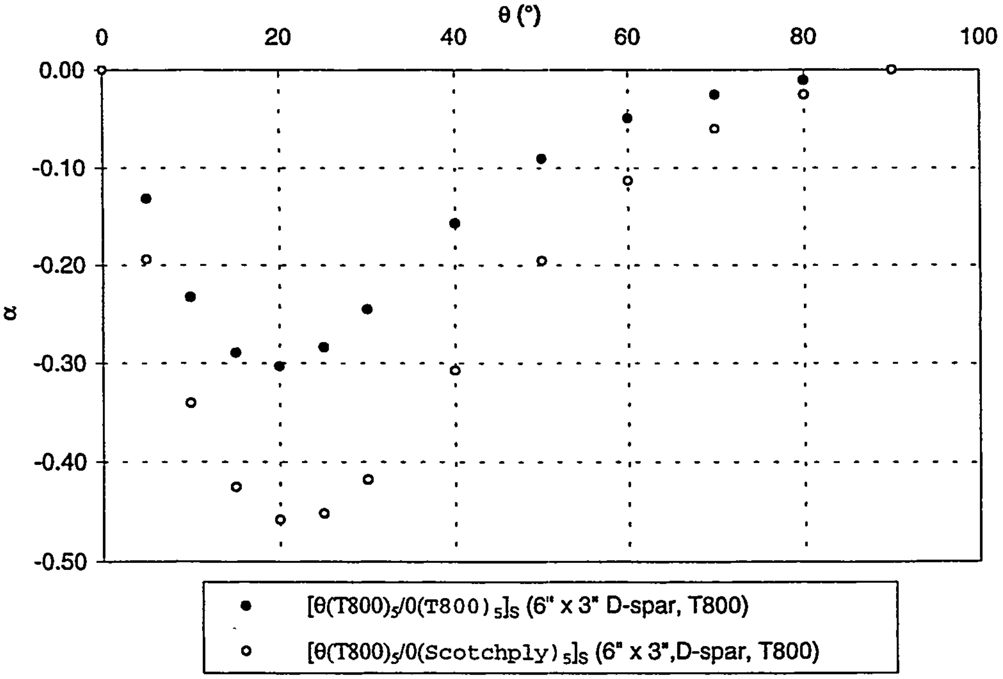

Figure 3.10b The Effect of Hybrid Materials on α Interaction Parameter for $[\theta_5/0_5]_S$ lay-up

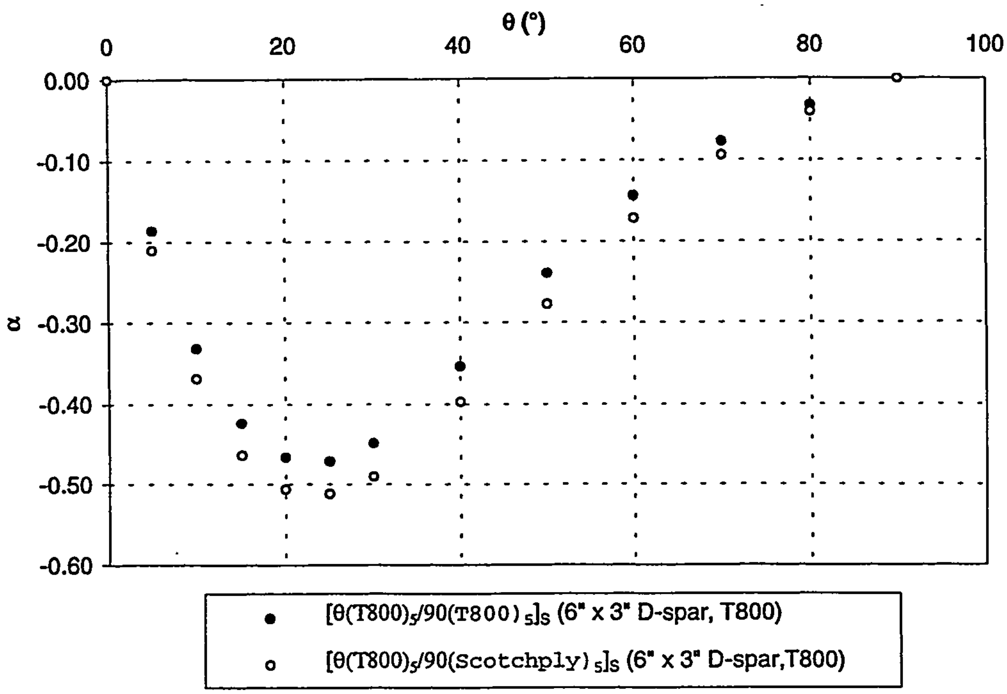

Figure 3.10c The Effect of Hybrid Materials on α Interaction Parameter for $[\theta_5/90_5]_S$ lay-up

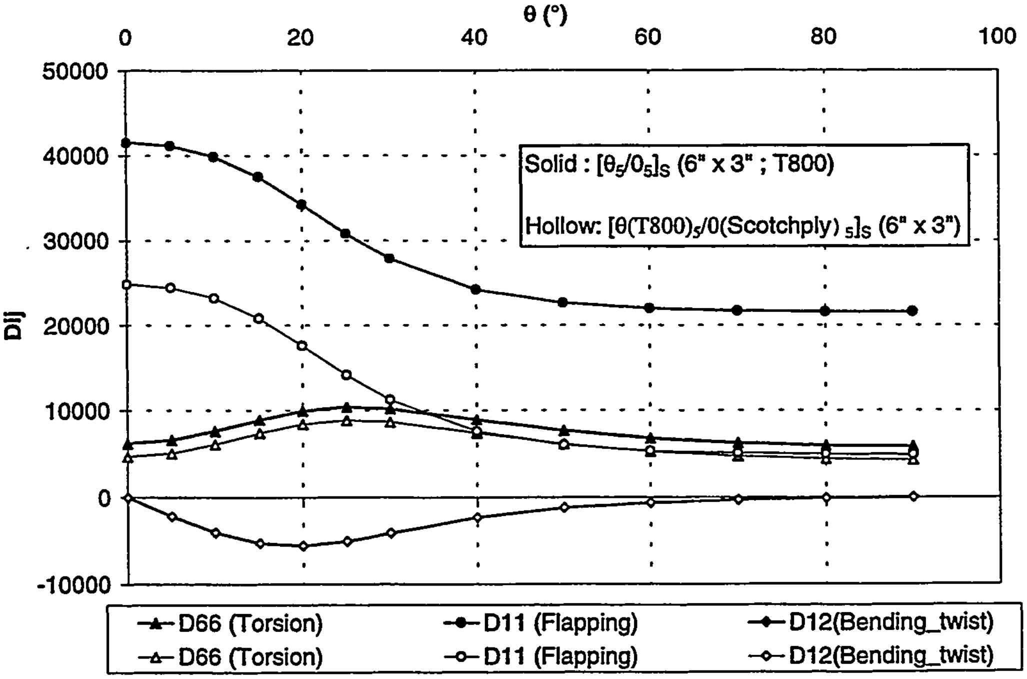

Figure 3.11 The Effect of Hybrid Materials on D_{ij}

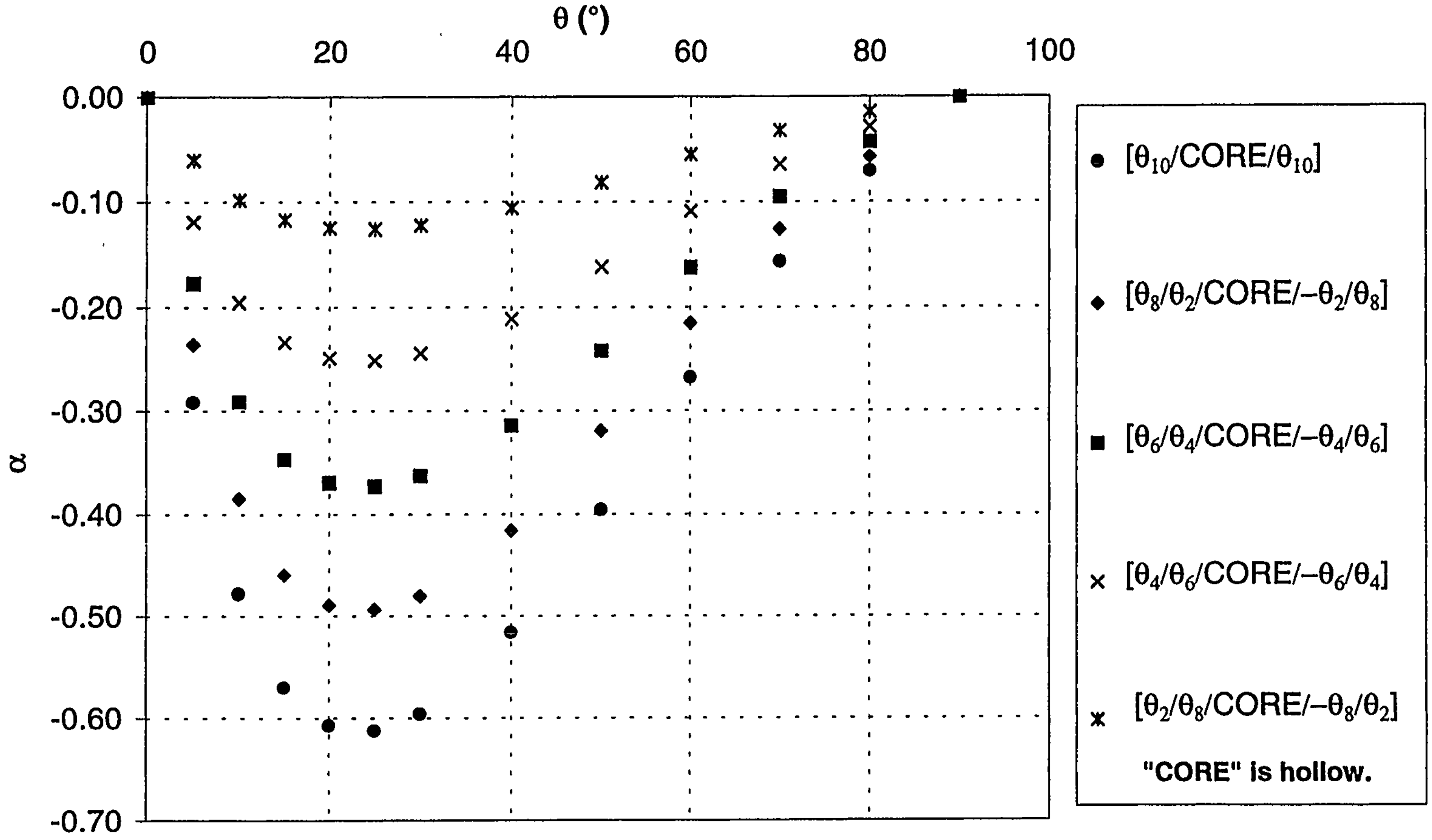

Figure 3.12 The Effect of Antisymmetry on α Interaction Parameter

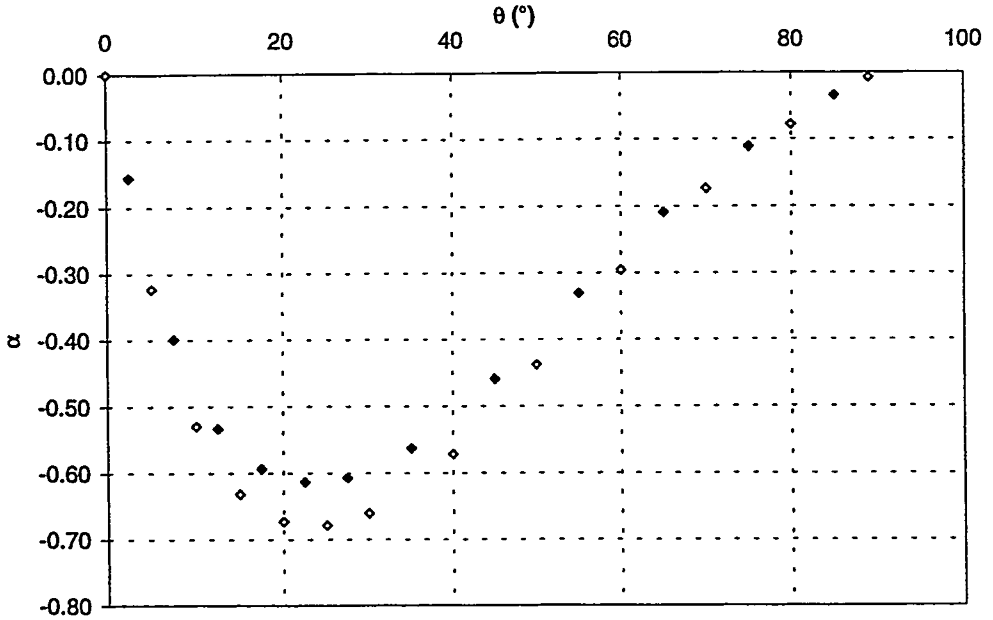

Figure 3.13a The Effect of Torsion-Related Out-of-Plane Warping on α

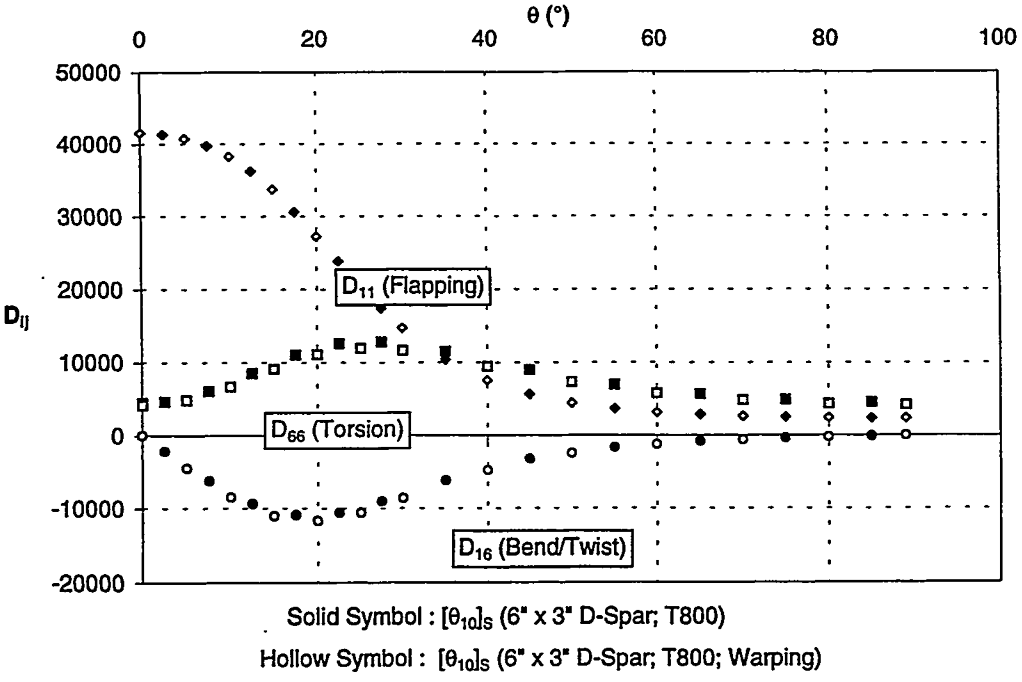

Figure 3.13b The Effect of Torsion-Related Out-of-Plane Warping on Stiffness Distribution

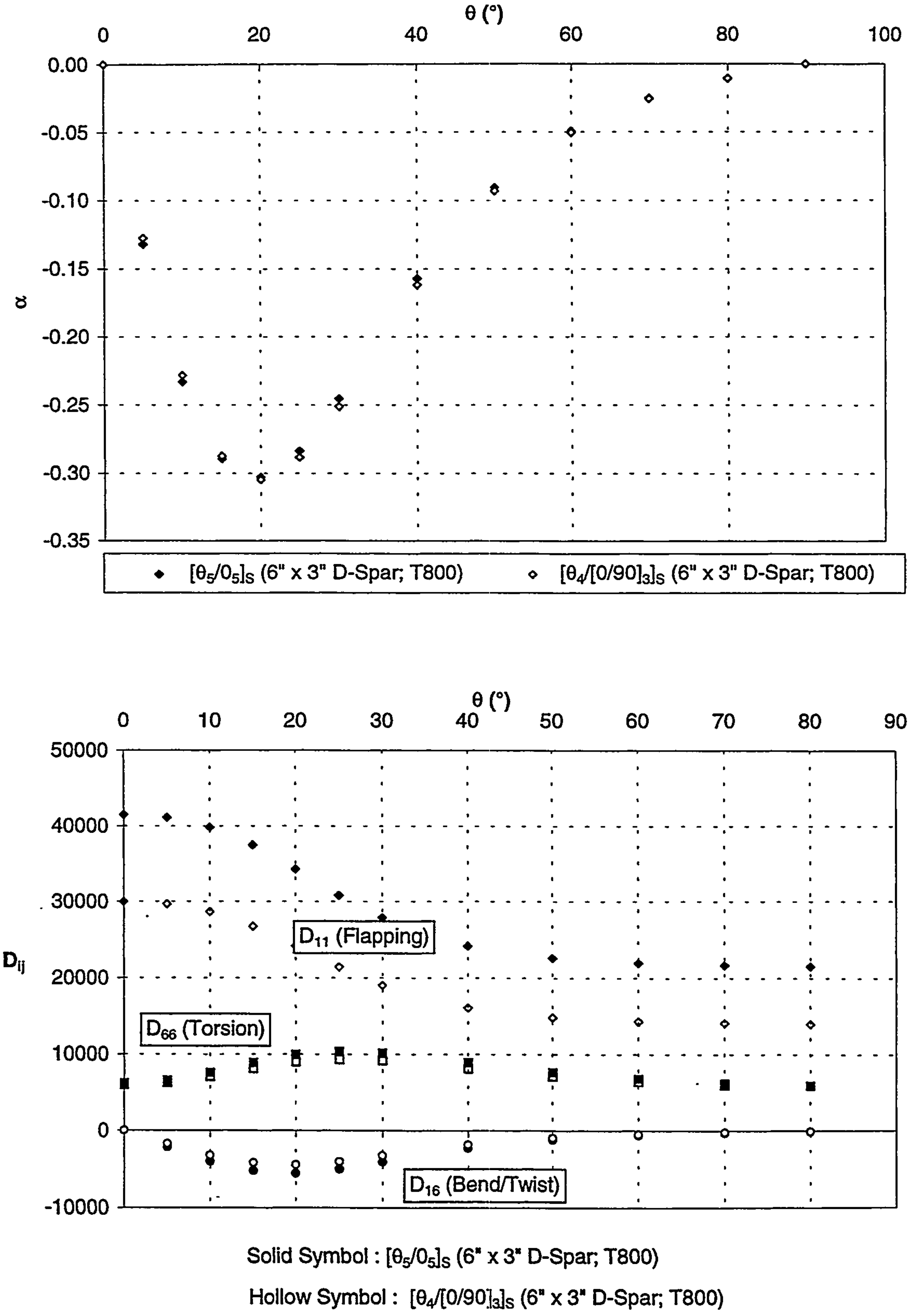

Figure 3.14 The Configuration that Exhibits Close α values but Different "EI & "GJ"

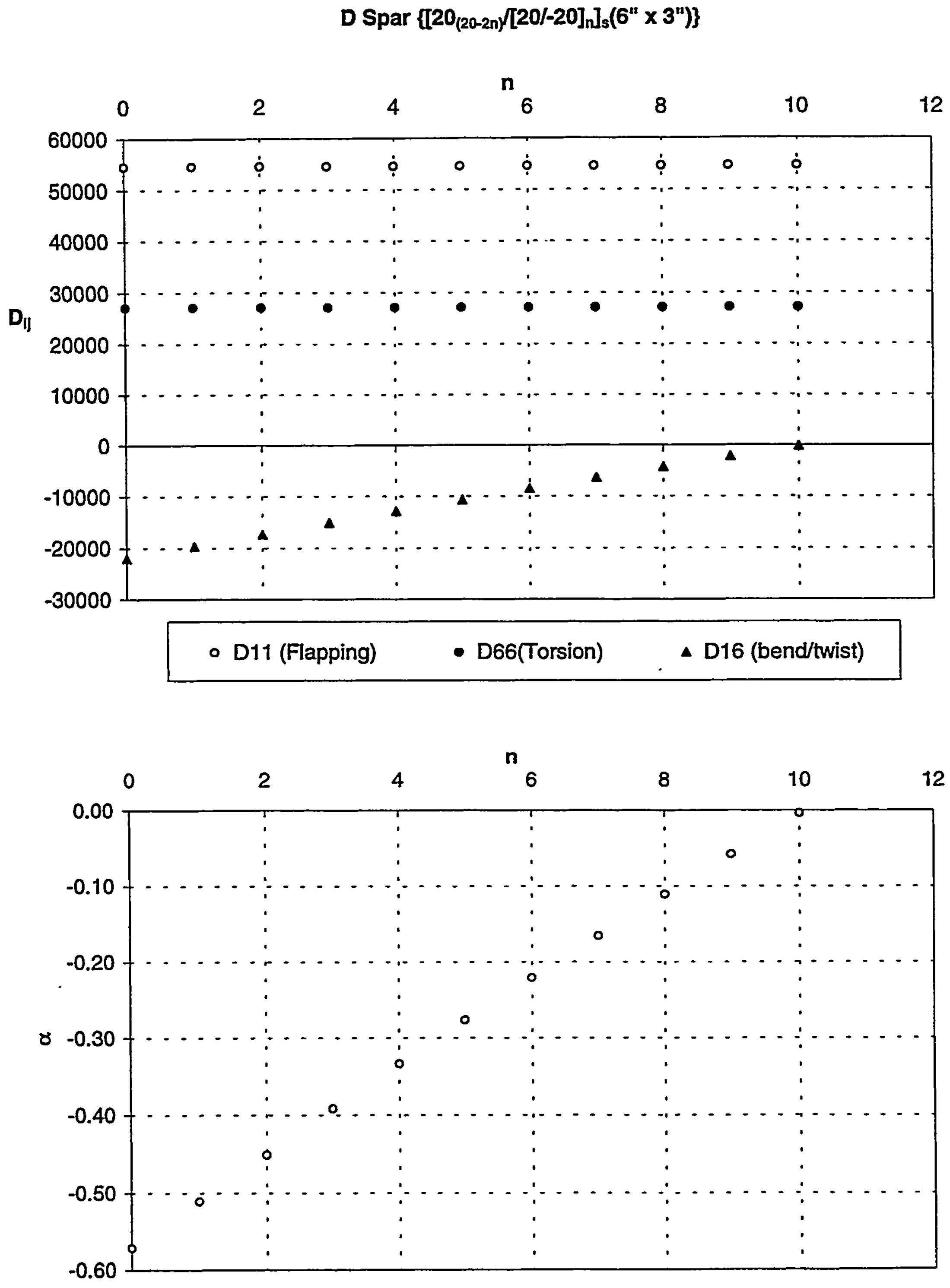

Figure 3.15 The Configuration that Exhibits the Same "EI" & "GJ" but Different α Values

Chapter 4

D-Spar Design

In the previous chapter, we looked at various parameters that affect the range of bend-twist coupling parameter and the critical parameters are,

a. Ply orientation: To have higher bend-twist coupling, the ply orientation should be between 15° and 30°.

b. Material: As the α interaction parameter depends implicitly on the normal and shear coupling coefficients (ν_{16} and ν_{61}), we should use the ply that has higher values of ν_{16} and ν_{61}. The graphite/epoxy gives higher α value than that of the glass/epoxy.

c. Volume fraction of the anisotropic layers: Any non-anisotropic layer will definitely decrease the α's value resulting in reduction in bend-twist coupling. The volume ratio of the anisotropic layers and non-anisotropic layers helps to control the desired degree of coupling.

4.1 D-Spar Design Specification

The D-spar's length is 72 inches and the cross-section dimension is shown in Figure 3.2. The D-spar that has constant cross-section properties should have both the bending and torsion stiffness close to the following values,

a. EI (flapwise) : 4.027×10^7 lb-in^2

b. GJ : 1.795×10^7 lb-in^2.

The EI and GJ are extracted from the data of a typical wind turbine blade (the Combined Experiment Blade, CEB). In addition to that, the D-spar must exhibit a certain degree of bend-twist coupling without compromising the structural integrity. The guideline is to design a D-spar that has tip rotation of at least 1 degree without exceeding a certain factor of safety for the static test (factor of safety of 2 is used in the design).

4.2 Theoretical Approach In Estimating Maximum Tip Rotation

We want to know the maximum tip rotation that is acheivable for a cantilevered, symmetric, composite D-spar. The equations for the bending-twist coupling are given in matrix form below:

$$\begin{bmatrix} EI & -g \\ -g & GJ \end{bmatrix} \begin{bmatrix} \frac{\partial \theta}{\partial x} \\ \frac{\partial \varphi}{\partial x} \end{bmatrix} = \begin{bmatrix} M_b \\ M_t \end{bmatrix} \quad \text{(Eq.6 of Lobitz and Veers}^9\text{)}$$

The bending slope, θ, and bending-induced twist, φ in a uniform, constant cross-section, cantilevered, symmeteric D-spar subjected to a tip load P are obtained from the above equations as:

$$\theta = \frac{P}{2\,(EI - g^2 / GJ)}(2 * l * x - x^2)$$

$$\varphi = \frac{P * g}{2\,(EI * GJ - g^2)}(2 * l * x - x^2) \tag{4.1}$$

where l is the length of the D-spar.

At the tip ($x = l$), the tip rotation is equal to $\frac{g * l^2 * P}{2\,(EI * GJ - g^2)}$. If we substitute the α interaction parameter, we get the $\varphi_{tip} = \frac{\alpha * l^2 * P}{2\sqrt{EI * GJ}\,(1 - \alpha^2)}$. The φ_{tip} depends on the length of the D-spar, the load, P, the α interaction parameter and the square root of the product of the EI and GJ. If the load and the length of the D-spar are fixed, to maximize the tip rotation we need to maximize the $\frac{\alpha}{\sqrt{EI * GJ}\,(1 - \alpha^2)}$ term. In fact, we can further split the term into the product of $\frac{1}{\sqrt{EI * GJ}}$ and $\frac{\alpha}{(1 - \alpha^2)}$. And we know that the value of $\frac{\alpha}{(1 - \alpha^2)}$ increases as the α increases, and the maximum value of the $\frac{\alpha}{(1 - \alpha^2)}$ goes to infinity as α approaches one. Therefore, to maximise the tip rotation, we need to minimise the product of the EI*GJ and maximise the α value.

The lower bound of the EI and GJ should be the same as the design values, which are equal to 4.027 x 10^7 lb-in^2 and 1.795 x 10^7 lb-in^2 respectively. As such, the theoretical estimation of the maximum tip rotation depends entirely on the α interaction parameter.

In the previous chapter, we found that the maximum α interaction parameter occurs at the ply orientation between 15°and 30°. The α interaction parameter also depends on the types of ply materials with which we fabricate the D-spar. The α_{max} is equal to 0.58 and 0.42 for all-graphite (T800/3900) and all-glass (ScotchPly) D-spar respectively. The upper bound of the tip rotation (φ_{tip}) of the built-in D-spars that have the length of 72 inches and have the same stiffness as the specification is obtained as:

a. all graphite case : -0.00483 °/lb

b. all glass case : -0.00282 °/lb

Figure 4.1 shows the variation of the tip rotation against the α interaction parameter for the desired D-spar. The D-spar has the specified structural properties, and the bend-induced tip rotation is based on the assumption that we can meet the stiffness design criteria.

4.3 Numerical Estimation of Tip Rotation

In this section, we want to assess whether we can design a D-spar that meets the stiffness requirements as well as fulfills the maximum tip rotation requirement. We look into two typical cases: all-graphite D-spar and all-glass D-spar. The material ply properties for a) T800/3900-2 (Graphite/Epoxy) and b) Scotchply (Glass/Epoxy) are given in Table 3.1.

The estimated results of the tip rotation, the EI and GJ properties for the all-graphite D-spar and the all-glass D-spar cases are tabulated in Table 4.1 and 4.2 respectively. The results indicate that EI decreases and GJ increases as the ply orientation angle increases (between 15° and 30°). The results also indicate that it is not possible to achieve the specified EI and GJ with a single ply orientation lay up. The best laminate lay up that is close to the design criteria is the all-graphite case with 20° ply orientation.

It is possible to fulfill the EI and GJ requirements by replacing some of the unidirectional plies with a combination of angle plies, 0° and 90° ply orientation. A typical example is shown in Table 4.2. The lay up of $[25_{26}/0_{33}]_S$ for all-glass D-spar provides a single-digit percentage error in EI and GJ. However, the tip rotation is reduced to half (from –0.002787°/lb to –0.001245°/lb) as the α interaction parameter has been reduced from 0.43 to 0.19. The reduction of the α interaction parameter is caused by the inclusion of the orthotropic layers.

Therefore, in designing the D-spar, we need to relax the EI and GJ requirements and maximize the tip rotation by maximizing value of the α interaction parameter. The next consideration for the D-spar design is structural integrity.

4.4 D-Spar Structural Integrity

One of the factors to consider in the structural analysis is the type of loading exerted on the structure. In the current design, we focus our analysis only on cantilevered loading.

4.4.1 D-spar Modelling Using 3D-Beam Program

We need to mention some features about the 3D Beam program. The failure criteria used in the 3D Beam software are based on the Tsai-Wu[12] quadratic failure criteria. If the strength/stress index (R) is greater than one, then the structure is safe. R equals 1 when the allowable or ultimate stress is reached.

The 3D Beam software outputs the distribution of the R along the cross-section at various longitudinal locations. Since we are analysing a constant cross-section D-spar, which has constant structural properties (EI, GJ), the failure should occur at the root section of a built-in structure. Therefore, only the output at the root (Element Group Number 1 as in 3D Beam notation) of the D-spar is presented.

The pin-point location of the failure at any cross-section is identified by the "brick" where the R index is less than or equal to one (or the lowest R value on the cross-section that is used to predict the failure load). The D-spar has been modelled with 26 Bricks (Brick No. 1 to 26) for every cross-section at various longitudinal stations. And 4 additional Bricks (Brick No. 27 to 30) are used to model the butt joint at the mid-plane section. The brick numbers of the D-spar are shown in Figure 4.2.

4.4.2 D-Spar Structural Analysis

Butt Joint

The selection of laminate schedule at the butt-joint layers depends on the strength of the joint and the effect of these additional layers on the EI, GJ and α. We look into four common sets of ply lay-up; i.e. [0/90], [+/-30], [+/-45], [+/-60]. The effects of the butt joint reinforcement on the EI, GJ and α are shown in Tables 4.3 and 4.4 for the all-graphite and the all-glass D-spars respectively. The results indicate the additional layers at the joint do not significantly change D-spar structural properties.

The [0°/90°] ply lay-up for these additional layers at the joint is the best selection because of the highest factor of safety (FS is similar to the R index). Therefore [0°/90°] ply lay-up is used for the ply layers at the joint.

Body

Three different D-spars have been studied, and the results are summarized in subsequent paragraphs.

Tables 4.5a & 4.5b show the summarized results for the all-graphite D-spar. The results indicate that the $[20°_{16}]$ off-axis unidirectional ply gives the highest tip rotation. For a tip load of 420 lb., the tip rotation is about 1.9° at the factor of safety (or the R index) of 2. In addition, the EI and GJ errors are within 10% and 20% respectively.

Tables 4.6a & 4.6b show the summarized results for the all-glass D-spar. The results indicate the all $[25°_{60}]$ off axis unidirectional ply gives the highest tip rotation per unit pound load. The EI and GJ errors are –22.9% and 41.7% respectively, but the error of $1/\sqrt{(EI*GJ)}$ is less than 5%. At safety factor of 2, the tip rotation and tip load of the $[25°_{60}]$ configuration are at 2.2° and 725 lb. respectively

Tables 4.7a & 4.7b show the summarized results for the hybrid D-spar. The results indicate the best laminate lay up for the hybrid D-spar is the combination of glass and graphite at the [20°] off-axis unidirectional ply because the α interaction parameter is between 0.5-0.56, and the error of the EI is less than 10%. The ratio of the mixture should be one layer of glass material with two layers of graphite material.

4.5 D-Spar Configuration for Demonstration

The above analysis implies that the best laminate lay up to achieve the maximum tip rotation, as well as not to compromise the structural integrity, is 20°-25° off-axis unidirectional lay up. This lay up has one major disadvantage; the failure is catastrophic failure. Since the same D-spars will undergo both the static test and modal test, it is better to design the D-spars to fail at the first outer layer under static load. The D-spars are then designed for first-ply failure.

The following configurations are studied,

(i) Case a: the all-graphite D-spar ($[\theta_1/20_{15}/\theta_1]_S$)

(ii) Case b: the all-glass D-spar ($[\theta_1/25_{60}/\theta_1]_S$)

(iii) Case c: the hybrid D-spar ($[\theta_1(c)/20_6(c)/20_6(gl)/20_6(c)/\theta_1(c)]_S$; 'c' denotes graphite and 'gl' denotes glass)

Tables 4.8a, 4.8b and 4.8c show the summarized results for cases (a), (b) and (c) respectively. The results indicate the θ angle of the first-ply, which will fail first, should be between,

(i) 60° and 70° [case (a)],

(ii) –50° and –60° [case (b)], and

(iii) 70° and 80° [case (c)].

4.6 Summary

To achieve the maximum tip rotation per unit pound load, the ply orientation of the laminate should be at 20° for the all-graphite D-spar and at 25° for the all-glass D-spar. The hybrid D-spar will have higher tip rotation if the mixture is one layer of the glass material to two layers of the graphite material. It is not possible to have the bending and torsion stiffness of the D-spar close to the design values by just using one off-axis unidirectional lay up. The inclusion of non-anisotropic layers helps to meet the stiffness criteria but fails to fulfill the requirement of the maximum tip rotation. The analysis indicates that the D-spar will be able to achieve at least 1° tip rotation without structure failure under static tip loading.

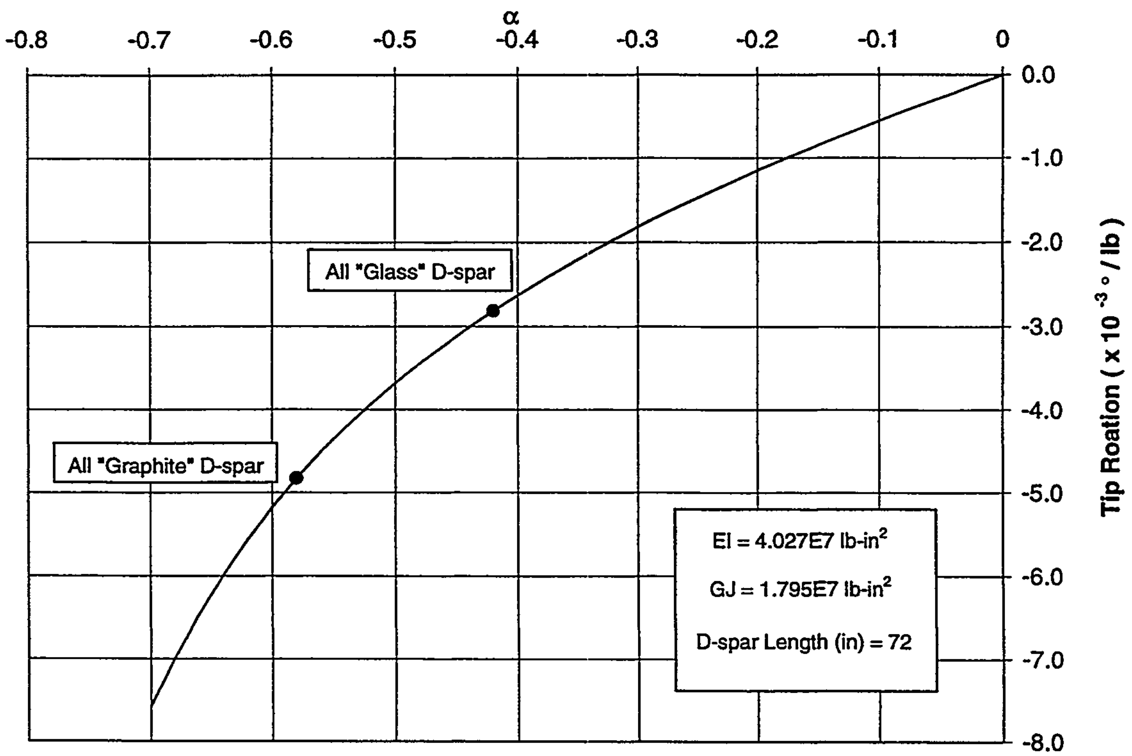

Figure 4.1 The Tip Rotation Variation of a D-spar Exhibiting Specified Structural Properties but Different α

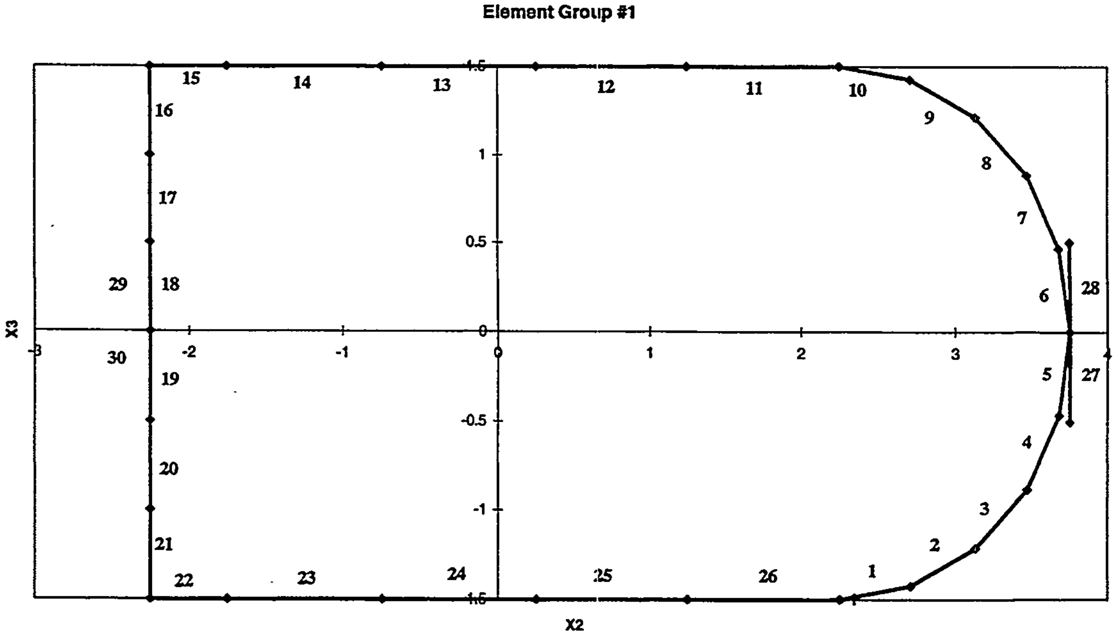

Figure 4.2 The Modeling of D-spar Cross-Section with 30 "Brick" Elements

Lay Up	α	Tip Rotation (°/lb.)	EI (x 10^7 lb-in^2)		GJ (x 10^7 lb-in^2)		√(EI*GJ) (x 10^7 lb-in^2)	
			Estimate	Error	Estimate	Error	Estimate	Error
$[15_{14}]$s	-0.54	-0.004483	4.7306	17.5%	1.5572	-13.2%	2.7141	0.9%
$[20_{14}]$s	-0.58	-0.005178	3.84	-4.6%	1.8562	3.4%	2.6698	-0.7%
$[25_{14}]$s	-0.58	-0.005862	2.8925	-28.2%	1.9833	10.5%	2.3951	-10.9%
$[30_{14}]$s	-0.57	-0.006561	2.0799	-48.4%	1.9385	8.0%	2.0079	-25.3%

Table 4.1 The Results of Tip Rotation, EI and GJ for all-Graphite D-spar

Lay Up	α	Tip Rotation (°/lb.)	EI (x 10^7 lb-in^2)		GJ (x 10^7 lb-in^2)		$\sqrt{(EI*GJ)}$ (x 10^7 lb-in^2)	
			Estimate	Error	Estimate	Error	Estimate	Error
$[15_{64}]s$	-0.35	-0.002183	4.2937	6.6%	2.1161	17.9%	3.0143	12.1%
$[20_{64}]s$	-0.41	-0.002553	3.8392	-4.7%	2.4335	35.6%	3.0566	13.7%
$[25_{64}]s$	-0.43	-0.002787	3.3135	-17.7%	2.7084	50.9%	2.9957	11.4%
$[25_{26}/0_{33}]s$	-0.19	-0.001245	3.8742	-3.8%	1.9125	6.5%	2.7220	1.2%
$[30_{64}]s$	-0.43	-0.002905	2.7781	-31.0%	2.8806	60.5%	2.8289	5.2%

Table 4.2 The Results of Tip Rotation, EI and GJ for all-Glass D-spar

Tip Load = -100 LB

	Tip Defl.(")	Tip Rot.(°)	α	EI_error	GJ_error	1/sqrt(EI*GJ) Error	Critical Brick	FS
W/O Butt Joint Reinforcement	**-0.3356**	**0.2868**	**-0.42**	**18.16%**	**30.64%**	**-19.51%**	**21**	**9.15**
Butt Joint Reinforcement								
$(0/90)_8$	**-0.3279**	**0.2625**	**-0.40**	**18.69%**	**40.58%**	**-22.58%**	**21**	**9.82**
$(30/-30)_8$	**-0.3199**	**0.2299**	**-0.38**	**18.51%**	**58.25%**	**-26.98%**	**21**	**10.88**
$(45/-45)_8$	**-0.3241**	**0.2440**	**-0.39**	**18.30%**	**50.35%**	**-25.02%**	**21**	**10.39**
$(60/-60)_8$	**-0.3273**	**0.2557**	**-0.40**	**18.24%**	**44.35%**	**-23.46%**	**21**	**10.02**

Safety Factor for the Bricks (27, 28, 29 and 30) at the butt joint

Brick No	27	28	29	30
$(0/90)_8$	**35.04**	**30.44**	**25.45**	**28.56**
$(30/-30)_8$	**13.58**	**17.79**	**14.05**	**11.28**
$(45/-45)_8$	**15.57**	**16.83**	**13.60**	**12.76**
$(60/-60)_8$	**21.09**	**19.46**	**16.01**	**17.09**

Table 4.3 The Effect of the Ply Orientation of the Butt Joints for the all-graphite D-spar ($[(45/-45)_1/25_7/0_4/25_7/(-45/45)_1]_S$).

Tip Load = -100 LB

	Tip Defl.(")	Tip Rot.(°)	α	EI_error	GJ_error	1/sqrt(EI*GJ) Error	Critical Brick	FS
W/O Butt Joint Reinforcement	**-0.3028**	**0.1038**	**-0.19**	**8.16%**	**30.18%**	**-15.73%**	**16**	**18.03**
Butt Joint Reinforcement								
$(0/90)_8$	**-0.3018**	**0.1000**	**-0.19**	**8.27%**	**35.23%**	**-17.36%**	**16**	**18.51**
$(30/-30)_8$	**-0.3012**	**0.0969**	**-0.18**	**8.26%**	**39.74%**	**-18.70%**	**16**	**18.90**
$(45/-45)_8$	**-0.3014**	**0.0974**	**-0.18**	**8.22%**	**39.12%**	**-18.50%**	**16**	**18.84**
$(60/-60)_8$	**-0.3017**	**0.0988**	**-0.18**	**8.20%**	**37.11%**	**-17.90%**	**16**	**18.66**

Safety Factor for the Bricks (27, 28, 29 and 30) at the butt joint

Brick No.	27	28	29	30
$(0/90)_8$	**167.19**	**78.04**	**58.64**	**86.43**
$(30/-30)_8$	**58.04**	**71.46**	**32.72**	**29.50**
$(45/-45)_8$	**67.50**	**52.65**	**26.99**	**30.52**
$(60/-60)_8$	**116.69**	**51.19**	**29.65**	**45.18**

Table 4.4 The Effect of the Ply Orientation of the Butt Joints for the all-glass D-spar ($[(45/-45)_2/25_{15}/0_{34}/25_{15}/(-45/45)_2]_S$)

Tip Load = -100 LB

D_spar Lay Up	Tip Rot.(°)	α	Critical Brick	FS	Projected Tip Rot.(°) for FS=2	Projected Tip Load (lb) for FS=2
$[20_{16}]_S$	0.4615	-0.58	18	8.40	1.9380	420
$[(20/-70)_1/20_{13}/(-70/20)_1]_S$	0.4375	-0.56	18	8.83	1.9323	442
$[25_{20}]_S$	0.4286	-0.59	18	7.91	1.6959	396
$[15_{16}]_S$	0.4003	-0.54	18	11.37	2.2746	568
$[(20/-70)_1/20_{16}/(-70/20)_1]_S$	0.3792	-0.56	18	10.16	1.9260	508
$[25_8/0_2/25_8]_S$	0.3592	-0.51	18	9.21	1.6531	460
$[(45/-45)_1/20_{16}/(-45/45)_1]_S$	0.3414	-0.52	21	7.49	1.2783	374
$[15_{20}]_S$	0.3296	-0.55	18	13.73	2.2636	687
$[25_8/0_3/25_8]_S$	0.3090	-0.48	18	10.54	1.6292	527
$[(45/-45)_1/25_6/0_3/25_6/(-45/45)_1]_S$	0.2620	-0.40	21	8.84	1.1586	442
$[(45/-45)_1/25_6/0_3/25_7/(-45/45)_1]_S$	0.2570	-0.41	21	9.09	1.1687	455
$[(45/-45)_1/20_6/0_3/20_6/(-45/45)_1]_S$	0.2564	-0.42	21	9.33	1.1955	466
$[(45/-45)_1/25_7/0_3/25_7/(-45/45)_1]_S$	0.2526	-0.42	21	9.33	1.1781	466
$[(45/-45)_1/25_7/0_4/25_7/(-45/45)_1]_S$	0.2223	-0.40	21	10.44	1.1606	522

Table 4.5a The Summary Results of All-Graphite D-spar

Tip Load = -100 LB

D_spar Lay Up	EI_Error	GJ_Error	1/√(EI*GJ)_Error
$[20_{16}]_S$	8.9%	16.8%	-11.3%
$[(20/-70)_1/20_{13}/(-70/20)_1]_S$	3.4%	15.9%	-8.7%
$[25_{20}]_S$	2.4%	53.6%	-20.3%
$[15_{16}]_S$	34.2%	-2.3%	-12.7%
$[(20/-70)_1/20_{16}/(-70/20)_1]_S$	23.8%	36.0%	-22.9%
$[25_8/0_2/25_8]_S$	2.6%	29.9%	-13.4%
$[(45/-45)_1/20_{16}/(-45/45)_1]_S$	14.5%	36.8%	-20.1%
$[15_{20}]_S$	67.6%	19.7%	-29.4%
$[25_8/0_3/25_8]_S$	13.0%	32.4%	-18.2%
$[(45/-45)_1/25_6/0_3/25_6/(-45/45)_1]_S$	-1.8%	23.7%	-9.3%
$[(45/-45)_1/25_6/0_3/25_7/(-45/45)_1]_S$	3.3%	30.8%	-14.0%
$[(45/-45)_1/20_6/0_3/20_6/(-45/45)_1]_S$	18.3%	17.6%	-15.2%
$[(45/-45)_1/25_7/0_3/25_7/(-45/45)_1]_S$	8.4%	38.1%	-18.2%
$[(45/-45)_1/25_7/0_4/25_7/(-45/45)_1]_S$	18.7%	40.6%	-22.6%

Table 4.5b The Summary Results of All-Graphite D-spar

Tip Load = -100 LB

D_spar Lay Up	Tip Rot.(°)	α	Critical Brick	FS	Projected Tip Rot.(°) for FS=2	Projected Tip Load (lb) for FS=2
$[25_{60}]s$	0.2965	-0.43	18	14.5	2.1506	725
$[20_{60}]s$	0.2716	-0.41	18	18.5	2.5120	925
$[0_1/20_{64}/0_1]s$	0.2385	-0.40	18	20.9	2.4931	1045
$[20_{17}/15_{30}/20_{17}]s$	0.2332	-0.38	18	21.1	2.4548	1053
$[15_{60}]s$	0.2322	-0.35	18	25.4	2.9510	1271
$[(45/-45)_2/25_{15}/0_{34}/25_{15}/(-45/45)_2]s$	0.1000	-0.19	16	18.5	0.9266	927

Table 4.6a The Summary Results of All-Glass D-spar

Tip Load = -100 LB

D_spar Lay Up	Tip Rot.(°)	EI_Error	GJ_Error	1/√(EI*GJ)_Error
$[25_{60}]s$	0.2965	-22.9%	41.7%	-4.3%
$[20_{60}]s$	0.2716	-10.7%	27.4%	-6.3%
$[0_1/20_{64}/0_1]s$	0.2385	-0.8%	38.1%	-14.6%
$[20_{17}/15_{30}/20_{17}]s$	0.2332	2.1%	29.3%	-13.0%
$[15_{60}]s$	0.2322	-0.1%	10.8%	-5.0%
$[(45/-45)_2/25_{15}/0_{34}/25_{15}/(-45/45)_2]s$	0.1000	8.3%	35.2%	-17.4%

Table 4.6b The Summary Results of All-Glass D-spar

Tip Load = -100 LB

D_spar Lay Up	Tip Rot.(°)	α	Critical Brick	FS	Projected Tip Rot.(°) for FS=2	Projected Tip Load (lb)
$[20_7(c)/0_2(gl)/20_7(c)]_S$	0.4717	-0.56	18	8.2	1.9298	409
$[0_1(gl)/20_6(c)/20_6(gl)/20_6(c)/0_1(gl)]_S$	0.4507	-0.54	18	8.5	1.9256	427
$[20_8(c)/0_2(gl)/20_7(c)]_S$	0.4471	-0.56	18	8.6	1.9284	431
$[0_1(gl)/20_5(c)/20_{20}(gl)/20_5(c)/0_1(gl)]_S$	0.3598	-0.50	18	10.6	1.9076	530
$[(45/-45)_2(gl)/25_7(c)/0_{14}(gl)/25_7(c)/(-45/45)_2(gl)]_S$	0.2481	-0.42	16	10.7	1.3326	537

Table 4.7a The Summary Results of Hybrid D-spar

Tip Load = -100 LB

D_spar Lay Up	Tip Rot.(°)	EI_Error	GJ_Error	1/√(EI*GJ)_Error
$[20_7(c)/0_2(gl)/20_7(c)]_S$	0.4717	-0.8%	6.0%	-2.4%
$[0_1(gl)/20_6(c)/20_6(gl)/20_6(c)/0_1(gl)]_S$	0.4507	-5.5%	4.8%	0.5%
$[20_8(c)/0_2(gl)/20_7(c)]_S$	0.4471	6.0%	12.7%	-8.5%
$[0_1(gl)/20_5(c)/20_{20}(gl)/20_5(c)/0_1(gl)]_S$	0.3598	1.8%	20.0%	-9.6%
$[(45/-45)_2(gl)/25_7(c)/0_{14}(gl)/25_7(c)/(-45/45)_2(gl)]_S$	0.2481	3.4%	46.6%	-18.8%

Note : "gl" denotes glass and "c" denotes graphite

Table 4.7b The Summary Results of Hybrid D-spar

Tip Load = -100 LB

Θ°	Tip Defl.(")	Tip Rot.(°)	α	EI_error	GJ_error	1/√(EI*GJ)_error	Critical Brick	FS	Projected Tip Rot.(°) for FS=2	Projected Tip Load (lb)	Failure at Θ° Ply
-90	-0.4558	0.4487	-0.56	3.3%	15.1%	-8.3%	18	8.6	1.9399	432	No
-80	-0.4540	0.4451	-0.56	3.3%	15.3%	-8.4%	18	8.7	1.9394	436	No
-70	-0.4504	0.4375	-0.56	3.4%	15.9%	-8.7%	18	8.9	1.9386	443	No
-60	-0.4435	0.4239	-0.55	3.7%	17.0%	-9.2%	18	9.1	1.9371	457	No
-50	-0.4313	0.4005	-0.53	4.3%	18.9%	-10.2%	21	7.6	1.5127	378	Yes
-40	-0.4098	0.3630	-0.51	5.9%	21.5%	-11.8%	21	6.1	1.1022	304	Yes
-30	-0.3773	0.3133	-0.47	9.4%	24.1%	-14.2%	21	5.7	0.8858	283	Yes
-20	-0.3447	0.2776	-0.44	15.7%	23.4%	-16.3%	21	7.2	0.9939	358	Yes
-10	-0.3371	0.2951	-0.46	21.1%	18.2%	-16.4%	18	12.7	1.8716	634	No
0	-0.3575	0.3536	-0.52	22.8%	15.1%	-15.9%	18	10.7	1.8897	534	No
10	-0.3896	0.4097	-0.56	21.1%	18.2%	-16.4%	18	9.4	1.9173	468	No
20	-0.4214	0.4378	-0.58	15.7%	23.4%	-16.3%	18	8.8	1.9338	442	Yes
30	-0.4420	0.4428	-0.58	9.4%	24.1%	-14.2%	18	6.9	1.5190	343	Yes
40	-0.4507	0.4433	-0.57	5.9%	21.5%	-11.8%	18	6.9	1.5190	343	Yes
50	-0.4541	0.4451	-0.57	4.3%	18.9%	-10.2%	16	7.2	1.5959	359	Yes
60	-0.4557	0.4476	-0.56	3.7%	17.0%	-9.2%	16	7.4	1.6608	371	Yes
70	-0.4564	0.4494	-0.56	3.4%	15.9%	-8.7%	16	8.0	1.7872	398	Yes
80	-0.4565	0.4500	-0.56	3.3%	15.3%	-8.4%	18	8.6	1.9406	431	No
90	-0.4559	0.4490	-0.56	3.3%	15.1%	-8.3%	18	8.6	1.9400	432	No

Table 4.8a The Effect of the θ Ply on the D-spar Structural Performance and Failure; the lay up is $[\theta_1/20_{15}/\theta_1]_S$ (all graphite case)

Tip Load = -100 LB

Θ°	Tip Defl.(")	Tip Rot.(°)	α	EI_error	GJ_error	1/√(EI*GJ)_error	Critical Brick	FS	Projected Tip Rot.(°) for FS=2	Projected Tip Load (lb)	Failure at Θ° Ply
-90	-0.4942	0.2864	-0.42	-22.1%	44.3%	-5.7%	11	8.2	1.1683	408	Yes
-80	-0.4940	0.2860	-0.42	-22.1%	44.4%	-5.7%	11	9.0	1.2823	448	Yes
-70	-0.4933	0.2845	-0.42	-22.0%	44.7%	-5.9%	11	10.6	1.5126	532	Yes
-60	-0.4916	0.2816	-0.42	-22.0%	45.3%	-6.1%	11	13.9	1.9543	694	Yes
-50	-0.4883	0.2767	-0.41	-21.8%	46.0%	-6.4%	19	13.7	1.8902	683	Yes
-40	-0.4829	0.2700	-0.41	-21.4%	46.6%	-6.8%	21	11.5	1.5577	577	Yes
-30	-0.4759	0.2635	-0.40	-20.7%	46.6%	-7.2%	21	10.6	1.3947	529	Yes
-20	-0.4704	0.2617	-0.40	-19.9%	45.8%	-7.5%	21	13.1	1.7119	654	Yes
-10	-0.4692	0.2661	-0.41	-19.3%	44.8%	-7.5%	18	16.0	2.1353	802	No
0	-0.4721	0.2739	-0.41	-19.1%	44.3%	-7.5%	18	15.6	2.1401	781	No
10	-0.4775	0.2815	-0.42	-19.3%	44.8%	-7.5%	18	15.2	2.1464	762	No
20	-0.4838	0.2863	-0.43	-19.9%	45.8%	-7.5%	18	15.0	2.1520	752	No
30	-0.4891	0.2876	-0.43	-20.7%	46.6%	-7.2%	18	12.9	1.8563	646	Yes
40	-0.4922	0.2868	-0.43	-21.4%	46.6%	-6.8%	16	9.9	1.4158	494	Yes
50	-0.4935	0.2860	-0.42	-21.8%	46.0%	-6.4%	16	8.4	1.2027	421	Yes
60	-0.4939	0.2858	-0.42	-22.0%	45.3%	-6.1%	16	8.0	1.1423	400	Yes
70	-0.4941	0.2860	-0.42	-22.0%	44.7%	-5.9%	11	7.9	1.1309	395	Yes
80	-0.4942	0.2864	-0.42	-22.1%	44.4%	-5.7%	11	7.8	1.1167	390	Yes
90	-0.4942	0.2864	-0.42	-22.1%	44.3%	-5.7%	11	8.1	1.1604	405	Yes

Table 4.8b The Effect of the θ Ply on the D-spar Structural Performance and Failure; the lay up is $[\theta_1/25_{60}/\theta_1]_S$ (all glass case)

Tip Load = -100 LB

Θ°	Tip Defl.(")	Tip Rot.(°)	α	EI_error	GJ_error	1/√(EI*GJ)_error	Critical Brick	FS	Projected Tip Rot.(°) for FS=2	Projected Tip Load (lb)	Failure at Θ° Ply
-90	**-0.4995**	**0.4712**	**-0.54**	**-8.5%**	**4.8%**	**2.1%**	**18**	**8.2**	**1.9367**	**411**	No
-80	**-0.4991**	**0.4701**	**-0.54**	**-8.5%**	**4.9%**	**2.0%**	**18**	**8.2**	**1.9367**	**412**	No
-70	**-0.4977**	**0.4669**	**-0.54**	**-8.4%**	**5.3%**	**1.9%**	**18**	**8.3**	**1.9366**	**415**	No
-60	**-0.4949**	**0.4607**	**-0.54**	**-8.4%**	**5.8%**	**1.6%**	**18**	**8.4**	**1.9363**	**420**	No
-50	**-0.4899**	**0.4508**	**-0.53**	**-8.2%**	**6.5%**	**1.1%**	**19**	**8.6**	**1.9335**	**429**	No
-40	**-0.4824**	**0.4381**	**-0.53**	**-7.8%**	**7.1%**	**0.6%**	**21**	**7.7**	**1.6955**	**387**	Yes
-30	**-0.4744**	**0.4273**	**-0.52**	**-7.1%**	**7.1%**	**0.3%**	**21**	**7.6**	**1.6133**	**378**	Yes
-20	**-0.4698**	**0.4259**	**-0.52**	**-6.3%**	**6.4%**	**0.2%**	**18**	**9.0**	**1.9258**	**452**	No
-10	**-0.4713**	**0.4358**	**-0.53**	**-5.7%**	**5.3%**	**0.3%**	**18**	**8.8**	**1.9252**	**442**	No
0	**-0.4774**	**0.4507**	**-0.54**	**-5.5%**	**4.8%**	**0.5%**	**18**	**8.6**	**1.9277**	**428**	No
10	**-0.4850**	**0.4631**	**-0.54**	**-5.7%**	**5.3%**	**0.3%**	**18**	**8.3**	**1.9321**	**417**	No
20	**-0.4915**	**0.4692**	**-0.55**	**-6.3%**	**6.4%**	**0.2%**	**18**	**8.3**	**1.9367**	**413**	No
30	**-0.4957**	**0.4693**	**-0.55**	**-7.1%**	**7.1%**	**0.3%**	**18**	**8.2**	**1.9266**	**411**	Yes
40	**-0.4975**	**0.4676**	**-0.55**	**-7.8%**	**7.1%**	**0.6%**	**16**	**6.8**	**1.5866**	**339**	Yes
50	**-0.4982**	**0.4672**	**-0.54**	**-8.2%**	**6.5%**	**1.1%**	**16**	**6.2**	**1.4433**	**309**	Yes
60	**-0.4987**	**0.4681**	**-0.54**	**-8.4%**	**5.8%**	**1.6%**	**16**	**6.2**	**1.4602**	**312**	Yes
70	**-0.4991**	**0.4696**	**-0.54**	**-8.4%**	**5.3%**	**1.9%**	**16**	**6.8**	**1.5881**	**338**	Yes
80	**-0.4994**	**0.4708**	**-0.54**	**-8.5%**	**4.9%**	**2.0%**	**16**	**7.8**	**1.8295**	**389**	Yes
90	**-0.4995**	**0.4712**	**-0.54**	**-8.5%**	**4.8%**	**2.1%**	**18**	**8.2**	**1.9367**	**411**	No

Table 4.8c The Effect of the θ Ply on the D-spar Structural Performance and Failure; the lay up is $[\theta_1(c)/20_6(c)/20_6(gl)/20_6(c)/\theta_1(c)]_S$ (hybrid case)

Chapter 5

D-Spar Fabrication

In the previous chapter, the design of three D-spars was described. Only the hybrid D-spar and the all-carbon D-spar were fabricated. The fabrication of all-glass D-spar did not materialize because of budget constraints. The fabrication was done at the Material Research Laboratory, Industrial Technology Research Institute (ITRI) in Taiwan. The engineers of the laboratory are familiar with the bladder process and they have been using this process in sporting goods applications. The fabrication was jointly carried out by a team composed of ITRI's engineers and researchers from Stanford University.

The bladder process uses an inflatable mandrel to pressurize the laminate surface. The inflatable mandrel is inflated from an external source, and the pressure is transferred to the laminate panel surface. The laminate surface is pressed against a female mold to a give smooth surface finish.

In this chapter, we describe the tooling used in the D-spar fabrication, the fabrication process, and problems faced at the earlier stages of D-spar fabrication.

5.1 Tooling and Materials Used in D-Spar Fabrication

5.1.1 Materials

In previous chapters, we indicated T800/3900-2 Graphite/Epoxy material was used in D-spar design. However a different category of Graphite/Epoxy material was used in D-spar fabrication. The material used for D-spar fabrication was Torayca/P3051F. The difference in ply properties of these materials is shown in Table 5.1. There is not much difference in structural performance, as shown in Table 5.2. However, the manufactured D-spars are thicker than the designed one, because more plies are added to compensate for axial ply stiffness reduction (see Table 5.2).

5.1.2 Tooling

There are two types of tooling used in D-spar fabrication. A wooden mold was used for the lay-up process, and a hard female mold was used to produce a smooth surface finish.

5.1.2.1 Wooden Mold

The shape of the wooden mold is similar to that of the D-spar, and the dimension of the wooden mold is close to the D-spar internal dimension. However the D-spar internal dimension depends on skin thickness. The average skin thickness of the hybrid

D-spar and the all carbon D-spar is 0.14 inches and 0.13 inches respectively. The wooden mold was sized based on the internal dimension of the hybrid D-spar.

5.1.2.2 Female Tooling

The female tooling consists of four parts. They are two end plates, one base plate and one U-shaped plate (see Figure 5.1). The length of the base plate and U-shaped plate is about 82 inches.

5.2 Fabrication Process

The whole fabrication process can be broken into five stages.

5.2.1 Pre-Lay-up Preparation

At this stage, the pre-impregnated aligned fibers (called prepregs) are sized to the correct length, width and ply orientation according to the laminate schedule of the respective D-spar. Tables 5.3 and 5.4 show the laminate schedule of the hybrid and the all-carbon D-spars respectively. The width of prepregs is determined by the amount of overlap and the D-spar half-circumference length. The last step of this stage is to arrange the prepared prepregs into two stacks at each side of the wooden mold. The stacking sequence of the prepregs of each pile is according to the laminate schedule for the lay-up.

5.2.2 Lay-up

The steps are

a. Make markings at both ends of the wooden mold as shown in Figure 5.2. Each marking is about 1 cm. The marking is to facilitate the formation of the staggered overlap joint.

b. Wrap the wooden mold with a sheet of peel ply. This peel ply separates the wooden mold from the laminate and facilitates the removal of the wooden mold before the assembly of female tooling.

c. Lay the prepregs onto the wooden mold according to the laminate schedule (see Table 5.3 and 5.4). A long ruler is used to facilitate the lay-up (see Figure 5.3).

5.2.3 Inflatable Bag Preparation

The steps are:

a. Select a nylon bag that is slightly larger than the size of the D-spar.

b. Cut the bag at a length 6 inches more than the fabricated D-spar length.

c. Seal one end of the bag and fold the sealed end inward. The inward folding is a critical step. As the bag is being pressurized, the inward folding of the sealed end causes this end to push outward instead of expanding outward.

d. Attach a rubber nozzle to the other end of the bag (see Figure 5.4a). The sealing is done by wrapping a string of prepregs and shrinkage tape (see Figure 5.4b).

5.2.4 Assembly

The steps are

a. Clean the two end-plates, base plate and U-shaped plate. Spray release agent on all surfaces of the plates.

b. Turn the U-shaped plate with the legs pointing upward.

c. Transfer the wooden mold (with uncured D-spar) to the U-shaped tooling.

d. Remove the wooden mold from the uncured D-spar (see Figure 5.5).

e. Insert the bag into the hollow section.

f. Attach both ends with a set of $[\pm 45^\circ_2]_T$ laminate (see Figure 5.6). This is to avoid physical contact between the nylon bag and the two end-plates.

g. Assemble the base plate and two end-plates. After the assembly, the uncured D-spar is enclosed, and the rubber nozzle remains outside.

h. Supply slight pressure to the bag through the nozzle and check for air leakage.

5.2.5 Curing

The whole assembly is then transferred to an oven for curing (see Figure 5.7). The curing steps are

a. Connect the nozzle to an air compressor unit.

b. Set the pressure to 85-90 MPa.

c. Set the oven temperature according to the curing cycle (see Figure 5.8).

5.3 Earlier Phase Fabrication Problems

Seven D-spars were made. Table 5.5 shows the order of the D-spar being fabricated and the condition of each D-spar. The first and second D-spars were the 8-layer all-carbon D-spars. This was to check and fine-tune the fabrication process. There was problem on removing the first 8-layer all-carbon D-spar. The U-shaped plate was modified with the legs opened outward by 1.9° in order to remove the D-spar from the tooling. Therefore, the cross-section of the fabricated D-spar is different from the design one (see Figure 5.11). The third and fourth D-spars have surface imperfection problems, and both D-spars are also not symmetric (see Figure 5.9) with reference to the mid-plane. The sixth D-spar was damaged because of a leakage of the bag during curing. The fifth and seventh D-spars were successfully fabricated with good surface finish and the required symmetry (see Figure 5.10). The fifth D-spar made is the hybrid D-spar, and the seventh is the all-carbon one. The surface imperfections and the non-symmetry problems may be related. The problem on non-symmetry D-spar was fixed by having a symmetric lay-up at the joints (staggered overlap joint). No surface imperfections were observed after fixing the non-symmetry problem.

5.4 Staggered Overlap Joint Design

One critical point in D-spar fabrication is the joint design. As mentioned earlier, the bend-twist coupled D-spar consists of two symmetric clamshells held together by either a butt joint or an overlap joint. Both the butt joint and overlap joint designs were not adopted in fabrication, as both designs have more disadvantages than the preferred design invented during the learning curve of the fabrication process. The new joint design is called staggered overlap joint design. Figure 5.12 shows the three possible joint designs. The disadvantages of a single overlap joint design are the thickness at the joint is doubly thicker than the thickness at the main skin and the strength of the joint is weakened by step-change in thickness distribution. The butt joint design carries the same disadvantages as those of the single overlap joint design and has an additional disadvantage of requiring more lay-up operation steps. The main advantages of the staggered overlap joint are that the step-change in skin thickness surrounding the joint is reduced to a minimum and the joint is strengthened.

Tables 5.3 and 5.4 show the lay-up sequence for the hybrid and the all carbon D-spar respectively. The symmetry of the lay-up is clearly seen in both tables. In addition to that, the number of ply layers near the mid-plane of the hybrid D-spar has been reduced from 56 (if a single overlap joint were used) to 39. Further away from the mid-plane, the number of ply layers reduce to 28. The stagger overlap joint design of the all-carbon D-spar is even better than that of the hybrid D-spar. At the mid-plane of the all-carbon D-spar, the number of ply layers is 34. Further away from the mid-plane, the number of ply layers reduces to 26.

Description	T800/3900-2 (Graphite/Epoxy)	Torayca/P3051F (Graphite/Epoxy)
E_x(msi)	23.2	17.5
E_y(msi)	1.3	1.3
E_s(msi)	0.9	0.8
ν_x	0.28	0.3

Table 5.1 Ply Properties of T800/3900-2 and Torayca/P3051F.

Tip Load = -100 LB

D-Spar	Material	Laminate Schedule	Tip Defl.(")	Tip Rot. (°)	α	EI_error	GJ_error	1/√EI*GJ_error	Remark
Hybrid	T800/3900-2	$[70^*/20_6/20_6^*/20_6/70^*]$	-0.499	0.470	-0.54	-8.4%	5.3%	1.9%	*: glass
Hybrid	Torayca/P3051F	$[70^*/20_9/20_8^*/20_9/70^*]$	-0.499	0.434	-0.51	-13.1%	3.5%	5.4%	*: glass
Carbon	T800/3900-2	$[60/25_{15}/60]$	-0.456	0.448	-0.56	3.7%	17.0%	-9.2%	
Carbon	Torayca/P3051F	$[60/25_{24}/60]$	-0.450	0.417	-0.54	0.0%	15.0%	-6.8%	

Table 5.2 Structural Performance of the Hybrid and the Carbon D-spars Made by Two Different Carbon Materials.

Sequence No:	Layers of Prepregs	Ply Orientation (°)	Type of Material	Prepregs Width (cm)	Lay from Wooden Mold's Marking	
					Left-Side	Right-Side
1	1	70	Glass	22	0	-2
2	8	20	Carbon	22.1	0	-2
3	4	20	Glass	22.5	-2	-4
4	2	20	Carbon	22.7	1	-1
5	4	20	Glass	22.8	4	2
6	8	20	Carbon	23.0	2	0
7	1	70	Glass	23.4	2	0

Table 5.3 Lay-up Laminate Schedule for the Hybrid D-spar (see also Figure 5.2)

Sequence No:	Layers of Prepregs	Ply Orientation (°)	Type of Material	Prepregs Width (cm)	Lay from Wooden Mold's Marking	
					Left-Side	Right-Side
1	1	60	Carbon	22	1	-1
2	6	20	Carbon	22.2	0	-2
3	6	20	Carbon	22.7	2	0
4	6	20	Carbon	23.1	-2	-4
5	6	20	Carbon	23.7	4	2
6	1	60	Carbon	23.8	1	-1

Table 5.4 Lay-up Laminate Schedule for the All-Carbon D-spar (see also Figure 5.2)

Sequence No.	Description	Remarks
1	8-Layer all carbon D-spar	To check the fabrication process. D-spar was difficult to be removed from the U-shape tooling because of tooling problems
2	8-Layer all carbon D-spar	To check the fabrication process. D-spar had no problem to remove from the U-shape tooling. Some surface imperfections noticed
3	Hybrid D-spar	D-spar had surface imperfections and was not symmetric to the mid-plane.
4	All carbon D-spar	D-spar had surface imperfections and was not symmetric to the mid-plane.
5	Hybrid D-spar	D-spar was good and used for static test.
6	All carbon D-spar	D-spar was damaged because of leakage of inflatable bag during curing.
7	All carbon D-spar	D-spar was good.

Table 5.5 The Conditions of Seven D-spars Fabricated.

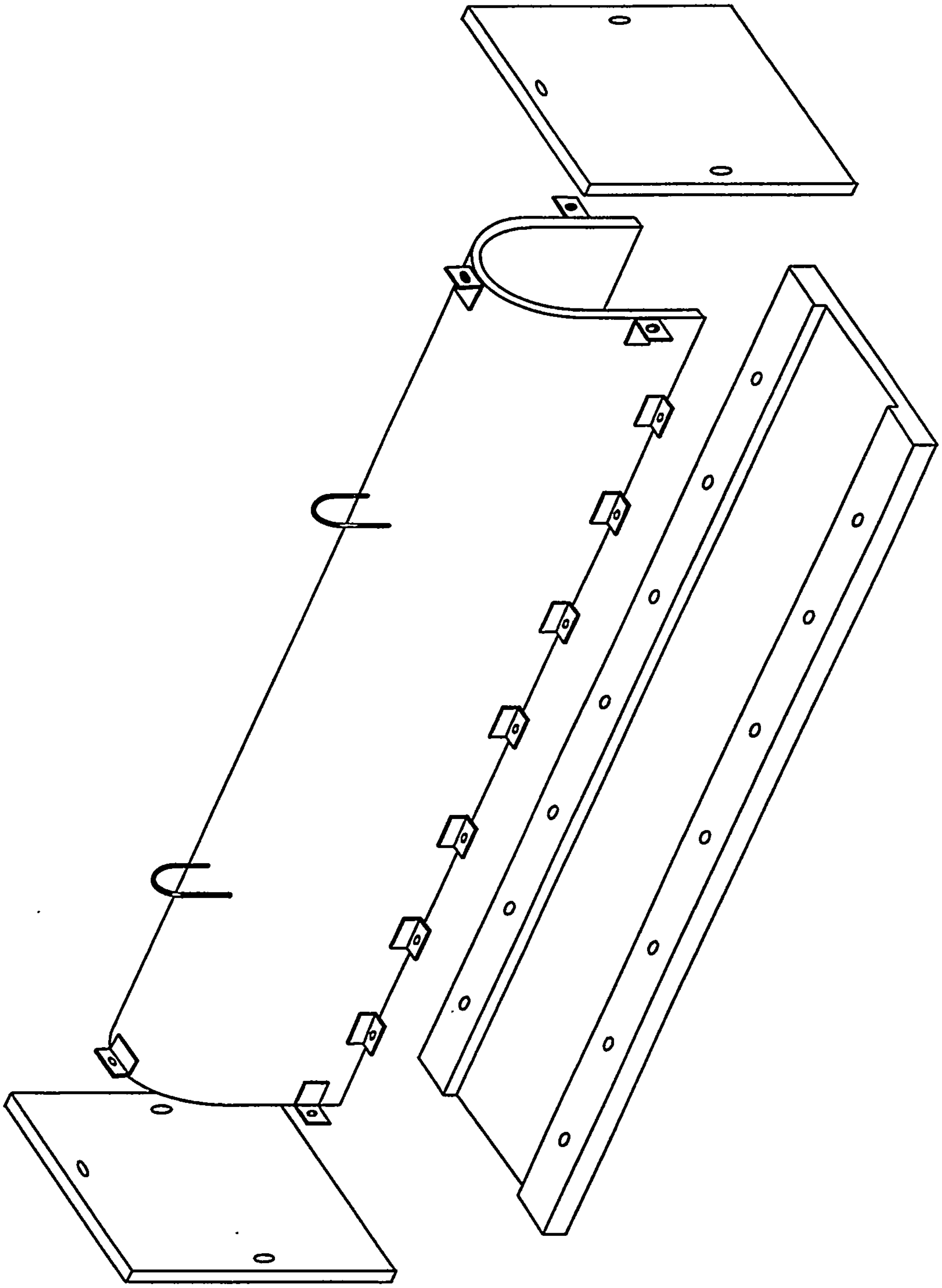

Figure 5.1 D-spar Female Tooling

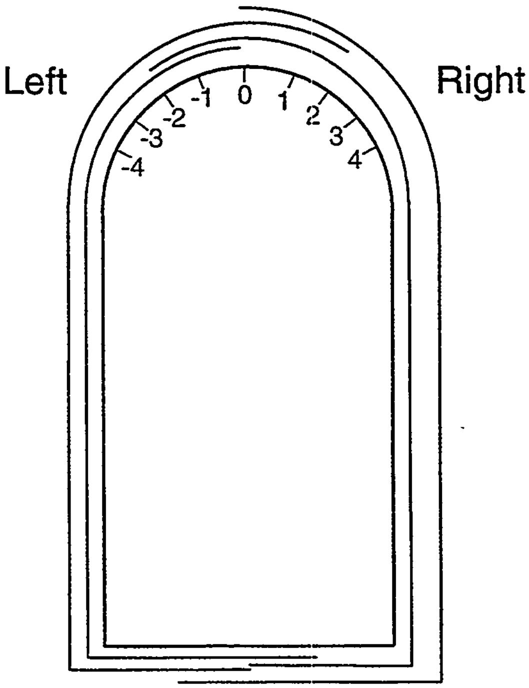

Figure 5.2 End-Marking on Wooden Mold for the Lay-up.

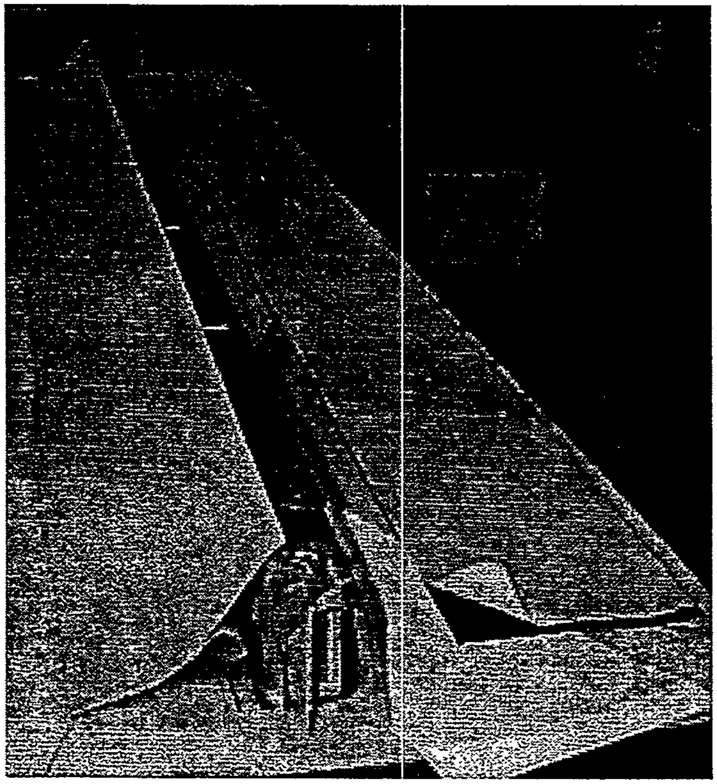

Figure 5.3 A Long Ruler Used for the Alignment.

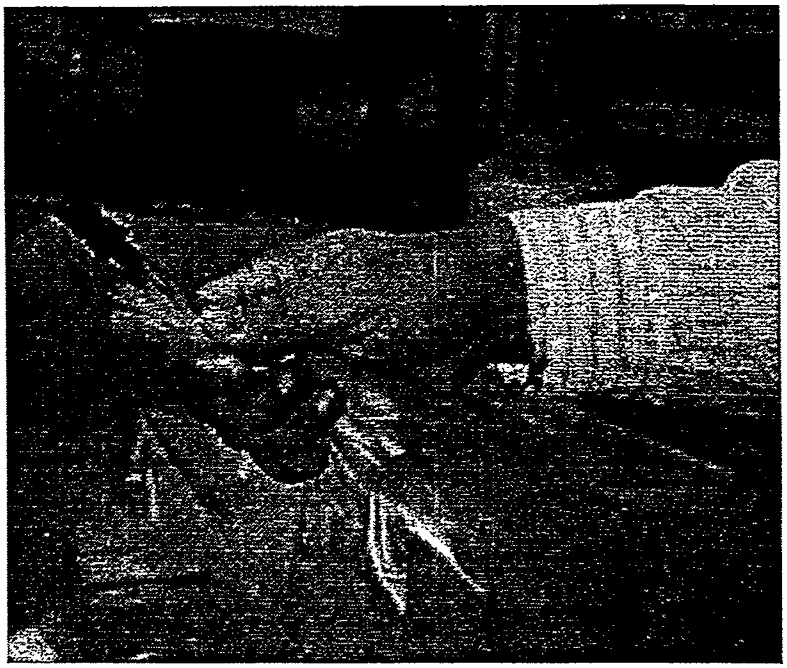

Figure 5.4a Place a Nozzle at the End of the Bag

Figure 5.4b Strings of Prepregs Wrapped around the Nozzle for Sealing

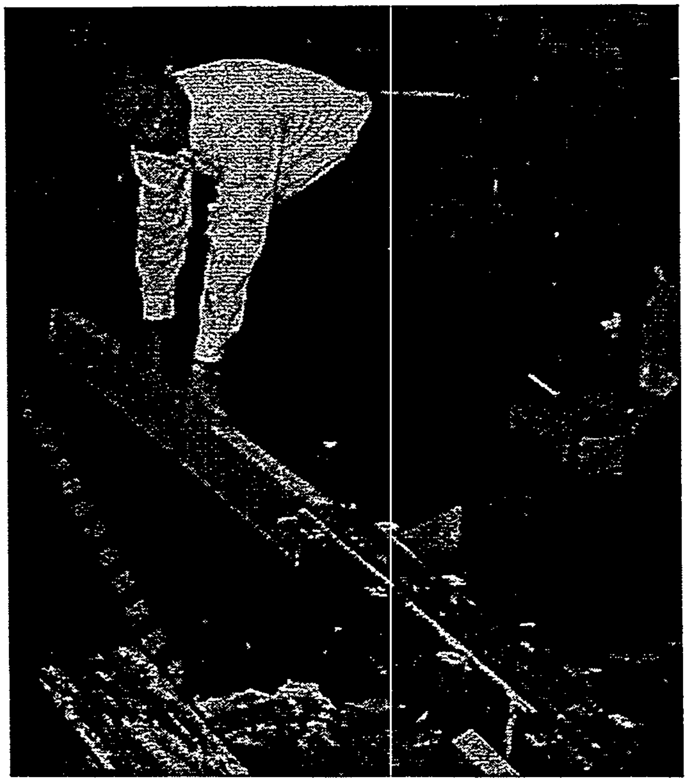

Figure 5.5 Remove the Wooden Mold Out of the Uncured D-spar

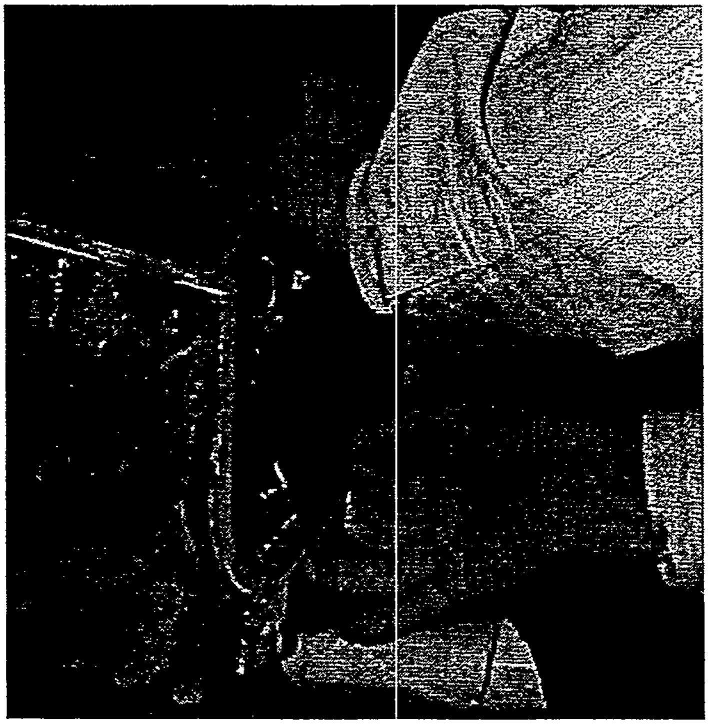

Figure 5.6 Protect Two Ends with a Sheet of $[\pm45°_2]_T$ Laminate

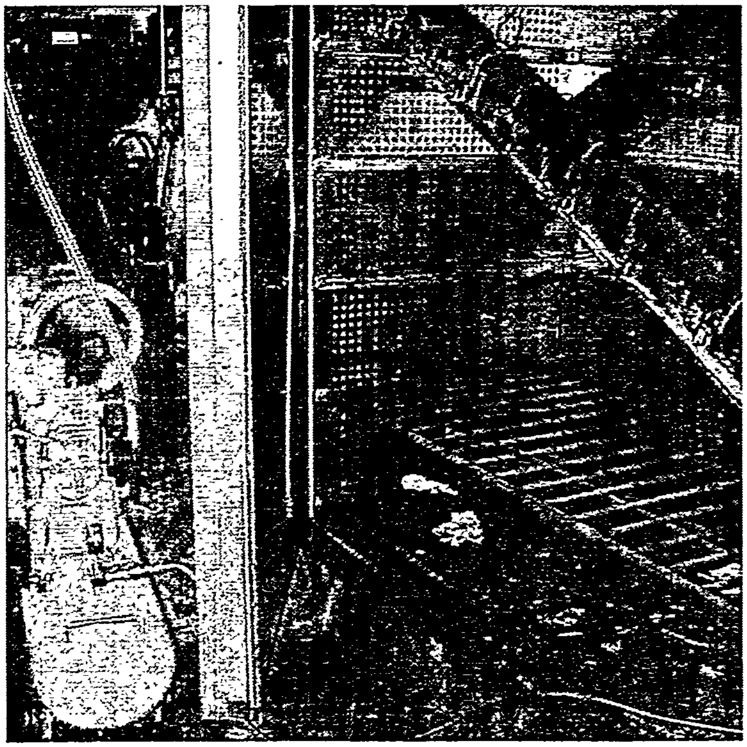

Figure 5.7 D-spar In Oven for Curing; Compressed Air Unit at Lower Left Corner

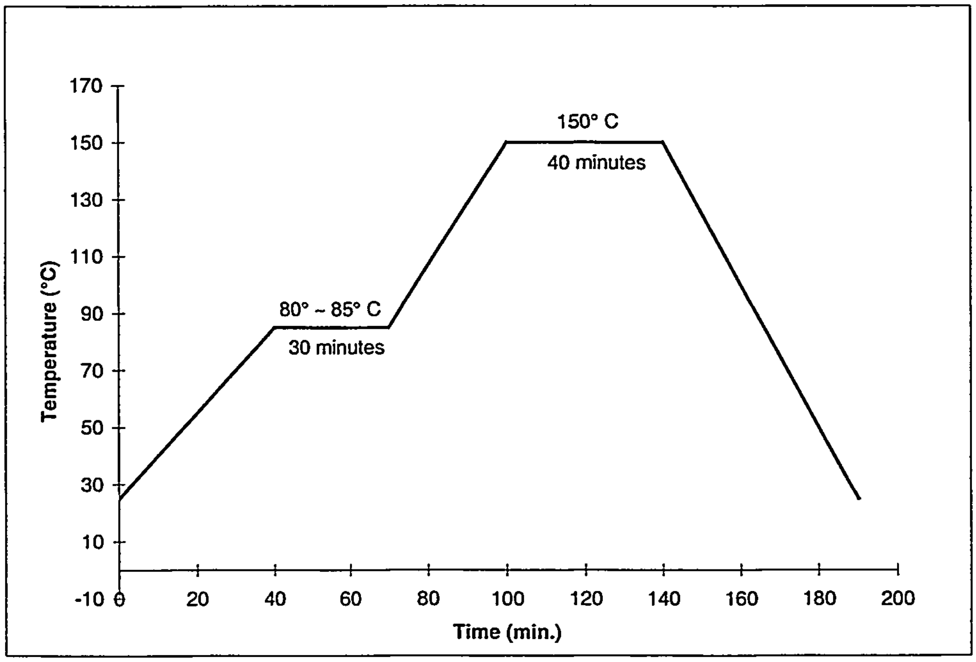

Figure 5.8 D-spar Curing Cycle

Figure 5.9 The Non-symmetric D-spar

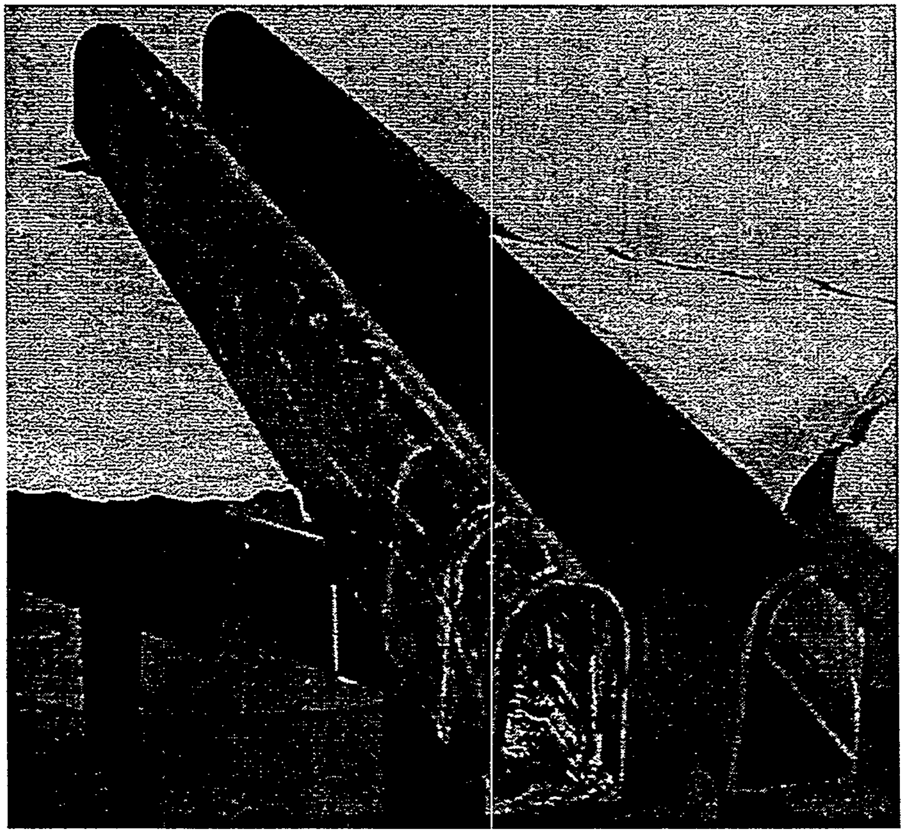

Figure 5.10 The Hybrid and All-Carbon D-spars

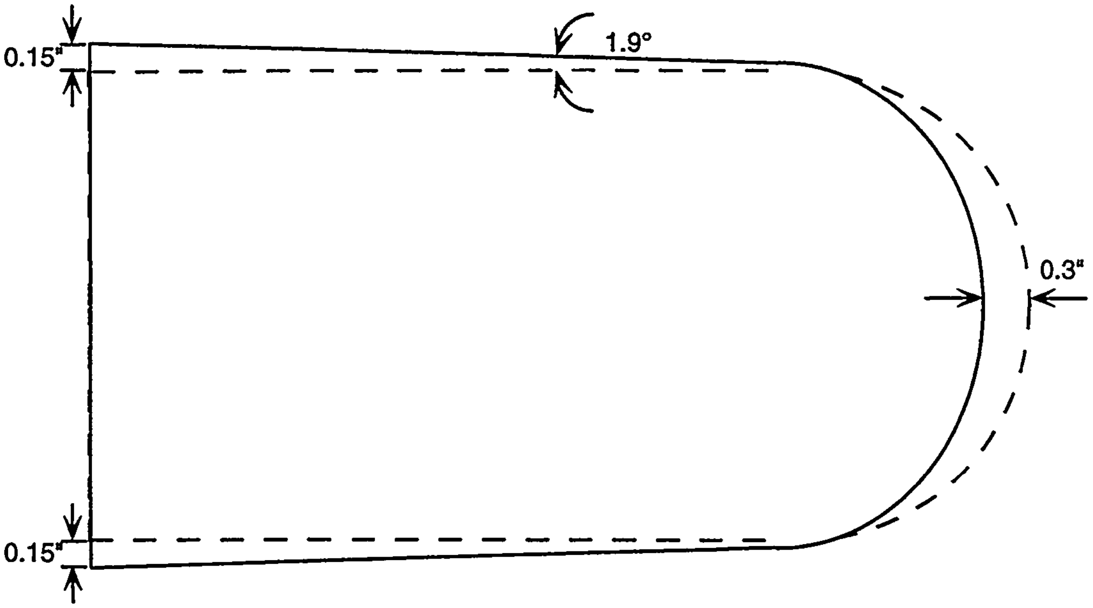

Figure 5.11 The Cross-Section Difference Between the Fabricated D-spar and the Design One

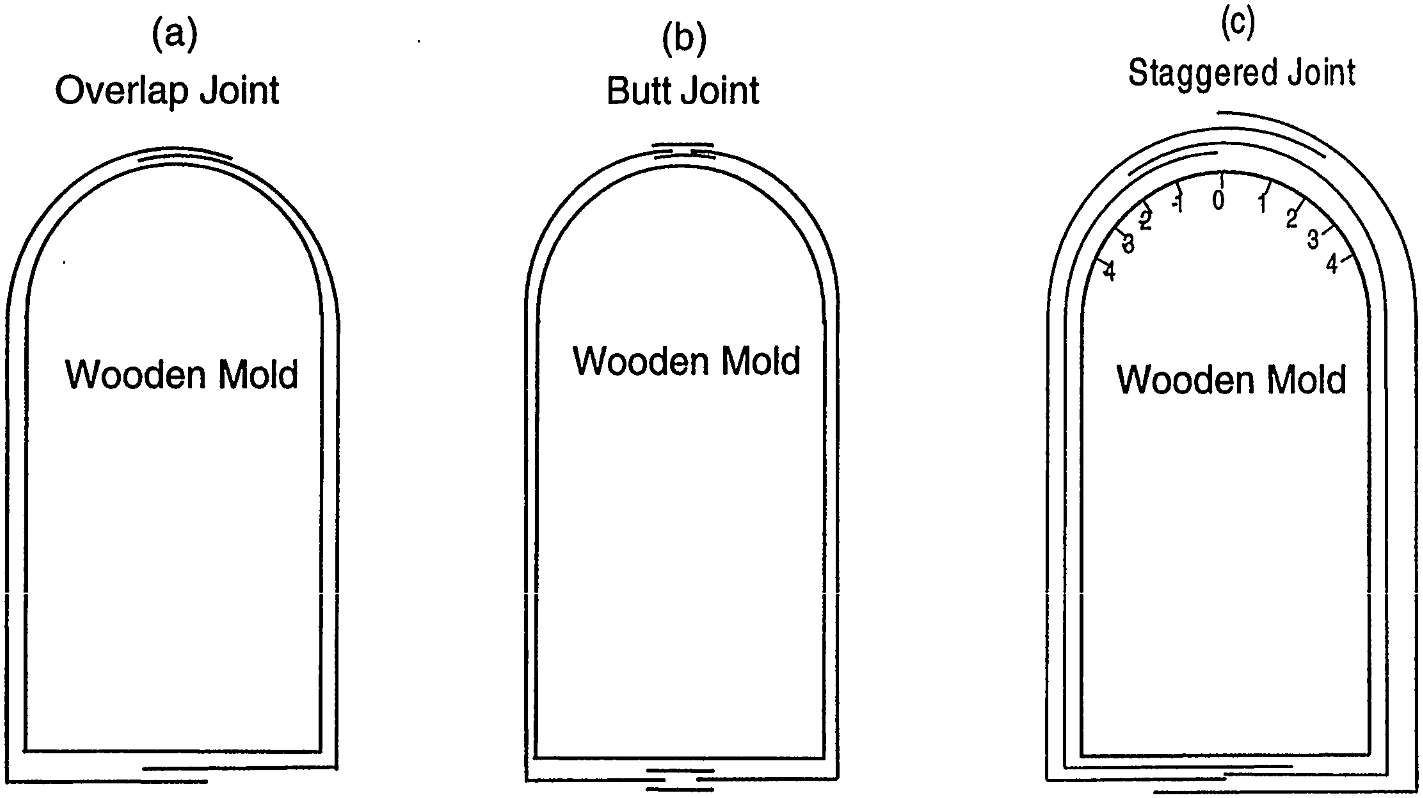

Figure 5.12 Three Possible Joint Designs.

Chapter 6

Static & Modal Testing

Two D-spars were successfully fabricated. Only the hybrid D-spar of the two good D-spars has been subjected to testing. The tests are the cantilever static test and the modal test. The static test was conducted at ITRI's testing facility, and the modal test was done at Sandia National Laboratories.

This chapter covers the static test set-up, the quality of the static test results, the comparison between the test results and the numerical predictions, and the post-modal test analysis.

6.1 Static Test Set-Up

The hybrid D-spar was subjected to the cantilever static test. The test set-up is shown in Figure 6.1. An aluminum block was inserted at the built-in end of the D-spar for reinforcement. The D-spar was then clamped tightly onto the test jig. The loads (dead weights were used) were applied vertically at the free end and were at a transverse distance 2.25" from the vertical wall of the D-spar (see Figures 6.2a and 6.2b). The dead weights were 5.84, 14.24, 21.04, 30.84, 37.04, 42.24, and 47.44 kg.

The measured parameters were vertical deflection, strains, and bend-induced twist. Displacement dial gauges were placed at locations x=56", 66" and 72" from the built-in end to measure respective vertical deflection. Two cross-bars (about 12" long) were positioned at locations x=66" and 72" to determine the bend-induced twist (see Figure 6.3). The strain gauges were attached at three longitudinal locations (see Figure 6.4). Two single-strain gauges were placed at x=0" at the top and bottom flat-skins. Three Rosettes were at x=6" (top and bottom skins) and at x=18" (top skin only).

6.2 Test Results

Each measured parameter was plotted against the loads, and a linear regression method was used to curve-fit the data to obtain normalized parameters (per unit pound force). Figures 6.5 and 6.6 show the vertical deflection measurements and the derived bend-induced twist under various tip loads, respectively. The strains at three locations are shown in Figures 6.7, 6.8 and 6.9. The plots indicate that all results are linearly correlated to loads except the bend-induced twist. The poor result on the bend-induced twist measurement may be due to inherent measurement error because the rotation is very small.

6.3 Comparison Between Estimated and Experimental Results

The normalized experimental results are compared to the results of two numerical models: 3D Beam and ANSYS models (the final geometry and material properties are used). Figures 6.10 to 6.14 show the vertical deflection, bend-induced twist, top skin longitudinal strain (e_1), transverse strain (e_2) and shear strain (e_6) comparisons, respectively. The hollow symbols in the graphs represent the experimental results divided by the respective tip loads. The solid symbol in the figures represents the normalized results after linear curved fitting through the experimental results. The scatter of the experimental results without linear curved fitting is clearly seen in those figures.

The comparisons between the experimental results and ANSYS results are excellent except for results located near the ends of the D-spar. The ANSYS model indicates that there are local deformation effects from the fixed boundary condition and applied load. As for the case of the 3D-Beam model, the experimental results are higher than the estimated results if no warping is included in the 3D-Beam model. The 3D-Beam estimated results are close to the test results once the torsion-related out-of-plane warping has been included. As observed in Figures 6.11 and Figure 6.14, torsion-related out-of-plane warping has a significant effect on the magnitude of bend-induced twist and transverse shear. Both the twist angle and shear strain (e_6) are nearly doubled if warping is considered. The effect from warping tends to marginally increase the α estimate but has significant effect on the bend-induced twist angle.

6.4 Post-Modal Testing Analysis

The modal testing was completed by Sandia National Laboratories[13]. This section describes the parameter sensitivity study done in order to reduce the discrepancy between the experimental results and modal analysis results (ANSYS model).

Table 6.1 shows initial comparisons on modal frequencies between the experimental results and ANSYS results. The initial frequency discrepancy is huge and the minimum error is about 10%. The discrepancy is mainly because the D-spar was not fabricated to exact dimensions and the measured material properties are different from the specification. The dimensional deviation was discussed in Chapter 5. The differences on material properties are reflected in Tables 6.2a and 6.2b. The main differences are on the E_x modulus and the ply thickness.

The ANSYS model has been updated to include all the changes. The new results are shown in Table 6.3. Table 6.3 is not in the same order as Table 6.1; the beam modes, torsion modes and oval modes are re-grouped together for clarity. The percentage of errors for the beam modes (Seq. No. 1-4) is less than 4%; for the torsion modes (Seq. No. 5-7) less than 10% and for the oval modes (Seq. No. 9-14) less than 20%. To further reduce errors, especially those errors related to the beam and torsion modes, a parameter sensitivity study was carried out.

The basic input to the ANSYS modal analysis model is the geometry of the D-spar, the ply properties, and the laminate schedule at every section (including the overlap region) of the D-spar. The ply properties are the major uncertainty data input because the volume fraction of the resin usually is unknown. Therefore, the sensitivity study mainly focuses on ply property variations. It is also expected that the adjustments to ply properties are small, because the errors of the beam modes are less than 4%.

The adjustments are

a. reduction of E_x (both glass and graphite fibers) by a factor of 1.05,

b. increase of ply thickness (both glass and graphite fibers) by the same factor of 1.05,

c. changing of ply orientation of the main skins from 20° to 20.5°.

The same adjustment factor is used for both (a) and (b). This is to keep the product of E_x and ply thickness constant. By reducing E_x and increasing ply thickness by the same amount we approximate the situation where the amount of fibers is known, but the amount of resin could vary.

Table 6.4 shows the comparisons for modal frequencies after the adjustments. The improvements are clearly seen on the first flatwise bending mode, the first twisting mode, the cross-section shear mode and the oval modes — about a 3% improvement. Additional adjustments are not required because the weight of the D-spar and the skin thickness are close to the measured values (see bottom of Table 6.4). The first and second flatwise bending and torsion mode shapes for both the analytical model and modal test model are shown from Figures 6.15 to 6.18.

Seq. No:	Frequency (Hz)		Modal Assurance Criteria (MAC)	Mode Shape Description*
	Modal Test	Modal Analysis		
1	145.0	130.5	0.990	First flatwise bending (2,0)
2	282.1	219.7	0.888	First twist (1,1)
3	292.2	269.1	0.541	Edgewise bending
4	309.6	239.0	0.877	Second twist (2,1)
5	334.8	259.3	0.807	X-section shear
6	338.8	297.6	0.835	Second flatwise bending (3,0)
7	356.1	—	0.211	Ovaling**
8	438.7	—	0.476	Ovaling**
9	458.0	341.0	0.929	Third twist (3,1)
10	468.0	330.1	0.628	Ovaling (1)
11	475.1	328.2	0.682	Ovaling (uniform)
12	485.6	336.6	0.941	Ovaling (2)
13	495.6	348.6	0.878	Ovaling (3)
14	512.6	422.0	0.666	Third flatwise bending (4,0)
15	533.2	368.0	0.783	Ovaling (4)
16	575.4	398.5	0.891	Ovaling (5)

*: The numbers in the brackets are the nomenclature for describing the modal shapes.

**: Unable to fine a suitable mode because of low MAC value.

Table 6.1 Initial Comparisons for Modal Frequencies between the Experimental Results and Modal Analysis Results

Description	Graphite/Epoxy	Glass/Epoxy
E_x(msi)	17.5	5.6
E_y(msi)	1.3	1.2
E_s(msi)	0.8	0.66
ν_x	0.28	0.3
Ply Thickness (inches)	0.00605	0.00496

Table 6.2a The Material Properties used for D-spars Design.

Description	Graphite/Epoxy	Glass/Epoxy
E_x(msi)	19.35	6.2
E_y(msi)	1.3	1.2
E_s(msi)	0.7	0.60
ν_x	0.28	0.3
Ply Thickness (inches)	0.0055	0.00425

Table 6.2b The Measured Material Properties.

Seq. No:	Frequency (Hz)		Modal Assurance Criteria (MAC)***	Mode Shape Description*
	Modal Test	Modal Analysis		
1	145.0	148.6	0.990	First flatwise bending (2,0)
2	338.8	329.6	0.835	Second flatwise bending (3,0)
3	512.6	491.0	0.666	Third flatwise bending (4,0)
4	292.2	288.3	0.541	Edgewise bending
5	282.1	254.7	0.888	First twist (1,1)
6	309.6	280.2	0.877	Second twist (2,1)
7	458.0	411.9	0.929	Third twist (3,1)
8	334.8	290.0	0.807	X-section shear
9	468.0	393.4	0.628	Ovaling (1)
10	475.1	395.5	0.682	Ovaling (uniform)
11	485.6	403.9	0.941	Ovaling (2)
12	495.6	414.5	0.878	Ovaling (3)
13	533.2	435.7	0.783	Ovaling (4)
14	575.4	468.9	0.891	Ovaling (5)
15	356.1	--	0.211	Ovaling**
16	438.7	--	0.476	Ovaling**

*: The numbers in the brackets are the nomenclature for describing the modal shapes.

**: Unable to fine a suitable mode because of low MAC value.

***: Previous MAC values.

Table 6.3 Comparisons for Modal Frequencies Between the Experimental Results and Modal Analysis Results After Geometry and Material Properties adjustment.

Seq. No:	Frequency (Hz)			Mode Shape Description*
	Modal Test	Modal Analysis (Baseline)	Modal Analysis (Final)	
1	145.0	148.6	146.2	First flatwise bending (2,0)
2	338.8	329.6	330.3	Second flatwise bending (3,0)
3	512.6	491.0	496.1	Third flatwise bending (4,0)
4	292.2	288.3	281.3	Edgewise bending
5	282.1	254.7	264.6	First twist (1,1)
6	309.6	280.2	289.1	Second twist (2,1)
7	458.0	411.9	413.6	Third twist (3,1)
8	334.8	290.0	302.3	X-section shear
9	468.0	393.4	409.9	Ovaling (1)
10	475.1	395.5	412.2	Ovaling (uniform)
11	485.6	403.9	421.1	Ovaling (2)
12	495.6	414.5	431.4	Ovaling (3)
13	533.2	435.7	452.6	Ovaling (4)
14	575.4	468.9	485.5	Ovaling (5)
(a)	11.9 lb.	11.2 lb.	11.8 lb.	D-spar Weight
(b)	0.147"	0.142"	0.148"	Average Thickness

*: The numbers in the brackets are the nomenclature for describing the modal shapes.

Table 6.4 Comparisons for Modal Frequencies Between the Experimental Results and Modal Analysis Results After Fine Tuning.

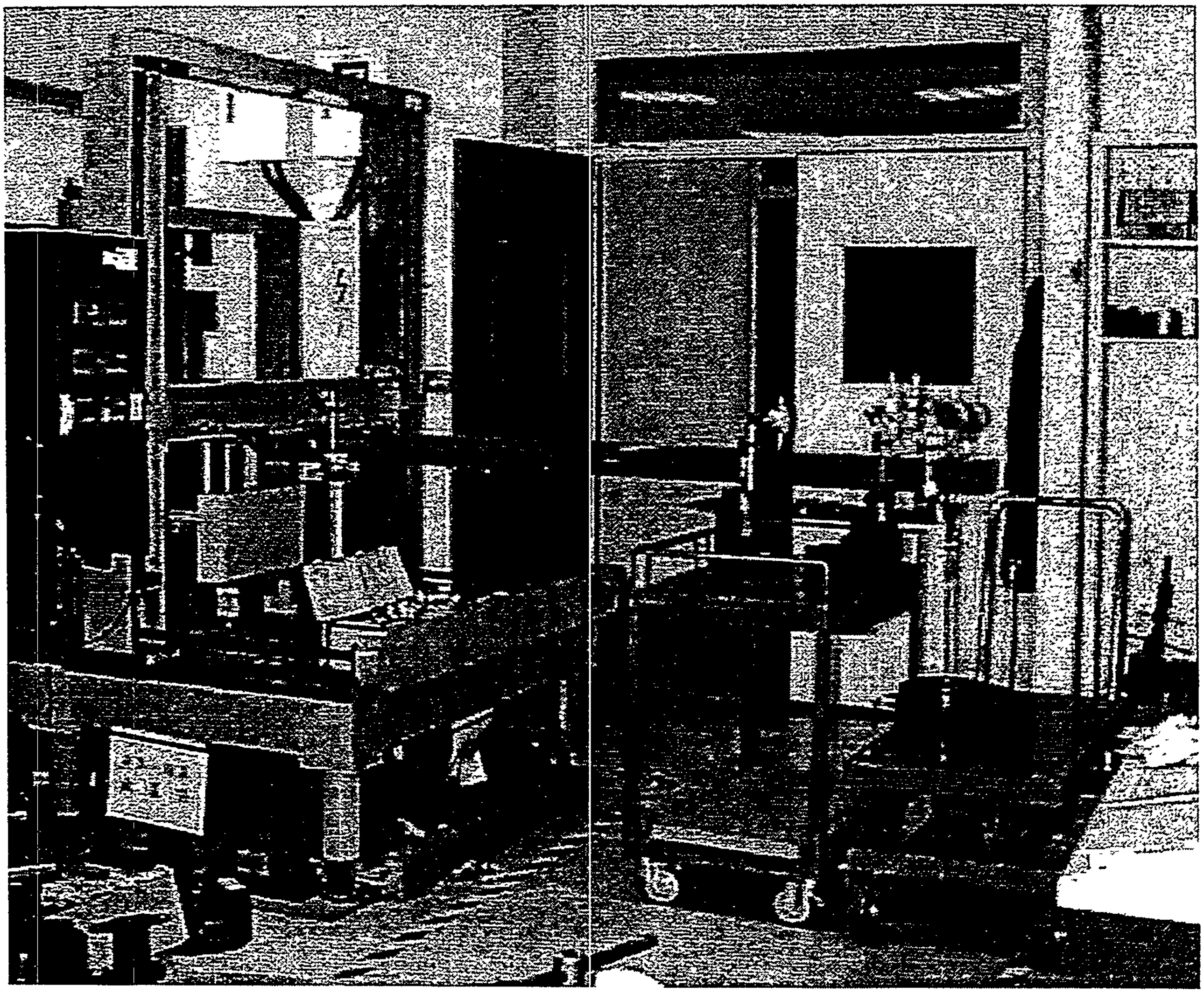

Figure 6.1 Static Test Set-Up

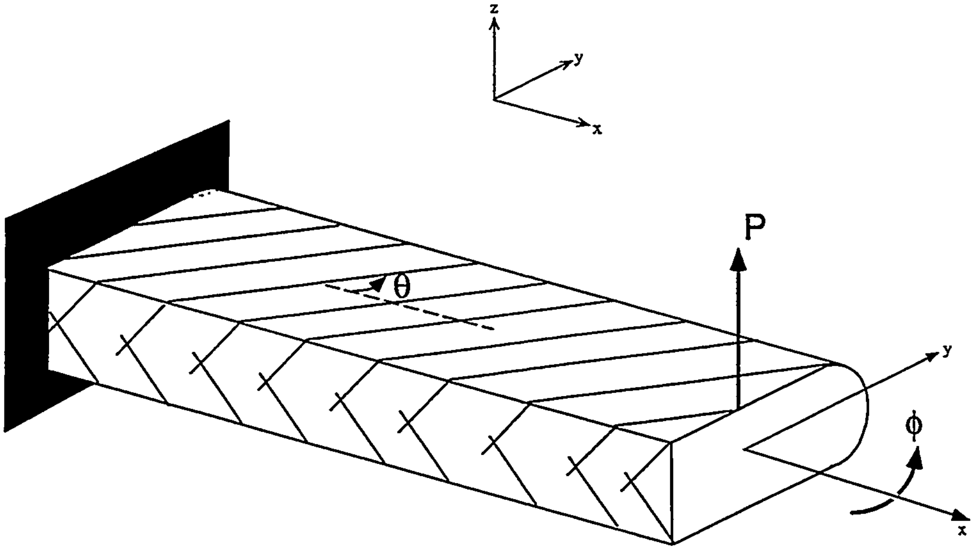

Figure 6.2a Definition of Reference Axis

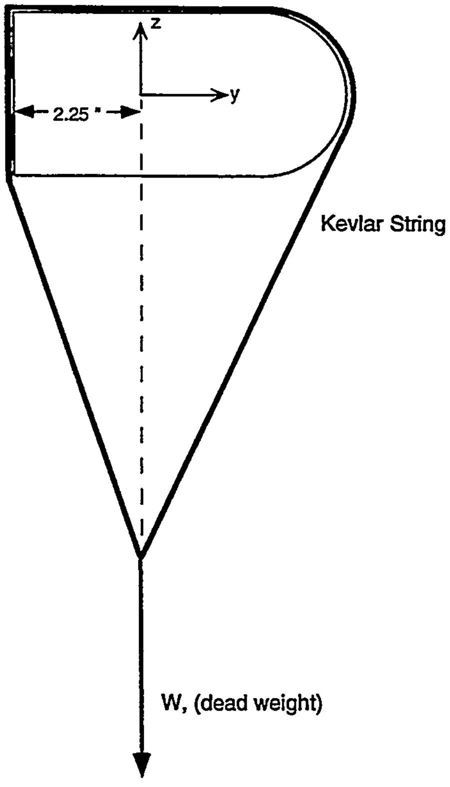

Figure 6.2b Application of Load

Figure 6.3 Placement of Two Cross-Bars for Twist Measurement

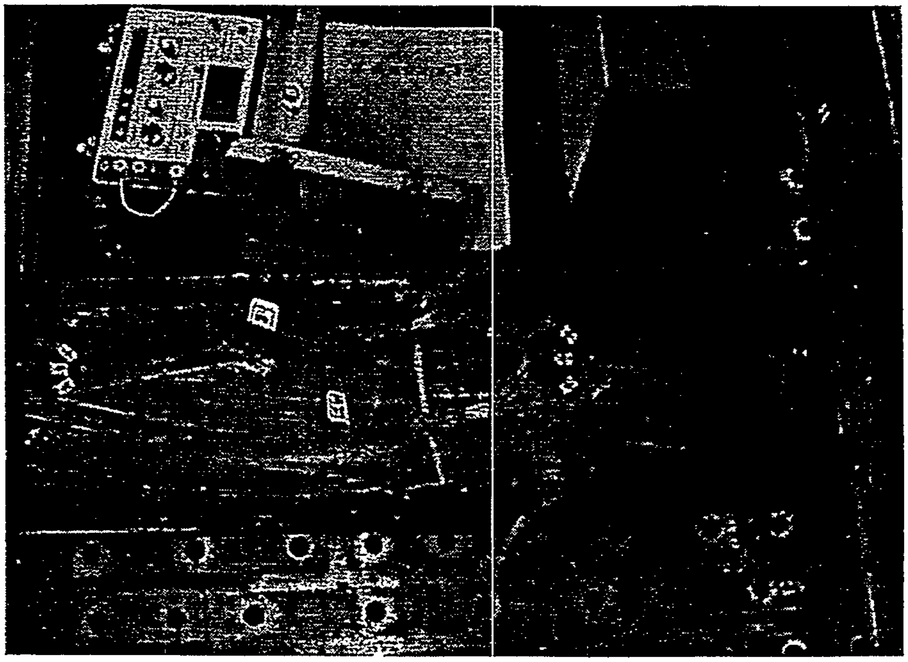

Figure 6.4 Strain Gauges Location at Top Surface

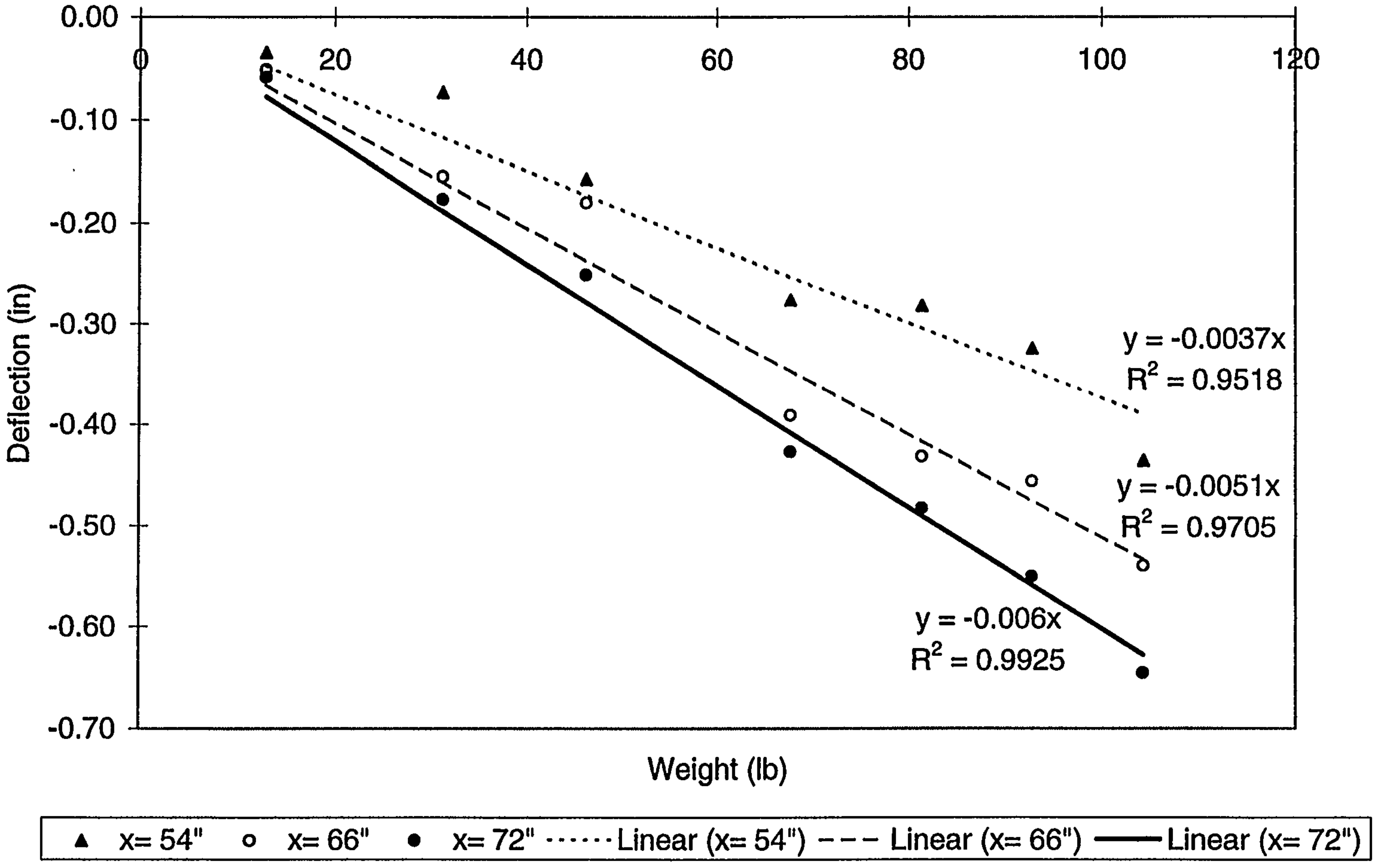

Figure 6.5 Vertical Deflection at the Measured Locations under Various Tip Loads

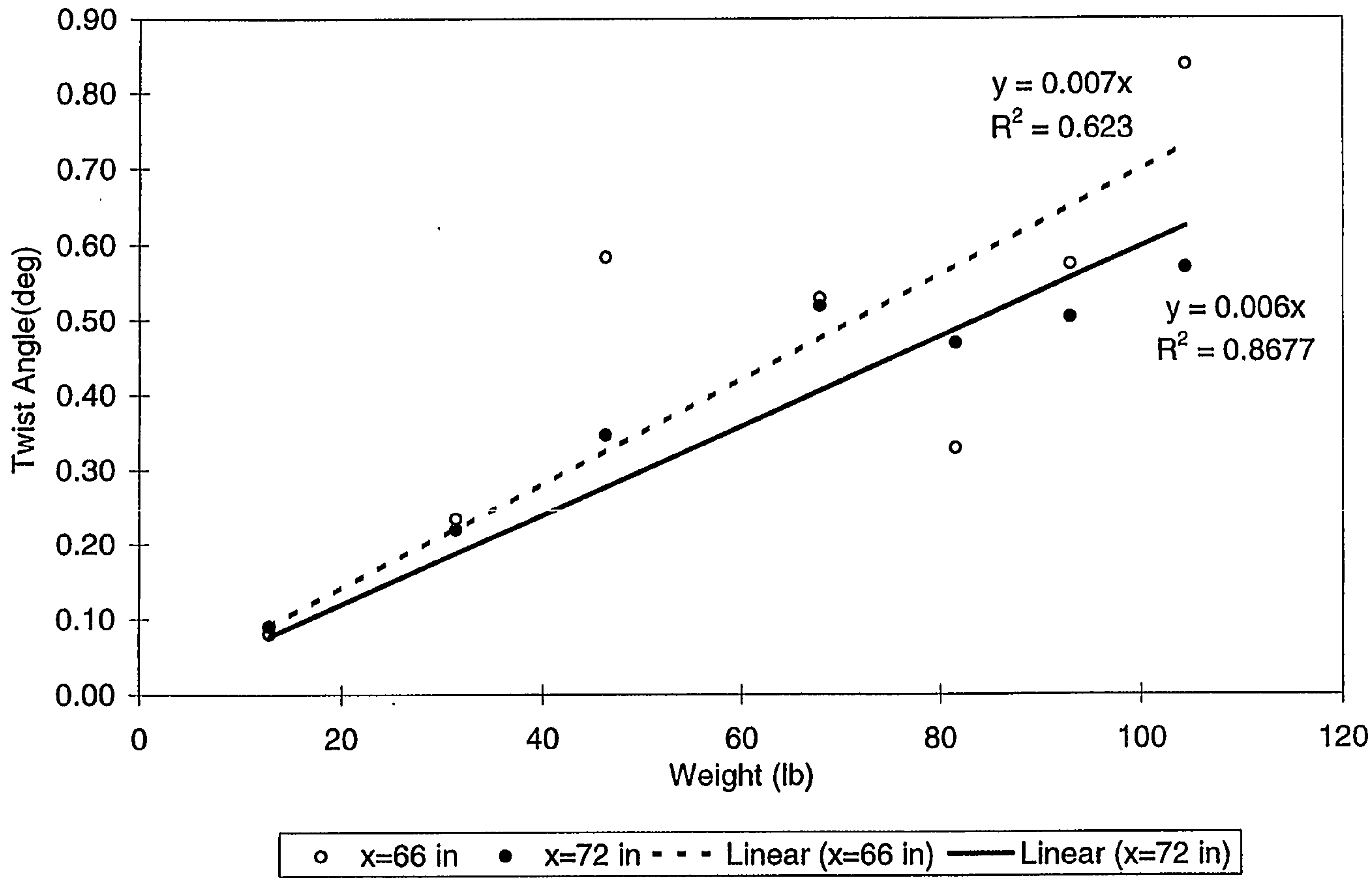

Figure 6.6 Bend-induced Twist at the Measured Locations under Various Tip Loads

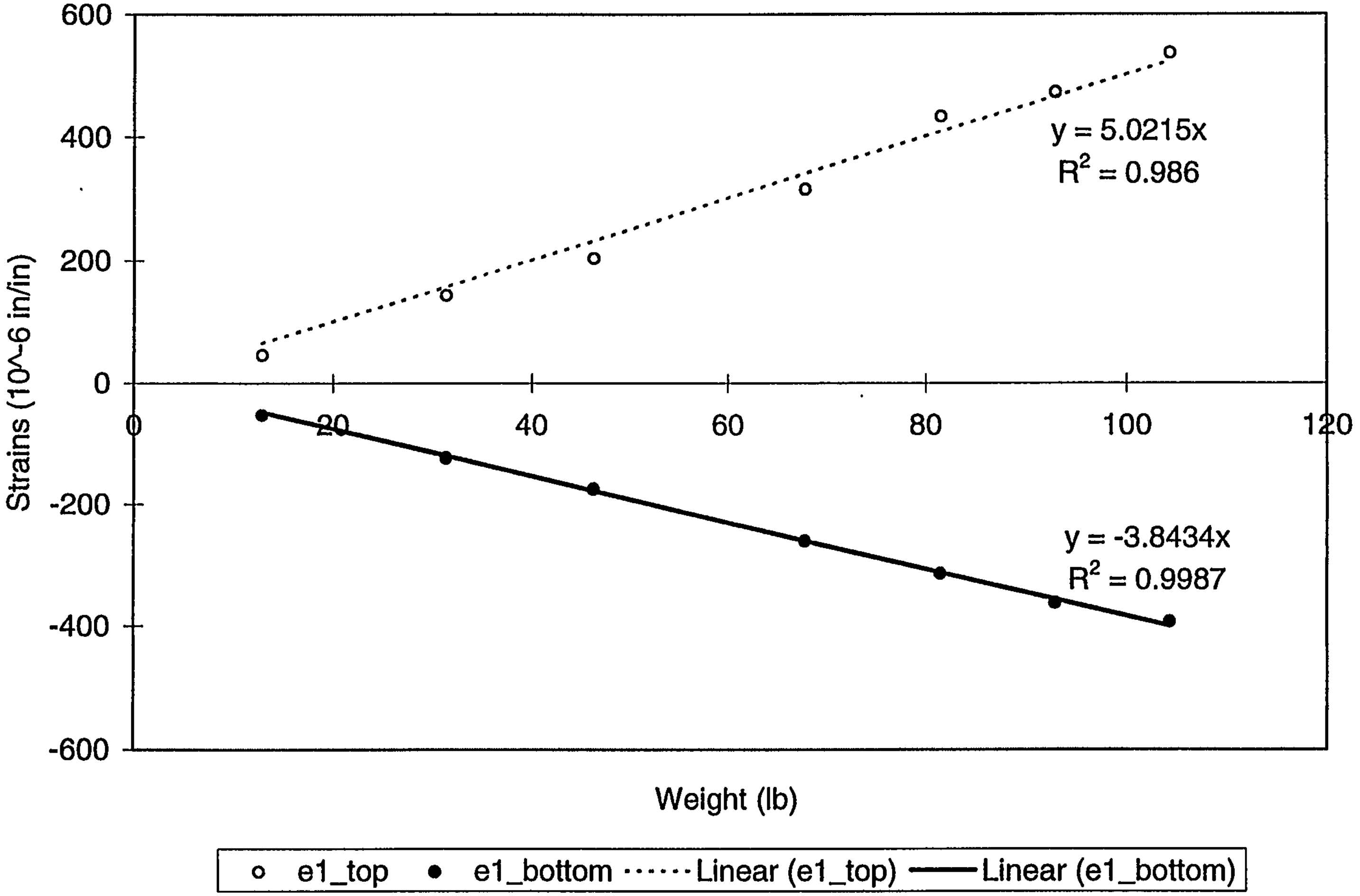

Figure 6.7 Longitudinal Strains at the Built-in End (x=0", y=0") under Various Tip Loads

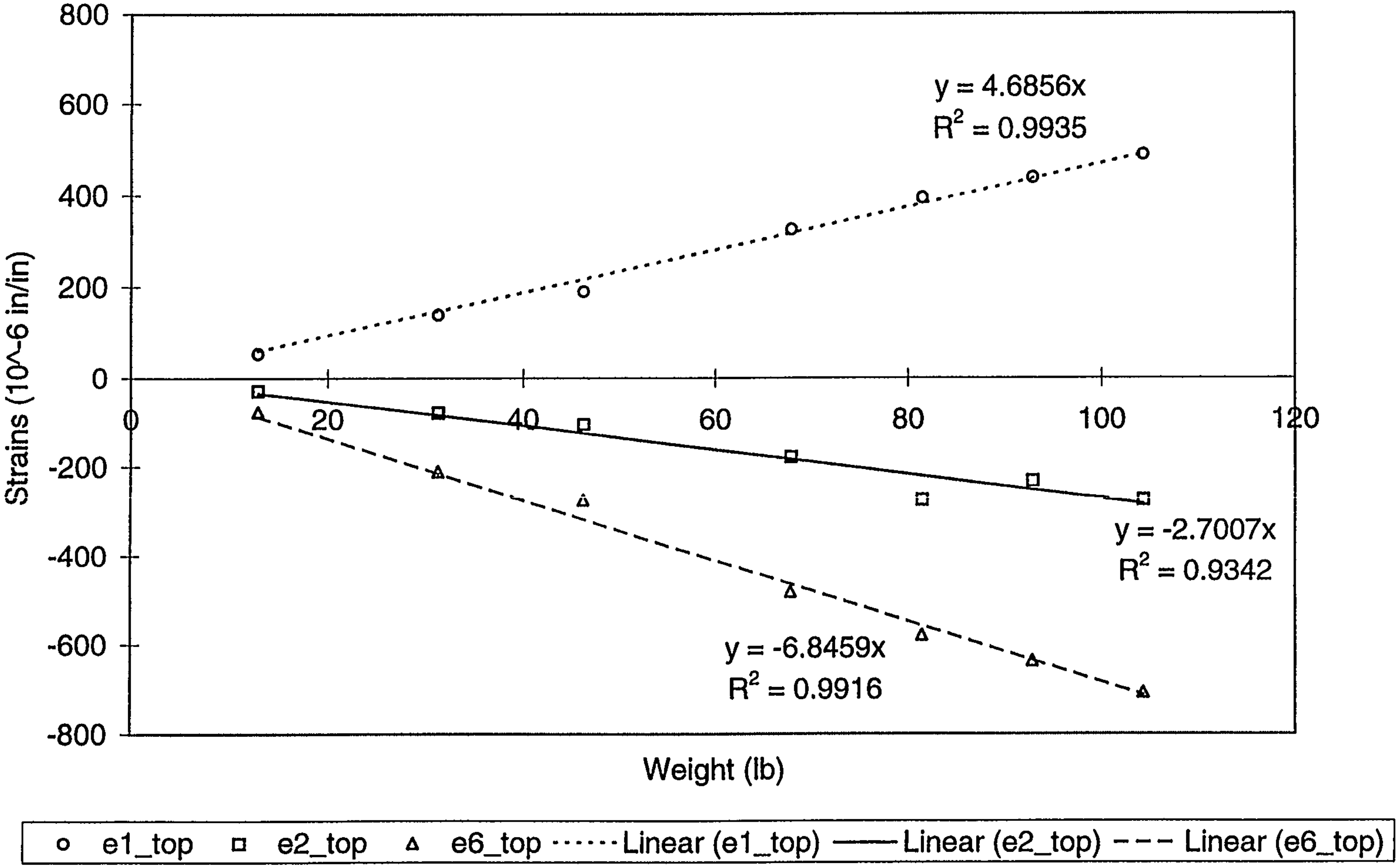

Figure 6.8a Strains at the Top Surface (x=6", y=0") under Various Tip Loads

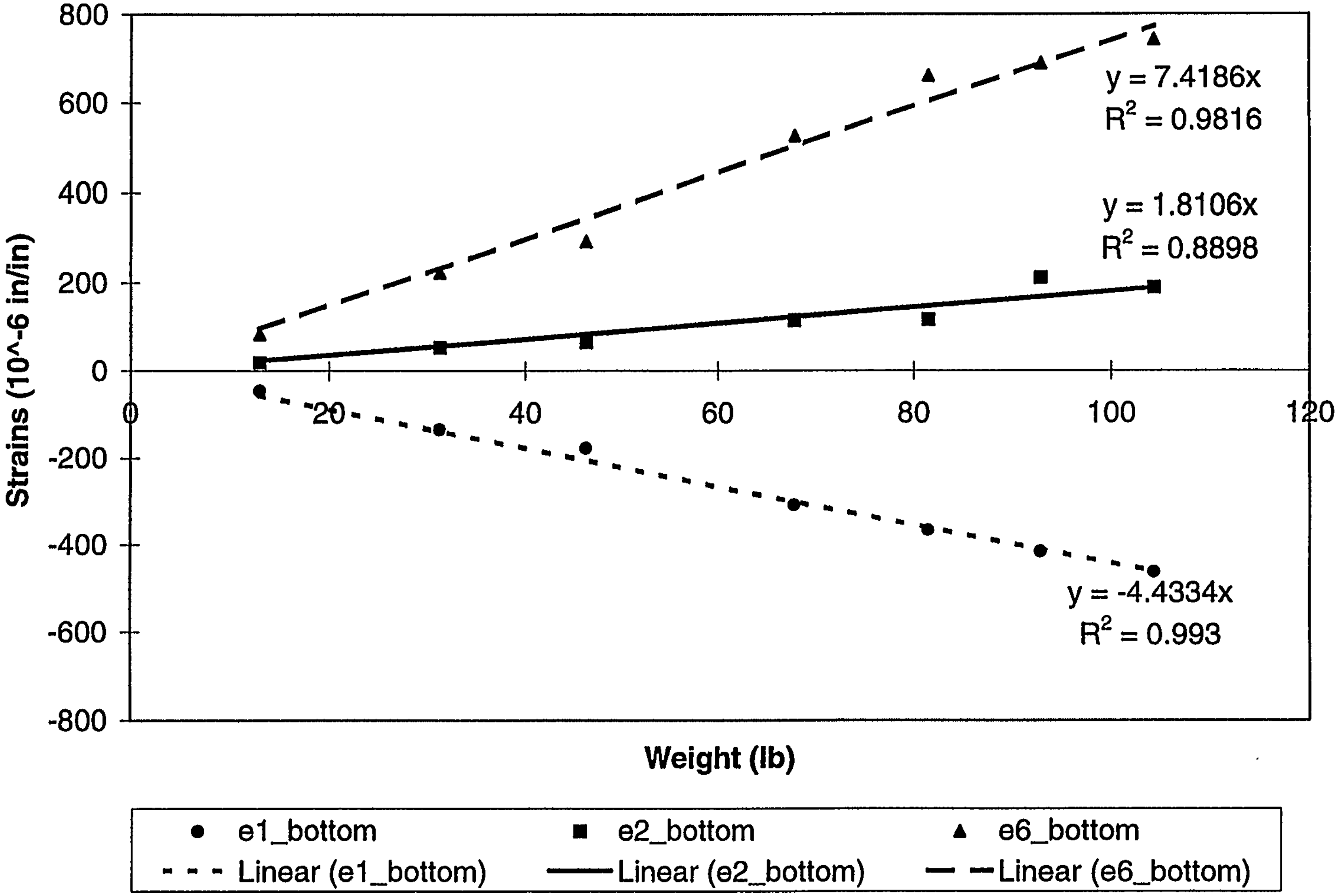

Figure 6.8b Strains at the Bottom Surface (x=6", y=0") under Various Tip Loads

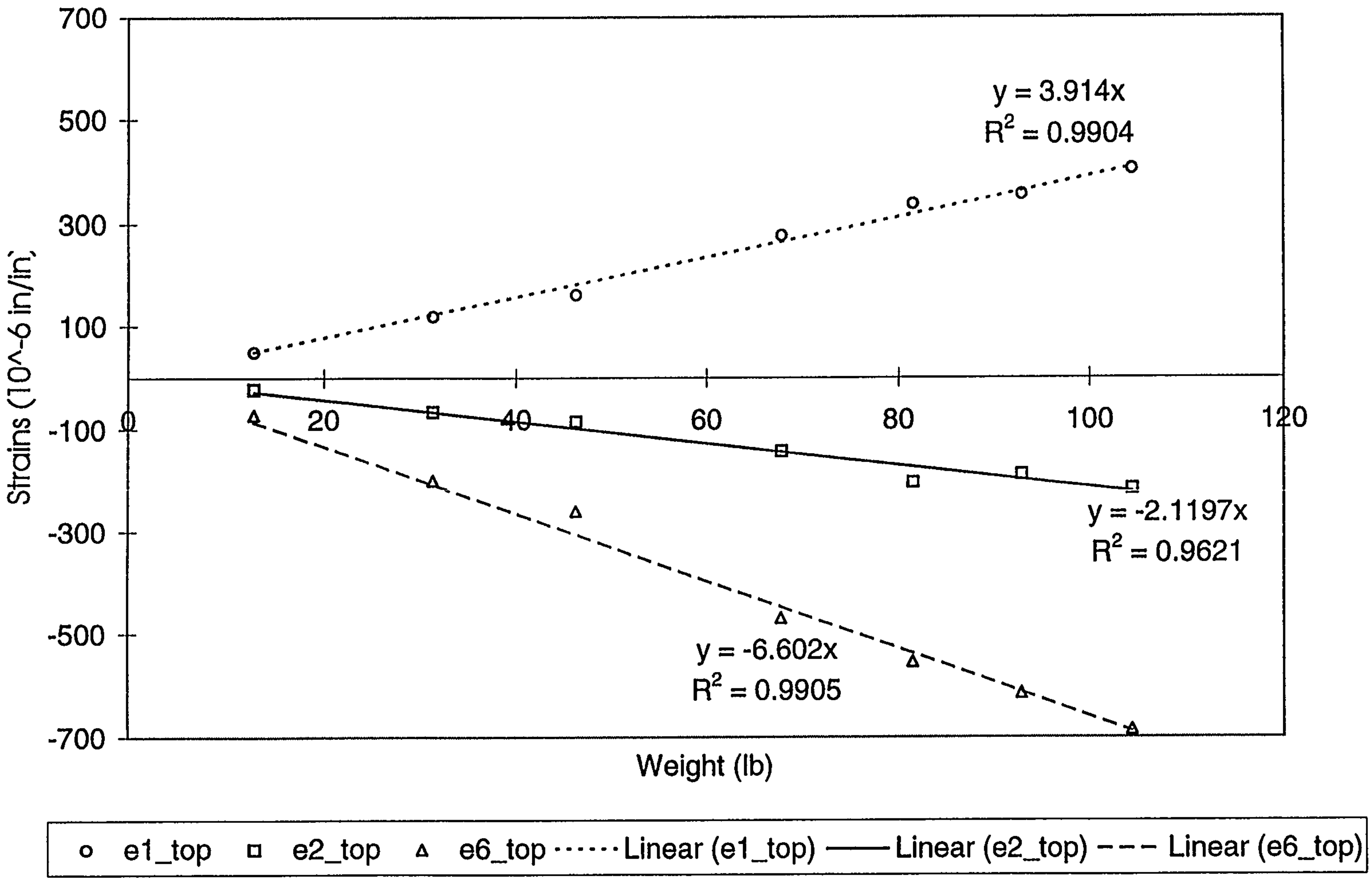

Figure 6.9 Strains at the Top Surface (x=18", y=0") under Various Tip Loads

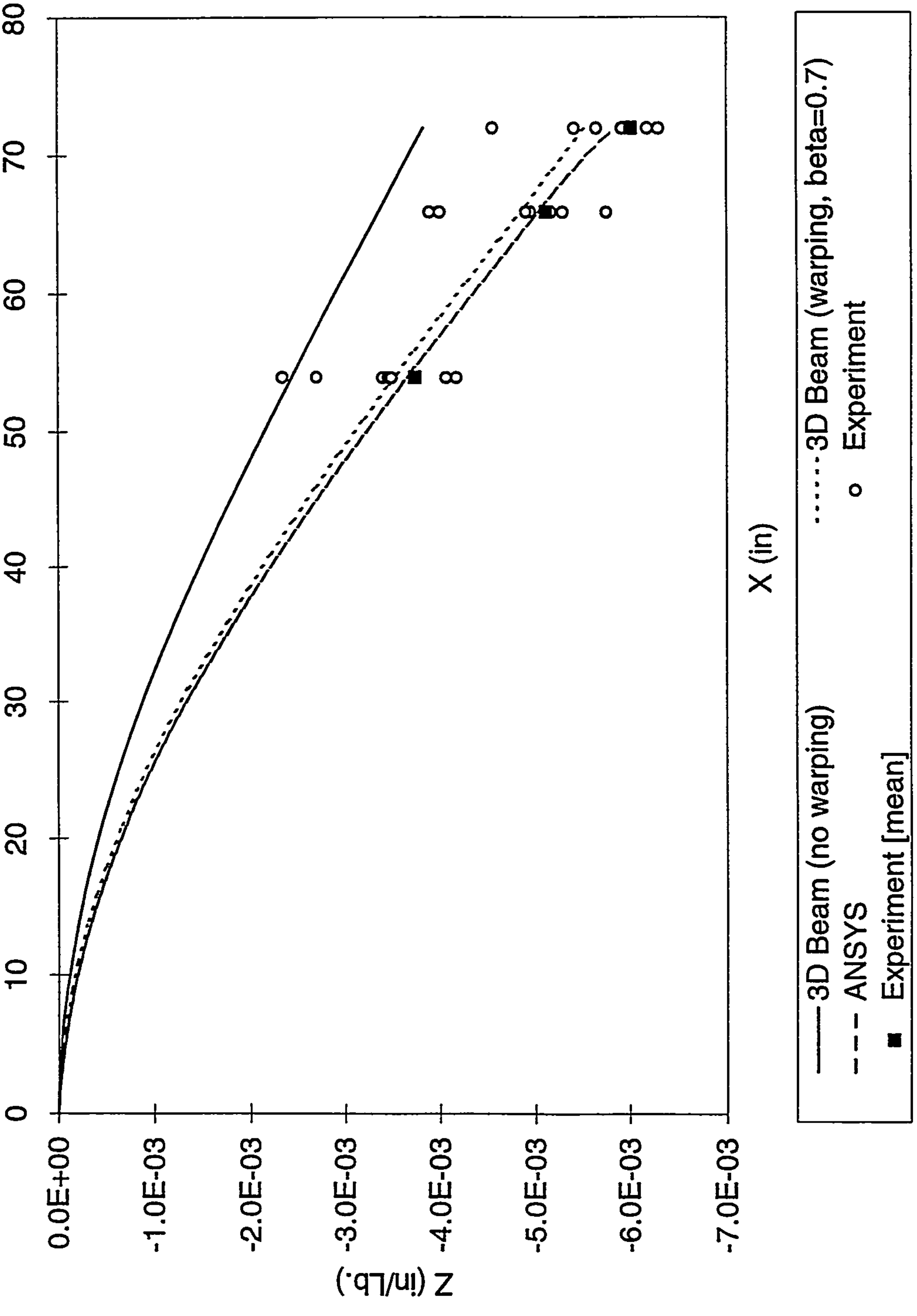

Figure 6.10 Static Deflection of the Hybrid D-spar Under Tip Unit Pound Force

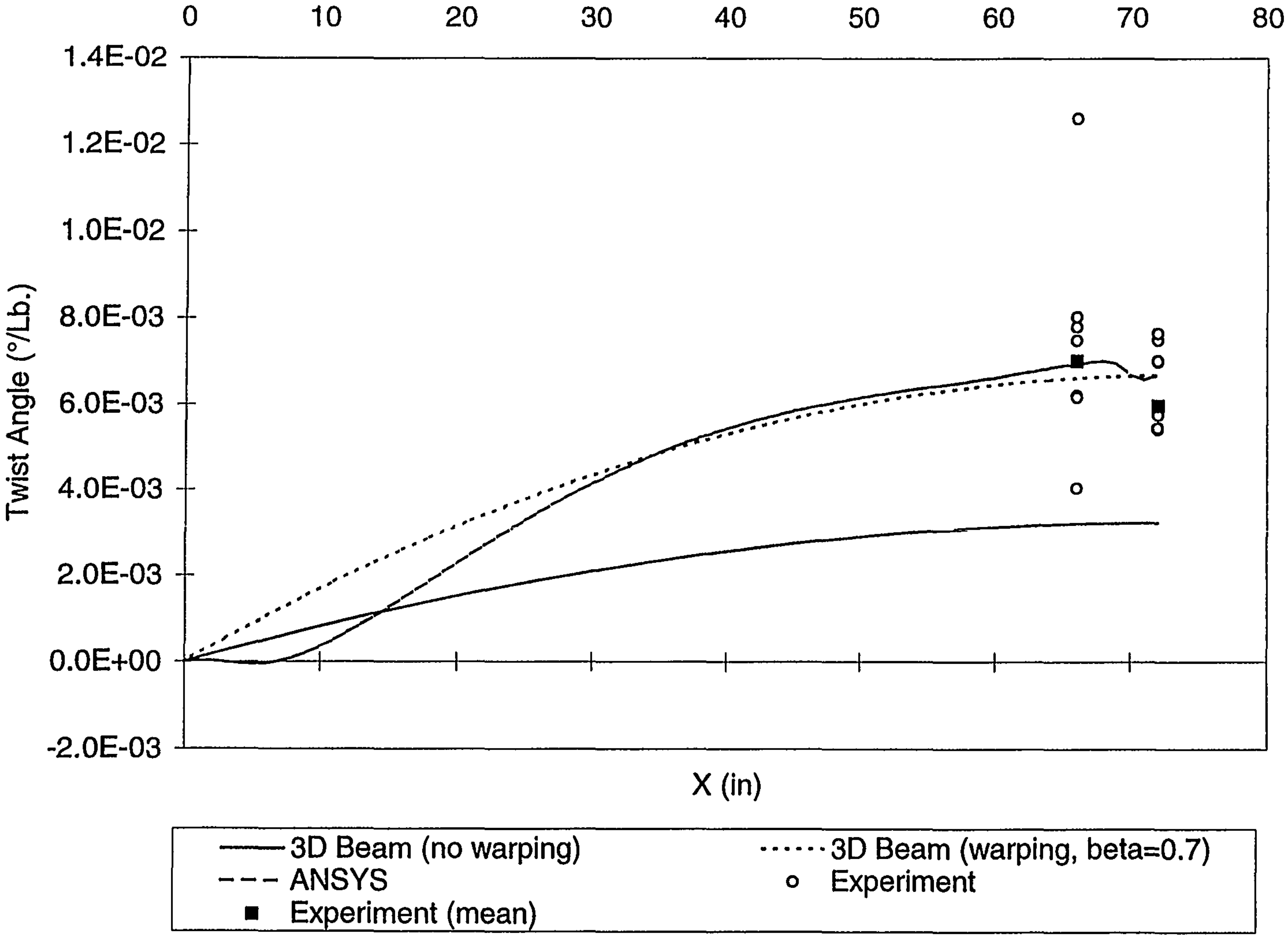

Figure 6.11 Bend-induced Twist of the Hybrid D-spar Under Tip Unit Pound Force

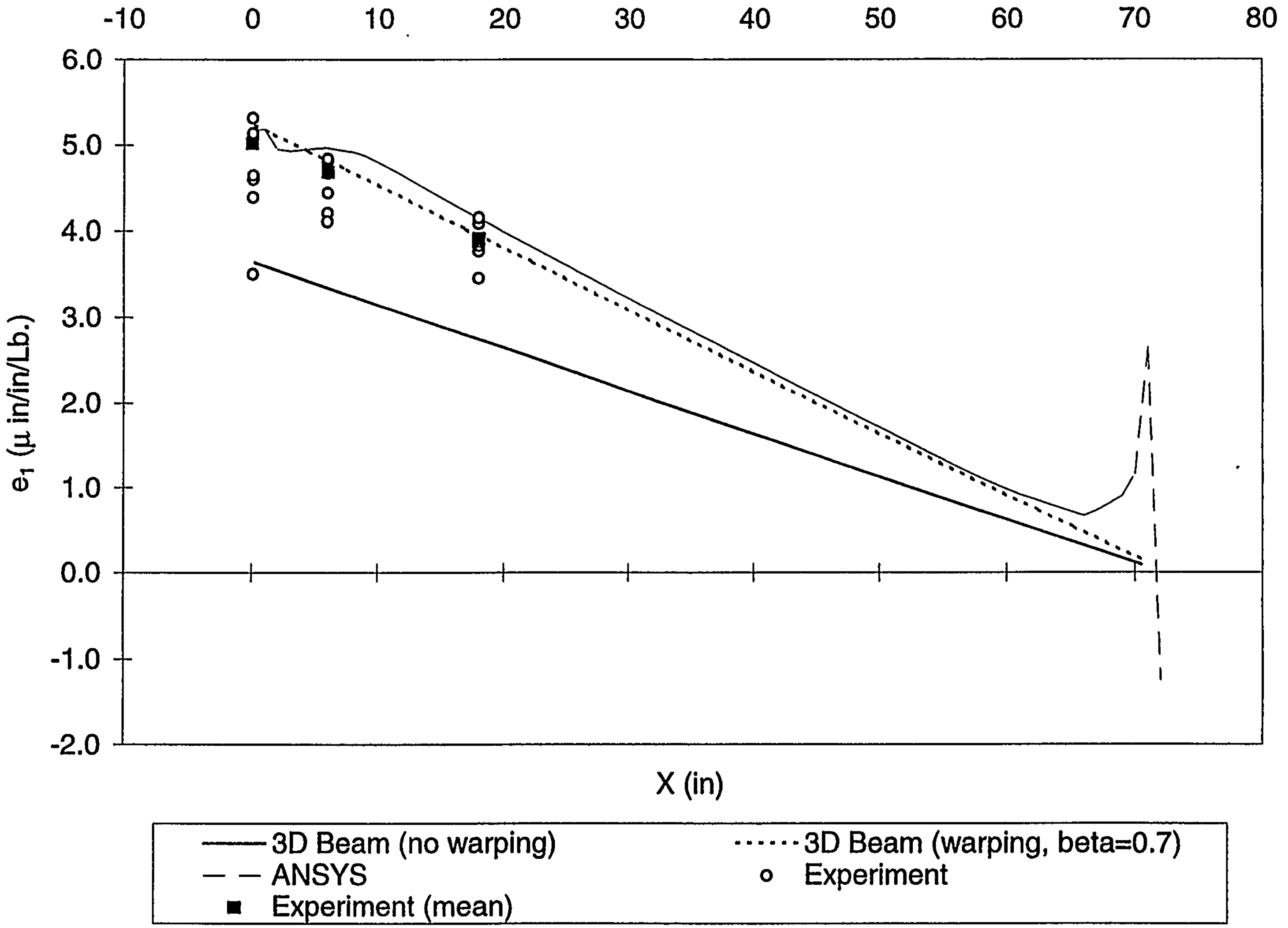

Figure 6.12 Longitudinal Strain (e_1) at the Top Skin (y=0") of the Hybrid D-spar Under Tip Unit Pound Force

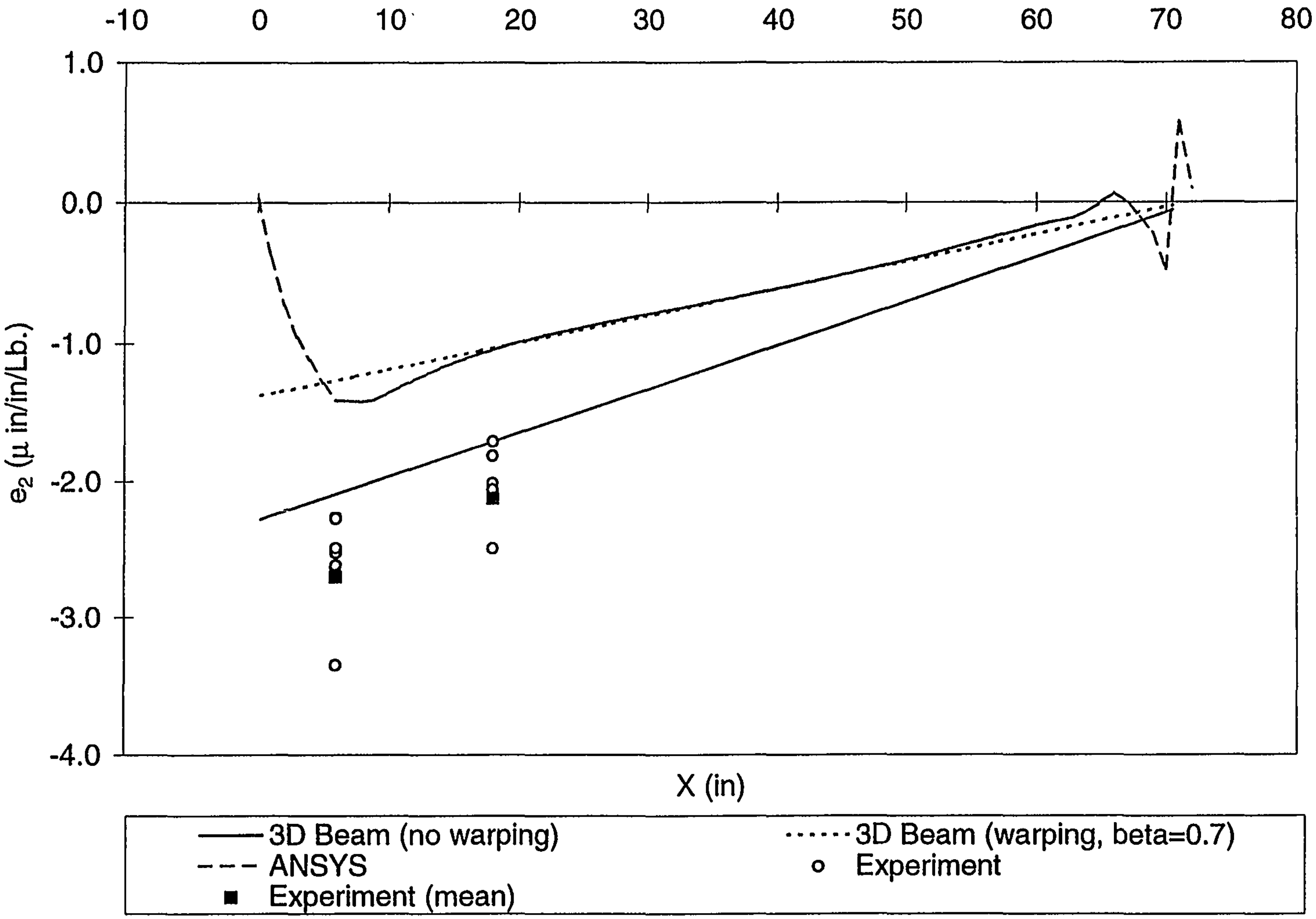

Figure 6.13 Transverse Strain (e_2) at the Top Skin (y=0") of the Hybrid D-spar Under Tip Unit Pound Force

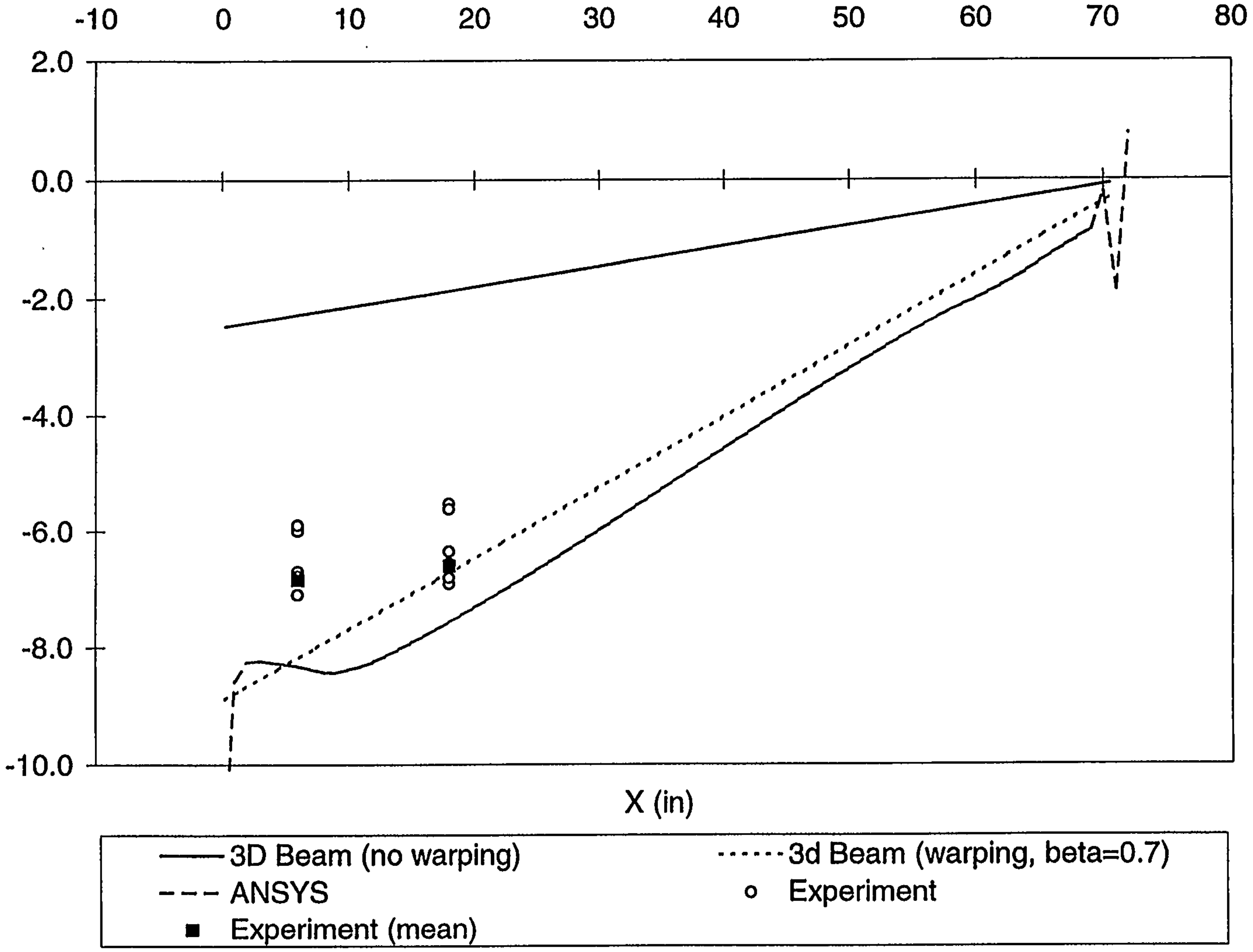

Figure 6.14 Shear Strain (e_6) at the Top Skin (y=0") of the Hybrid D-spar Under Tip Unit Pound Force

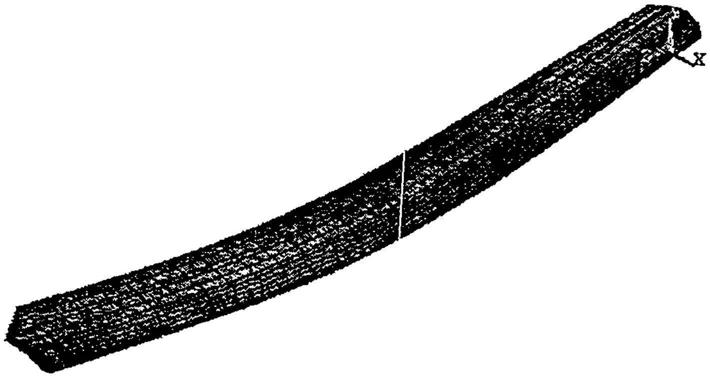

Figure 6.15(a) First Flatwise Bending Mode (ANSYS; frequency= 146.2Hz)

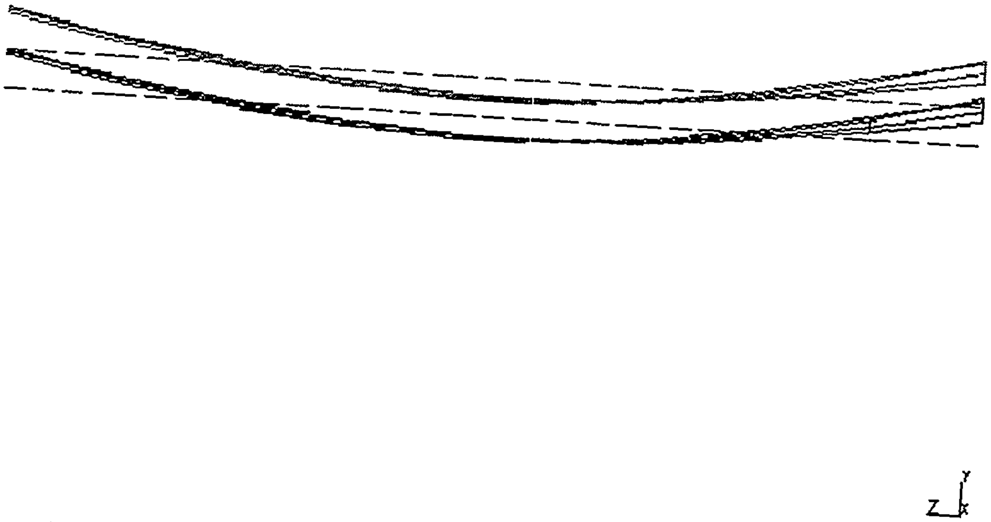

Figure 6.15(b) First Flatwise Bending Mode (Modal Test; frequency= 145.0 Hz)

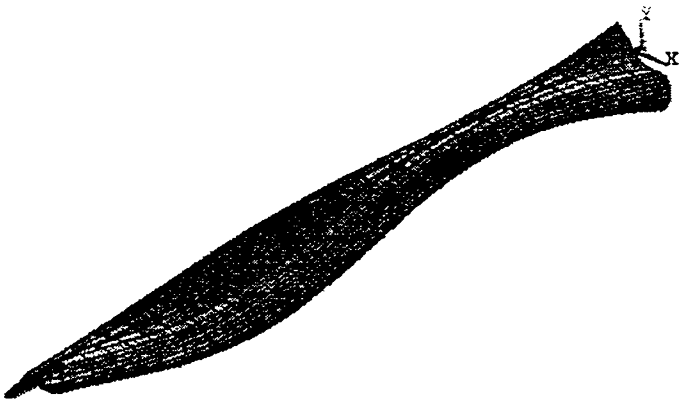

Figure 6.16(a) Second Flatwise Bending Mode (ANSYS; frequency= 330.3Hz)

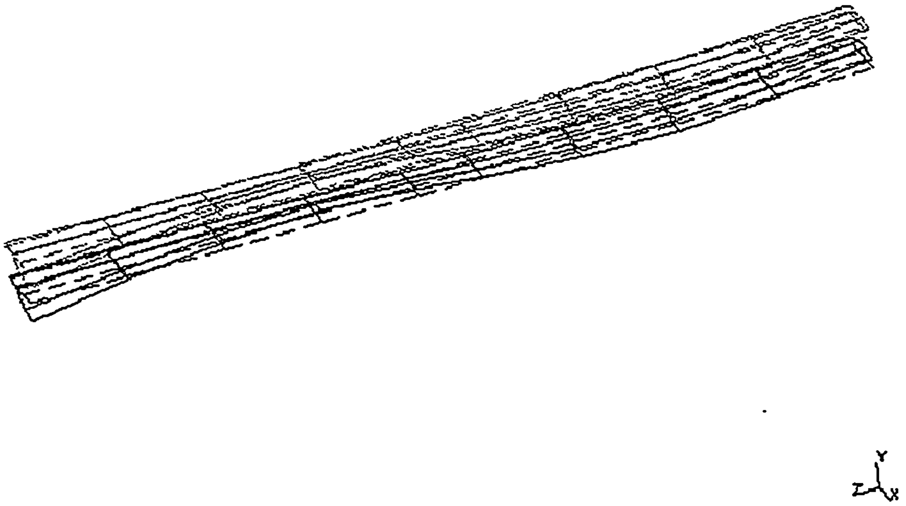

Figure 6.16(b) Second Flatwise Bending Mode (Modal Test; frequency= 338.8Hz)

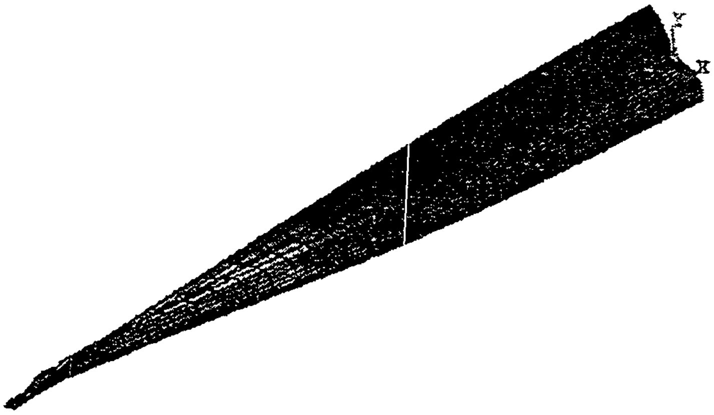

Figure 6.17(a) First Torsion Mode (ANSYS; frequency= 264.6Hz)

Figure 6.17(b) First Torsion Mode (Modal Test; frequency= 282.1Hz)

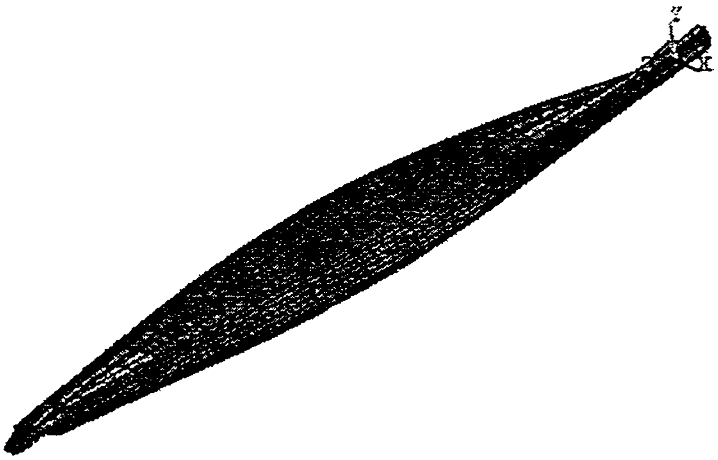

Figure 6.18(a) Second Torsion Mode (ANSYS; frequency= 289.1Hz)

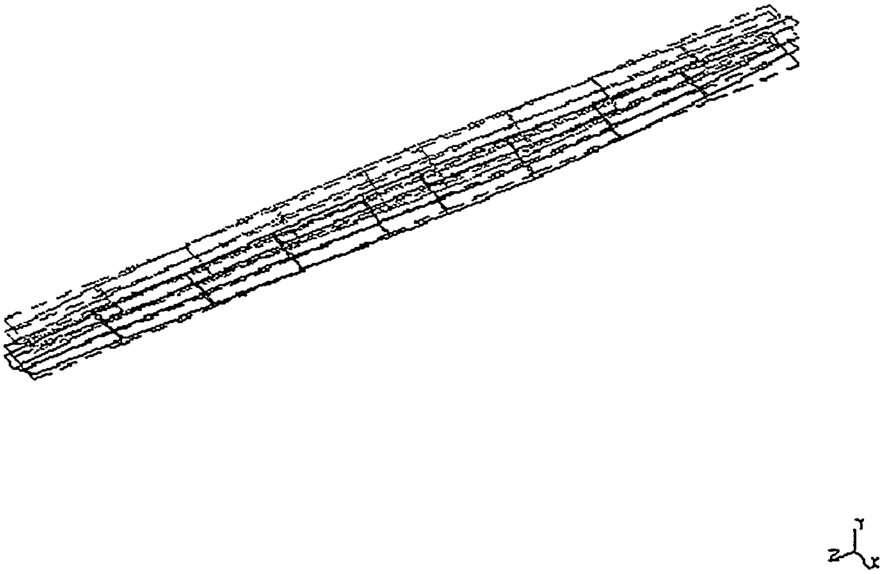

Figure 6.18(b) Second Torsion Mode (Modal Test; frequency= 309.6Hz)

Chapter 7

Conclusions

The three key parameters that have the greatest effect on the coupling coefficient are the ply orientation, the laminate material, and the proportional volume of anisotropy layers in a laminate. A higher α value is achieved by having the ply orientation between 15° and 30° and by using a high-performance ply material such as Graphite/Epoxy. Graphite/Epoxy D-spars have a maximum coupling around $\alpha=0.55$, while those with Glass/Epoxy have a maximum coupling around $\alpha=0.4$. The hybrid lay-up configuration has an α close to that of the Graphite/Epoxy D-spar. Other parameters, such as the geometry and the inclusion of internal rib, change the magnitude of α, but the effect is not significant.

The three critical parameters have been fully utilized in the D-spar design. To achieve the maximum tip rotation per unit pound force, the α value must be maximized and the square root of the product of "EI" and "GJ" must be minimized. With using just one off-axis unidirectional lay-up, the desired structural properties were achieved to within 15% for two of the three D-spar configurations.

Two D-spars, the all-carbon and the hybrid D-spars, were successfully fabricated. The staggered overlap joint that was invented during the fabrication eases the problems caused by a butt joint or a single overlap joint design. The step-change in thickness surrounding the joint is drastically reduced with this new design. The cantilevered static test demonstrated that the manufactured hybrid D-spar does produce the desired coupling. The test results generally indicate greater coupling than the numerical results (predicted by 3D-Beam) without torsion-related warping effect. When warping is included in the predictions, much better agreement with test data is obtained, indicating a significant beneficial effect on the bend-induced twist.

The predicted results of the ANSYS model (both static and modal analysis) are close to the experimental results after the adjustments were made to better match the as-built D-spar geometry and material properties. Extensive study of parameter sensitivity was not required because the baseline results are close to the modal test results. Minor adjustments on the modulus (E_x) and the thickness bring the average prediction error to less than 5% for the beam modes and torsion modes.

References

1. T. Weisshaar, "Aeroelastic Tailoring - Creative Uses of Unusual Materials," AIAA Paper No. 87-0976-CP, 1987.

2. E. C. Smith and I. Chopra, "Formulation and Evaluation of an Analytical Model for Composite Box-Beams," AIAA-90-0962-CP, 1990.

3. Ramesh Chandra, Alan D. Stemple, and Inderjit Chopra, "Thin-Walled Composite Beams Under Bending, Torsional, and Extensional Loads," *Journal of Aircraft*, Vol. 27, No. 7, July 1990.

4. N.M. Karaolis, P.J. Mussgrove and G. Jeronimidis, "Active and Passive Aerodynamic Power Control Using Asymmetric Fiber Reinforced Laminates for Wind Turbine Blades," Proc. *10th British Wind Energy Conf.*, D.J. Milbrow Ed., London, March 22-24, 1988.

5. N.M. Karaolis, G. Jeronimidis and P.J. Mussgrove, "Composite Wind Turbine Blades: Coupling Effects and Rotor Aerodynamic Performance," Proc., *EWEC'89*, European Wing Energy Conf., Glasgow, Scotland, 1989.

6. H.J.T. Koijman, "Bending-Torsion Coupling of a Wind Turbine Rotor Blade," ECN-I-96-060, December 1996.

7. D.W. Lobitz, P.S. Veers and P.G. Migliore, "Enhanced Performance of HAWTs Using Adaptive Blades," Proc. *Wind Energy '96, ASME Wing Energy Symposium*, Houston, Jan. 29 - Feb. 2, 1996.

8. D.W. Lobitz and D.J. Laino, "Load Mitigation with Twist-Coupled HAWT Blades," *Proceedings of the 1999 ASME Wing Energy Symposium*, Reno, January 11-14, 1999.

9. D.W. Lobitz and P.S. Veers, "Aeroelastic Behavior of Twist-Coupled HAWT Blades," AIAA-98-0029, Proc. *1998 ASME Wind Energy Symposium* held at 36th AIAA Aerospace Sciences Meeting and Exhibition, Reno, NV, Jan. 12-15, 1998.

10. S. Shinh, "Composite Blade Model and Software," XAF-4-14076-01, September 1997.

11. C.H. Ong., "Composite Tubular Structures," *Proceedings of the Fifth Japan International SAMPE Symposium*, October 38-31, 1997

12. S.W. Tsai and H. T. Hahn, *Introduction to Composite Materials*, Technomic Publishing Company, Inc., 1980.

13. T.G. Carne and B.D. Boughton, "Modal Testing of the Graphite and Hybrid D-Spars for Model Validation," Internal Memorandum, Sandia National Laboratories, March 25, 1999.

DISTRIBUTION

R. E. Akins
Washington & Lee University
P.O. Box 735
Lexington, VA 24450

T. Almeida
TPI Inc.
225 Alexander Road
Portsmouth, RI 02871

H. Ashley
Dept. of Aeronautics and
Astronautics Mechanical Engr.
Stanford University
Stanford, CA 94305

M. Balas
University of Colorado
Dept. of Aerospace Eng. Sciences
Campus Box 429
Boulder, CO 80309-0429

Hui Bau
NSE Composites Stress Services
6417 Woodland Place North
Seattle, WA 98103

A. Beattie
Physical Acoustics
PO Box 462
Corrales, NM 87048

B. Bell
Zond Systems Inc.
P.O. Box 1970
Tehachapi, CA 93581

K. Bergey
University of Oklahoma
Aero Engineering Department
Norman, OK 73069

C. P. Butterfield
NREL
1617 Cole Boulevard
Golden, CO 80401

G. Bywaters
Northern Power Systems
Box 999
Waitsfield,VT 05673

J. Cadogan
U.S. Department of Energy
Office of Photovoltaic & Wind
Technology
Energy Efficiency & Renewable Energy
EE-11
1000 Independence Avenue SW
Washington, DC 20585

D. Cairns
Montana State University
Mechanical & Industrial
Engineering Department
Bozeman, MT 59717

S. Calvert
U.S. Department of Energy
Office of Photovoltaic & Wind
Technology
Energy Efficiency & Renewable Energy
EE-11
1000 Independence Avenue SW
Washington, DC 20585

J. Chapman
OEM Development Corp.
840 Summer St.
Boston, MA 02127-1533

R. N. Clark
USDA
Agricultural Research Service
P.O. Drawer 10
Bushland, TX 79012

J. Cohen
Princeton Economic Research, Inc.
1700 Rockville Pike
Suite 550
Rockville, MD 20852

C. Coleman
Northern Power Systems
Box 999
Waitsfield, VT 05673

K. Cousineau
Zond Systems Inc.
PO Box 1970
Tehachapi, CA 93581

M. Cramer
Foam Matrix, Inc.
PO Box 6394
Malibu, CA 90264

K. J. Deering
The Wind Turbine Company
515 116th Avenue NE
No. 263
Bellevue, WA 98004

E. A. DeMeo
Electric Power Research Institute
3412 Hillview Avenue
Palo Alto, CA 94304

A. J. Eggers, Jr.
RANN, Inc.
744 San Antonio Road, Ste. 26
Palo Alto, CA 94303

D. M. Eggleston
DME Engineering
1605 W. Tennessee
Midland, TX 79701

W. Erdman
Trace Technologies
P.O. Box 5049
Livermore, CA 94551-5049

L. J. Fingersh
NREL
1617 Cole Boulevard
Golden, CO 80401

T. Forsythe
NREL
1617 Cole Boulevard
Golden, CO 80401

P. R. Goldman
Acting Deputy Director
Office of Photovoltaic and
Wind Technology
Energy Efficiency & Renewable
Energy, EE-11
U.S. Department of Energy
1000 Independence Avenue
Washington, DC 20585

G. Gregorek
Aeronautical & Astronautical Dept.
Ohio State University
2300 West Case Road
Columbus, OH 43220

C. Hansen
University of Utah
Department of Mechanical Engineering
Salt Lake City, UT 84112

C. Hedley
Headwaters Composites, Inc.
PO Box 1073
105 E. Adams Street
Three Forks, MT 59752

L. Helling
Librarian
National Atomic Museum
Albuquerque, NM 87185

C. Hiel
W. Brandt Goldsworthy & Assoc.
23930-40 Madison Street
Torrance, CA 90505

S. Hock
Wind Energy Program
NREL
1617 Cole Boulevard
Golden, CO 80401

W. E. Holley
3731 Oak Brook Court
Pleasanton, CA 94588

K. Jackson
Dynamic Design
123 C Street
Davis, CA 95616

G. James
ISSO Fellow
University of Houston
4800 Calhoun
Houston, TX 77204-4792

O. Krauss
Division of Engineering Research
Michigan State University
East Lansing, MI 48825

R. Lynette, President
Springtyme Co.
212 Jamestown Beach Lane
Sequim, WA 98382

D. Malcolm
Kamzin Technology Inc.
425 Pontius Avenue North
Suite 150
Seattle, WA 98109

J. F. Mandell
Montana State University
302 Cableigh Hall
Bozeman, MT 59717

T. McCoy
Kamzin Technology Inc.
425 Pontius Avenue North
Suite 150
Seattle, WA 98109

R. N. Meroney
Dept. of Civil Engineering
Colorado State University
Fort Collins, CO 80521

P. Migliore
NREL
1617 Cole Boulevard
Golden, CO 80401

A. Mikhail
Zond Systems, Inc.
P.O. Box 1970
Tehachapi, CA 93581

E. Muljadie
NREL
1617 Cole Boulevard
Golden, CO 80401

W. Musial
NREL
1617 Cole Boulevard
Golden, CO 80401

NWTC Library (5)
NREL
1617 Cole Boulevard
Golden, CO 80401

V. Nelson
Department of Physics
West Texas State University
P.O. Box 248
Canyon, TX 79016

G. Nix
NREL
1617 Cole Boulevard
Golden, CO 80401

J. W. Oler
Mechanical Engineering Dept.
Texas Tech University
P.O. Box 4289
Lubbock, TX 79409

Cheng-Huat Ong
Stanford University
Dept. of Aeronautics & Astronautics
Stanford, CA 94305-4035

R. Poore
Kamzin Technology Inc.
425 Pontius Avenue North
Suite 150
Seattle, WA 98109

R. G. Rajagopalan
Aerospace Engineering Department
Iowa State University
404 Town Engineering Bldg.
Ames, IA 50011

J. Richmond
3368 Mountain Trail Avenue
Newbury Park, CA 91320

M. Robinson
NREL
1617 Cole Boulevard
Golden, CO 80401

S. Rock
Stanford University
MC 4035
Stanford, CA 94305-4035

D. Sanchez
U.S. Dept. of Energy
Albuquerque Operations Office
P.O. Box 5400
Albuquerque, NM 87185

W. Sass
Second Wind
366 Summer Street
Summerville, MA 02144

L. Schienbein
CWT Power
4006 S. Morain Loop
Kennewick, WA 99337

B. Smith
NREL
1617 Cole Boulevard
Golden, CO 80401

D.Y.D. Song
North Carolina A&T State University
Dept. of Electrical Engineering
Greensboro, NC 27411

K. Starcher
AEI
West Texas State University
P.O. Box 248
Canyon, TX 79016

F. S. Stoddard
Dynamic Design-Atlantic Office
P.O. Box 1373
Amherst, MA 01004

A. Swift
University of Texas at El Paso
320 Kent Ave.
El Paso, TX 79922

J. Tangler
NREL
1617 Cole Boulevard
Golden, CO 80401

R. W. Thresher
NREL
1617 Cole Boulevard
Golden, CO 80401

S. Tsai (10)
Stanford University
Dept. of Aeronautics & Astronautics
Stanford, CA 94305-4035

W. A. Vachon
W. A. Vachon & Associates
P.O. Box 149
Manchester, MA 01944

B. Vick
USDA, Agricultural Research Service
P.O. Drawer 10
Bushland, TX 79012

C. Weigand
Electronic Power Conditioning Inc.
1895 NW 9th Street
Corvallis, OR 97330

L. Wendell
2728 Enterprise Dr.
Richland, WA 99352

K. Wetzel
Zond Systems Inc.
PO Box 1970
Tehachapi, CA 93581

R. E. Wilson
Mechanical Engineering Dept.
Oregon State University
Corvallis, OR 97331

S. R. Winterstein
Civil Engineering Department
Stanford University
Stanford, CA 94305

R. Zadoks
UTEP
Mechanical & Industrial Engineering
500 W. University Ave.
El Paso, TX 79968-0521

M. Zuteck
MDZ Consulting
931 Grove Street
Kemah, TX 77565

M.S. 0437	K. E. Metzinger, 9117	
M.S. 0439	D. W. Lobitz, 9234	
M.S. 0439	D. R. Martinez, 9234	
M.S. 0555	B. Hansche, 9133	
M.S. 0557	T. J. Baca, 9119	
M.S. 0557	B. Boughton, 9119	
M.S. 0557	T. G. Carne, 9119	
M.S. 0557	M. Sagartz, 9119	
M.S. 0708	H. M. Dodd, 6214	(25)
M.S. 0708	T. D. Ashwill, 6214	
M.S. 0708	D. E. Berg, 6214	
M.S. 0708	P. L. Jones 6214	
M.S. 0708	D. L. Laird, 6214	
M.S. 0708	M. A. Rumsey, 6214	
M.S. 0708	H. J. Sutherland, 6214	
M.S. 0708	P. S. Veers, 6214	
M.S. 0708	J. R. Zayas, 6214	
M.S. 0836	J. H. Strickland, 9116	
M.S. 0836	G. F. Homicz, 9116	
M.S. 0836	W. Wolfe, 9116	
M.S. 0958	M. Donnelly, 1472	
M.S. 0958	T. R. Guess, 1472	
M.S. 0619	Review & Approval Desk, 00111 For DOE/OSTI	
M.S. 0899	Technical Library, 4916	(2)
M.S. 9018	Central Technical Files, 8940-2	